N°d'ordre NNT : 2023ISAL0085

DOCTORAL THESIS of the
Institut National des Sciences Appliquées, INSA – Lyon

Member of UNIVERSITE DE LYON

Doctoral School N° 160
Mécanique, Énergétique, Génie civil, Acoustique

Specialty/ discipline of doctorate:
Biomechanics

Publicly defended on 10/11/2023, by:
Samaneh Choupani

Intravascular manometry by clinical color Doppler

In front of the jury composed of:

Deplano, Valérie	Research Director CNRS, Marseille	Reviewer
Løvstakken, Lasse	Professor NTNU, Norway	Reviewer
Bernard, Olivier	Professor INSA, Lyon	Examiner
Rouet, Laurence	PhD, senior researcher Philips Medisys, Paris	Examiner
Béra, Jean-Christophe	Professor UCBL, Lyon	Co-supervisor
Gilles, Bruno	Associate Professor UCBL, Lyon	Co-supervisor
Varray, François	Associate Professor UCBL, Lyon	Co-director
Garcia, Damien	Research Director INSERM, Lyon	Thesis director

Département de la Formation par la Recherche
et des Études Doctorales (**FEDORA**)

Bâtiment INSA direction, 1er étage
37, av. J. Capelle
69621 Villeurbanne Cédex
fedora@insa-lyon.fr

Référence : TH1006_Samaneh CHOUPANI

L'INSA Lyon a mis en place une procédure de contrôle systématique via un outil de détection de similitudes (logiciel Compilatio). Après le dépôt du manuscrit de thèse, celui-ci est analysé par l'outil. Pour tout taux de similarité supérieur à 10%, le manuscrit est vérifié par l'équipe de FEDORA. Il s'agit notamment d'exclure les auto-citations, à condition qu'elles soient correctement référencées avec citation expresse dans le manuscrit.

Par ce document, il est attesté que ce manuscrit, dans la forme communiquée par la personne doctorante à l'INSA Lyon, satisfait aux exigences de l'Etablissement concernant le taux maximal de similitude admissible.

INSA LYON
Campus LyonTech La Doua
20, avenue Albert Einstein - 69621 Villeurbanne cedex - France
Tél. +33 (0)4 72 43 83 83 - Fax +33 (0)4 72 43 85 00
www.insa-lyon.fr

Département FEDORA – INSA Lyon - Ecoles Doctorales

SIGLE	ECOLE DOCTORALE	NOM ET COORDONNEES DU RESPONSABLE
CHIMIE	**CHIMIE DE LYON** **https://www.edchimie-lyon.fr** Sec. : Renée EL MELHEM Bât. Blaise PASCAL, 3e étage secretariat@edchimie-lyon.fr	**M. Stéphane DANIELE** C2P2-CPE LYON-UMR 5265 Bâtiment F308, BP 2077 43 Boulevard du 11 novembre 1918 69616 Villeurbanne **directeur@edchimie-lyon.fr**
E.E.A.	**ÉLECTRONIQUE, ÉLECTROTECHNIQUE, AUTOMATIQUE** **https://edeea.universite-lyon.fr** Sec. : Stéphanie CAUVIN Bâtiment Direction INSA Lyon Tél : 04.72.43.71.70 secretariat.edeea@insa-lyon.fr	**M. Philippe DELACHARTRE** INSA LYON Laboratoire CREATIS Bâtiment Blaise Pascal, 7 avenue Jean Capelle 69621 Villeurbanne CEDEX Tél : 04.72.43.88.63 **philippe.delachartre@insa-lyon.fr**
E2M2	**ÉVOLUTION, ÉCOSYSTÈME, MICROBIOLOGIE, MODÉLISATION** **http://e2m2.universite-lyon.fr** Sec. : Bénédicte LANZA Bât. Atrium, UCB Lyon 1 Tél : 04.72.44.83.62 secretariat.e2m2@univ-lyon1.fr	**Mme Sandrine CHARLES** Université Claude Bernard Lyon 1 UFR Biosciences Bâtiment Mendel 43, boulevard du 11 Novembre 1918 69622 Villeurbanne CEDEX **sandrine.charles@univ-lyon1.fr**
EDISS	**INTERDISCIPLINAIRE SCIENCES-SANTÉ** **http://ediss.universite-lyon.fr** Sec. : Bénédicte LANZA Bât. Atrium, UCB Lyon 1 Tél : 04.72.44.83.62 secretariat.ediss@univ-lyon1.fr	**Mme Sylvie RICARD-BLUM** Institut de Chimie et Biochimie Moléculaires et Supramoléculaires (ICBMS) - UMR 5246 CNRS - Université Lyon 1 Bâtiment Raulin - 2ème étage Nord 43 Boulevard du 11 novembre 1918 69622 Villeurbanne Cedex Tél : +33(0)4 72 44 82 32 **sylvie.ricard-blum@univ-lyon1.fr**
INFOMATHS	**INFORMATIQUE ET MATHÉMATIQUES** **http://edinfomaths.universite-lyon.fr** Sec. : Renée EL MELHEM Bât. Blaise PASCAL, 3e étage Tél : 04.72.43.80.46 infomaths@univ-lyon1.fr	**M. Hamamache KHEDDOUCI** Université Claude Bernard Lyon 1 Bât. Nautibus 43, Boulevard du 11 novembre 1918 69 622 Villeurbanne Cedex France Tél : 04.72.44.83.69 **hamamache.kheddouci@univ-lyon1.fr**
Matériaux	**MATÉRIAUX DE LYON** **http://ed34.universite-lyon.fr** Sec. : Yann DE ORDENANA Tél : 04.72.18.62.44 yann.de-ordenana@ec-lyon.fr	**M. Stéphane BENAYOUN** Ecole Centrale de Lyon Laboratoire LTDS 36 avenue Guy de Collongue 69134 Ecully CEDEX Tél : 04.72.18.64.37 **stephane.benayoun@ec-lyon.fr**
MEGA	**MÉCANIQUE, ÉNERGÉTIQUE, GÉNIE CIVIL, ACOUSTIQUE** **http://edmega.universite-lyon.fr** Sec. : Stéphanie CAUVIN Tél : 04.72.43.71.70 Bâtiment Direction INSA Lyon mega@insa-lyon.fr	**M. Jocelyn BONJOUR** INSA Lyon Laboratoire CETHIL Bâtiment Sadi-Carnot 9, rue de la Physique 69621 Villeurbanne CEDEX **jocelyn.bonjour@insa-lyon.fr**
ScSo	**ScSo*** **https://edsciencessociales.universite-lyon.fr** Sec. : Mélina FAVETON INSA : J.Y. TOUSSAINT Tél : 04.78.69.77.79 melina.faveton@univ-lyon2.fr	**M. Bruno MILLY** Université Lumière Lyon 2 86 Rue Pasteur 69365 Lyon CEDEX 07 **bruno.milly@univ-lyon2.fr**

*ScSo : Histoire, Géographie, Aménagement, Urbanisme, Archéologie, Science politique, Sociologie, Anthropologie

Acknowledgments

First, I would like to extend a heartfelt thank you to my PhD directors, Damien Garcia and François Varray. Your constant support at every step of this project has been incredible. You have both been there for me throughout this journey, and I cannot thank you enough. Special thanks also to my co-supervisors, Jean-Christophe Béra and Bruno Gilles, your guidance and assistance have been instructive and greatly appreciated.

I want to express my immense gratitude to all my friends and colleagues at Creatis and Labtau, especially the fellows from office number 21; we have truly had some fantastic times together. Among them is the love of my life, Mehdi, who have been there for me through every high and low, both at work and in our personal life. It is kind of funny and wonderful how we ended up working together so closely, that was one in a million! Louise, you were always there to encourage us to step out and connect with others; Sophie, for your yummy “chouquettes”; Alexandre, for your Persian catchphrases and Cyril, for your passion for JDD, each of you has made arriving at work each day a pleasure. And of course, my lovely family, though you might be miles away, your love and support have always felt close by. So, a massive thanks to each and every one of you. This journey would not have been possible without your help, patience, and encouragement.

Finally, I would like to express my sincere gratitude to the LabEx CeLyA (ANR-11-LABX-0060) at the Université de Lyon, within the program "Investissements d’Avenir" (ANR-11-IDEX-0007) operated by the French National Research Agency (ANR), for funding my doctoral research and supporting my various conference travels. Additionally, I appreciate the financial support from EUR MANUTECH SLEIGHT (ANR-17-EURE-0026) for the study, and the PILOT (INSA Lyon, France) for providing the necessary facilities.

Contents

Introduction

Arterial stenosis is a pathological condition of the vascular system, characterized by the accumulation of atherosclerotic plaques, composed of lipids, inflammatory cells, and fibrous tissue, within the arterial wall. This accumulation results in progressive arterial narrowing, causing partial or complete vessel occlusion.

In severe cases, arterial stenosis can lead to significant hemodynamic changes and impair the delivery of oxygen and nutrients to the affected tissue, increasing the risk of cardiovascular events and tissue damage. The carotid artery, a critical vessel responsible for supplying blood to the head and brain, is particularly susceptible to atherosclerotic plaque formation due to multiple risk factors including modern lifestyles.

An accurate assessment of stenosis severity in this disease is essential for determining the optimal treatment approach. Ultrasound imaging is the standard procedure for quantifying the degree of carotid artery stenosis. This method involves measuring the geometric dimensions of the carotid artery and the plaque from the echographic image and applying established diagnostic criteria such as the North American symptomatic carotid endarterectomy trial (NASECT) or the European carotid surgery trial (ECST) to calculate the percentage of luminal narrowing. External factors can affect this method, so even small changes in measurement can cause errors in the calculations and may result in the misclassification of the degree of stenosis. Moreover, geometric parameters are limited in providing clinicians with comprehensive information about the hemodynamic characteristics of intra-arterial blood flow.

Given the limitations of using geometric parameters for assessing arterial stenosis, alternative methods incorporating hemodynamic parameters, such as measuring pressure drop along the arterial occlusion, have emerged as more reliable and comprehensive approaches for evaluating blood flow characteristics and identifying potentially high-risk stenoses.

The clinical method of measuring trans-stenotic pressure drop involves an invasive technique known as catheterization, which requires inserting a wire equipped with a pressure sensor into the affected artery. However, this method carries risks of side effects and potential complications, such as bleeding, infection, and arterial damage, limiting its clinical utility. Thus, medical professionals tend to utilize non-invasive methodologies to gather information about the hemodynamic functionality of blood flow, such as echocardiography or phase-contrast magnetic resonance imaging (PC-MRI). Due to its expensive and time-consuming nature, PC-MRI imaging is primarily performed in research applications. Accordingly, recent studies have redirected their attention towards using echocardiography as a real-time and accessible imaging modality.

The present study addresses this concern by developing a non-invasive method that employs conventional clinical color Doppler ultrasound imaging to estimate the trans-stenotic pressure loss in mild to moderate carotid artery stenosis, to evaluate its severity for earlier diagnosis.

To accomplish the objective of this study, we estimated the post-stenotic pressure drop in multiple common carotid artery stenosis phantoms with different stenosis geometry and occlusion percentages, utilizing *in vitro* experiments conducted through color Doppler imaging. These phantoms were fabricated explicitly for this purpose. During the validation phase of this non-invasive technique, particle image velocimetry (PIV) was performed on the same stenotic phantoms.

This scientific research highlights the significant contribution of our current study in advancing knowledge within this area. Therefore, this manuscript is organized into separate chapters, which cover various aspects of the study, including:

The **first chapter** of this thesis introduces the blood circulatory system in the human body, with a particular focus on carotid artery stenosis. The medical context of this study is also presented for a comprehensive understanding of the topic.

In the **second chapter**, we examine the current state-of-the-art methods for blood flow velocity imaging across various image modalities. By assessing each approach, we will identify their respective strengths and limitations. Furthermore, we will explain the distinct advantages offered by our proposed approach in comparison to these existing methods.

In the **third chapter**, we will discuss different state-of-the-art approaches for calculating pressure in conjunction with obtained velocities. We will explore the theoretical foundations, computational techniques, and practical applications of each method. By comparing the advantages and limitations of our proposed technique with other relevant studies, we emphasize our crucial role in expanding the scope of research in this domain.

In the **fourth chapter**, we will explain our developed approach to achieve the objectives of this study. Firstly, we will introduce a novel vascular vector flow mapping (vVFM) technique for converting the color Doppler scalar velocity field into a two-dimensional vector velocity field by solving an inverse problem. Additionally, we will present the second inverse problem to estimate pressure losses using the fluid dynamic equations for the calculated velocity vector field.

In the **fifth chapter** of our study, we describe in detail the methods and materials used to perform *in vitro* color Doppler echography and PIV experiments. It includes the design and fabrication of phantoms specific for each modality, along with the latest state-of-the-art techniques.

In the **sixth chapter**, which focuses on the results, we will present the validation outcomes of our developed algorithm, consisting of two optimization problems. The validation process includes both *in silico* simulations utilizing computational fluid dynamics (CFD) and *in vitro* experiments performed using color Doppler echography PIV techniques on phantoms. By employing these diverse methodologies, we aim to provide comprehensive evidence of the algorithm's performance and efficacy.

Finally, in the **seventh chapter**, we will discuss the estimated trans-stenotic pressure drop results derived from the acquired color Doppler ultrasound data using our technique. Additionally, the project will conclude with a summary of the key points covered in each chapter. Furthermore, a forward-looking perspective on future research will be presented, addressing the limitations identified in this scientific investigation.

1

Medical Context

This chapter presents an overview of arterial stenosis, emphasizing the significance of early diagnosis and appropriate treatment. It explores the potential complications associated with arterial stenosis and discusses the common invasive method used for assessing its severity. Furthermore, the chapter highlights the need for non-invasive methods in this assessment. It introduces the main objective of the study, which is to develop a non-invasive technique using clinical color Doppler ultrasound imaging to estimate the pressure drop across arterial stenosis and grade its occlusion.

Contents

1.1 Arterial stenosis

The blood circulatory system is a complex and vital network of organs, vessels, and fluids that plays a critical role in the proper functioning of the human body. The system is responsible for transporting oxygen, nutrients, and waste products to and from the body's tissues and organs [1]. At the center of the blood circulatory system is the heart, which pumps blood throughout the body via a series of arteries, veins, and capillaries. The former, which carries oxygenated blood away from the heart, is divided into two main types: systemic and pulmonary. Systemic types supply oxygenated blood to the body's tissues and organs, while deoxygenated blood is carried to the lungs for oxygenation from pulmonary ones [2].

Arterial stenosis refers to the narrowing or constriction of any of these arteries, which restricts or obstructs the normal blood flow through them. It is caused by the accumulation of plaque, a fatty substance, on their inner walls. This can occur in various arteries throughout the body, including the coronary, the carotid or the peripheral arteries such as femoral, respectively supplying blood to the heart, the brain and the lower limbs. The narrowing of the artery can lead to reduced blood flow, compromised oxygen supply, and potential complications such as ischemia, tissue damage, or even complete blockage in severe cases. Prompt diagnosis and appropriate treatment are crucial in managing arterial stenosis to prevent further complications and maintain optimal blood flow [3].

1.1.1 Carotid artery in the blood circulatory system

One of the vital peripheral arteries in the body is the carotid artery, located on both sides of the neck and supplies oxygenated blood to the brain. It originates at the aortic arch in the thoracic cavity and ascends to the neck. At the level of the larynx, it bifurcates into the external and internal carotid arteries (Figure 1.1). The external carotid artery supplies blood to the face, scalp, and neck muscles, whereas the internal carotid artery delivers blood to the brain. The latter is crucial for brain function since it nourishes the cerebrum responsible for consciousness, thought, and movement. Any blockages or disruptions to the blood flow through the carotid arteries can lead to serious health consequences, including stroke or other neurological impairments, highlighting its importance in maintaining human health [4].

1.1.2 Carotid arterial stenosis

Carotid arterial stenosis is characterized by the narrowing of one or both of the carotid arteries. This is typically caused by the build-up of atherosclerotic plaque within the vessel wall, leading to reduced blood flow to the brain and an increased risk of stroke (Figure 1.2). The most common symptoms of this disease are transient ischemic attacks (TIAs) or strokes, which can cause weakness or numbness on one side of the body, slurred speech, and difficulty with vision or walking. However, many people with carotid stenosis may be asymptomatic, and their condition might be detected incidentally in imaging studies [5]. There are several treatment methods for carotid stenosis, which depend on the severity of the condition and the patient's health needs [6]. The treatment options include:

- *Lifestyle changes*: The first step in treating carotid arterial stenosis is to make lifestyle changes that can help to reduce the risk of further plaque build-up. It may include quitting smoking, maintaining a healthy weight, exercising regularly, and eating a healthy diet low in saturated fats and cholesterol.

- *Medications*: Several medications can be used to treat this disease. Antiplatelet agents can prevent blood clots from forming in the narrowed artery. Anticoagulants can also be used to avoid blood clots. Cholesterol-lowering medications can lower cholesterol levels and reduce the risk of further plaque build-up.

- *Carotid artery stenting*: This invasive procedure involves inserting a small metal mesh tube, called a stent, into the narrowed artery. The stent expands and holds the vessel open, allowing blood to flow freely.

- *Carotid endarterectomy*: This surgical procedure removes plaque build-up from the carotid artery. The surgeon incise the neck and exposes the affected blood vessel. The plaque is then removed and repaired with sutures.

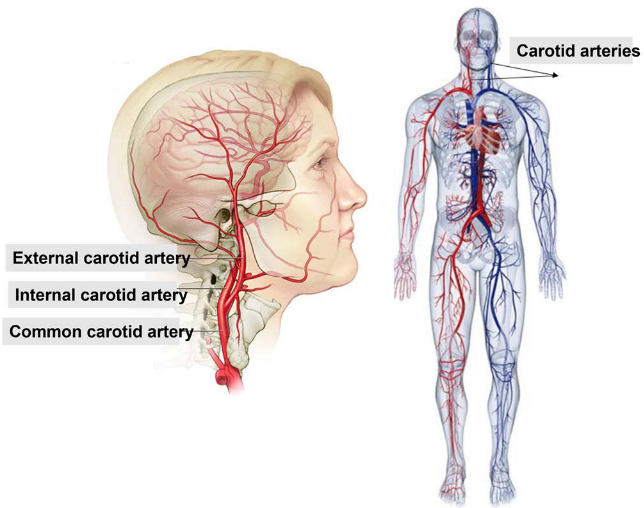

Figure 1.1: (left) Carotid arteries. (right) Blood circulatory system in the human body.[1]

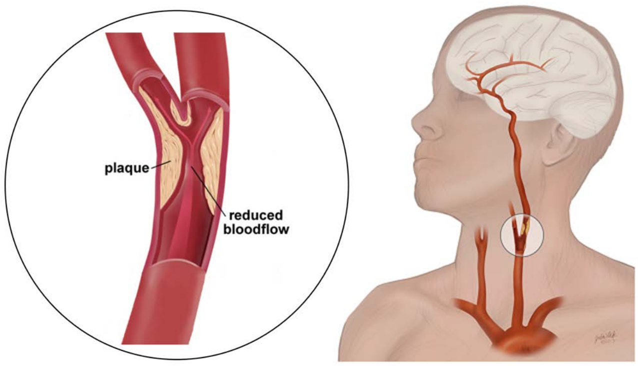

Figure 1.2: Carotid arterial stenosis, which shows accumulated plaque and impaired blood flow.[2]

Figure 1.3. depicts the two invasive surgeries for treating carotid artery stenosis mentioned earlier.

[1] https://www.mayoclinic.org

[2] https://www.hopkinsmedicine.org

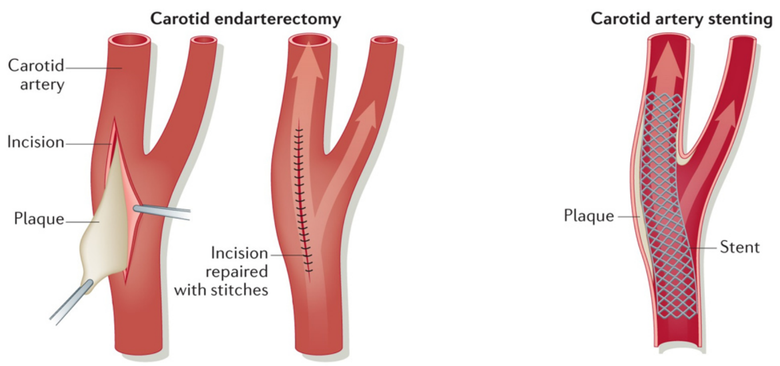

Figure 1.3: Two invasive surgery methods for Carotid arterial stenosis treatment [7].

1.2 Assessment of arterial stenosis severity

For optimal treatment selection among various methods, an accurate diagnosis approach is required to evaluate the severity of stenosis. This diagnosis typically involves a combination of physical examination, medical history review, and imaging to visualize the carotid arteries and determine their degree of occlusion [8]. Phase contrast magnetic resonance imaging (PC-MRI) is a highly effective method that can provide high-resolution images of the carotid arteries to assess the degree of stenosis and evaluate the composition of the plaque causing the stenosis. However, ultrasound imaging is generally preferred over PC-MRI due to its non-invasive nature, wide availability, and cost-effectiveness. Ultrasound is well suited for imaging the carotid arteries due to their superficial location, which allows to measure the degree of stenosis and hemodynamic significance of the stenosis in real-time. Additionally, ultrasound provides information on the plaque composition causing the stenosis, which can help predict the risk of future stroke. The standard grading commonly used methods for estimating the severity of arterial stenosis are [9]:

- North American Symptomatic Carotid Endarterectomy Trial (NASECT)
- European Carotid Surgery Trial (ECST)

Figure 1.4 demonstrates the calculation of the blockage percentage for each method. Although the NASCET and ECST methods are commonly employed to evaluate the extent of carotid stenosis, their usage may present particular challenges. As such, they should be used in conjunction with other pertinent clinical and imaging data to ensure informed decision-making in treatment:

- They rely on visual inspection of the stenosis. However, different observers may interpret the images differently, leading to high variability in the estimation.
- Lack of standardized imaging protocols and variations across modalities complicate comparisons of results across studies or different imaging centers.
- Their accuracy in estimating stenosis severity may be compromised due to reliance on a single carotid artery diameter measurement and influences from plaque presence or artery shape.

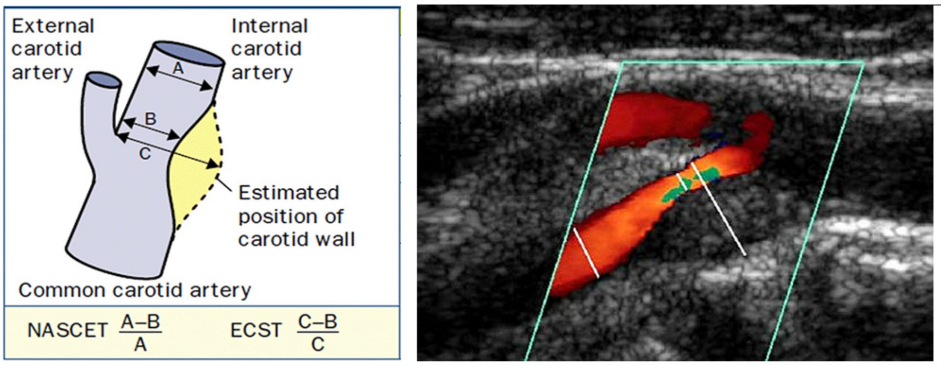

Figure 1.4: NASCET and ECST methods for assessing carotid stenosis severity, an example of using them on an ultrasound image [9].

- They guide carotid endarterectomy decisions, but over-treatment risks arise if stenosis estimates are too high or patient-specific factors like age or health are overlooked.

Moreover, while methods based solely on geometric parameters provide valuable information about the extent of narrowing and the potential risk of plaque rupture and stroke, they lack the ability to capture detailed hemodynamic information regarding arterial blood flow in stenotic lesions. The **hemodynamic function** of a stenotic lesion is influenced by various factors, including the severity and location of the stenosis, blood viscosity and flow rate, arterial wall compliance and elasticity, as well as the presence of collateral vessels or compensatory mechanisms. These factors interact in complex ways, affecting blood flow patterns and pressure gradients across the stenotic lesion [10–12]. In this regard, measuring the **intravascular blood pressure** differences between two related points in the cardiovascular region plays a crucial role as a diagnostic marker for assessing the pathological state of the cardiovascular system. Any abnormal changes in this parameter could indicate the presence of underlying cardiovascular disease [13, 14]. Therefore, measuring pressure variations is a well-established fluid dynamics approach that provides valuable insights into the hemodynamic functionality of vascular flow [15–17]. By measuring the total pressure loss between the inlet and outlet of the stenosis, a reliable method is employed to gather comprehensive information about the hemodynamic characteristics of stenotic blood flow (Figure 1.5).

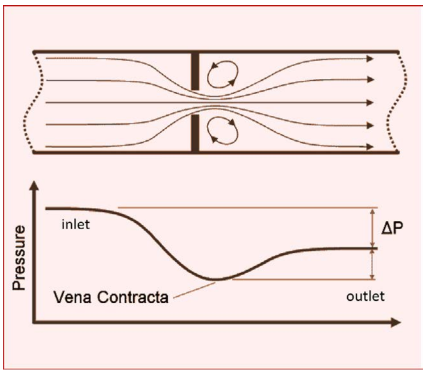

Figure 1.5: Total pressure loss between the inlet and outlet of a stenosis as a hemodynamic criterion for grading its severity.[3]

[3] https://www.biomecardio.com

1.3 Pressure loss across the arterial stenosis

When blood flows through arterial stenosis, it encounters resistance due to the narrowed passage, causing it to lose some of its energy irreversibly. This loss occurs in this situation primarily due to two reasons: an abrupt change in flow geometry and wall friction (Figure 1.6):

- *The abrupt change in flow geometry*: It represents a critical factor contributing to energy dissipation in the presence of a vascular stenosis. The narrowing of the vessel obstructs the smooth flow of blood, leading to a sudden alteration in flow geometry and subsequent turbulence in the blood flow. This turbulence induces the mixing of blood in distinct layers, while the presence of fluid viscosity generates internal friction, resulting in the dissipation of energy as heat [18]. It is important to note that the impact of this pressure loss factor is significantly higher and more dominant compared to wall friction.

- *Wall friction*: In the context of intravascular flow within the circulatory system, energy dissipation due to wall friction is an inherent phenomenon. It affects dynamics of blood flow to the progressive reduction of pressure along the flow pathway, resulting in a decrease in blood pressure from the arterial side to the venous side. This pressure drop is essential for maintaining blood circulation and facilitating proper perfusion of organs and tissues. It refers to the loss of energy that arises as blood travels along the inner walls of blood vessels. The movement of blood within these vessels encounters resistance from the vessel walls, leading to the generation of frictional forces. They act to convert the kinetic energy of the flowing blood into heat, resulting in irreversible energy loss that dissipates into the surrounding tissues. When an arterial stenosis is present, characterized by a narrowing of the artery's diameter, the blood is confined to flow through a reduced space. This condition increases wall friction due to its inverse relationship with the lumen diameter. In other words, as the lumen diameter decreases, the value of the wall friction rises [19].

This energy loss can be significant in severe cases of arterial stenosis and contribute to ischemia or reduced blood flow to tissues and organs. It is also responsible for forming atherosclerotic plaques in the arterial wall. As blood flows through a narrowed artery, it can damage the endothelial cells that line the artery's interior, accumulating lipids and other substances that form plaque [19]. The clinical method of assessing trans-stenotic pressure is catheterization which can be performed using either a wire or a more commonly employed catheter [14]. Generally, these devices necessitate vascular access through either the femoral or brachial artery and then undergo precise navigation to reach the specific region of interest. Consequently, this procedure is classified as an invasive medical intervention [20]. Figure 1.7 presents an example of femoral catheterization for measuring the trans-stenotic pressure drop (ΔP) between proximal P_1 and distal P_2 of a carotid stenosis.

Due to the highly invasive nature of catheterization, there are potential complications associated with the procedure, such as bleeding or hematoma formation at the site of insertion, infection, arterial damage and allergic reactions to contrast media. Additionally, catheterization often requires the use of ionizing radiation for guidance during angiography. Given the possibility of such consequences, safely and effectively performing the procedure can be challenging. To address these concerns and minimize costs and clinical side effects, non-invasive methods that utilize blood flow imaging, such as echocardiography or PC-MRI, are preferred alternatives for assessing intravascular pressure.

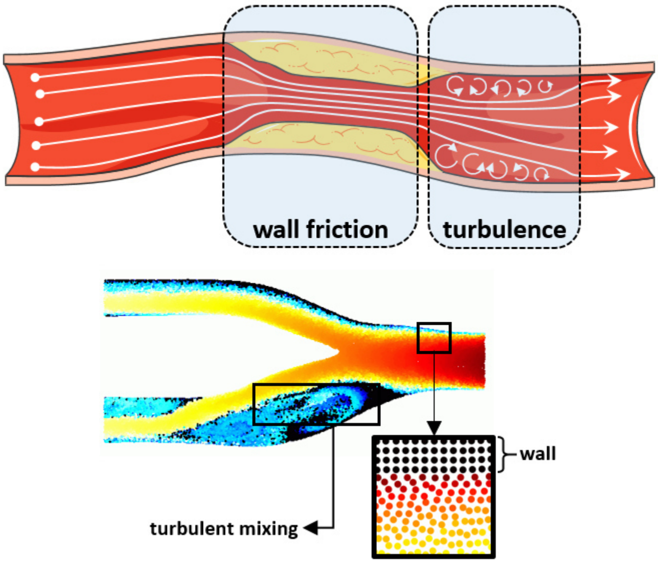

Figure 1.6: Energy loss in arterial stenosis with wall friction and turbulence caused due to the abrupt change in flow geometry.[4]

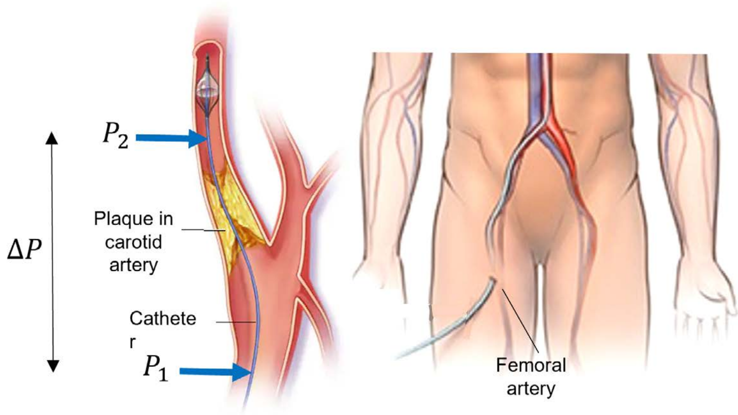

Figure 1.7: Femoral catheterization in carotid artery stenosis for trans-stenotic pressure measurement.[5]

Medical imaging plays a significant role in providing a direct visual assessment of stenosis degree and understanding the physical state of stenosis through the analysis of geometric features presented in corresponding images, particularly in cases where the stenosis has progressed to a high degree of occlusion, resulting in symptoms. However, traditional medical imaging methods are limited in their ability to provide information on the hemodynamic aspects of stenosis. Therefore, in addition to the necessity of obtaining information on the hemodynamic functionality of blood flow, there is a pressing need for a method capable of estimating stenosis in its mild to moderate stages, where symptoms may not yet be apparent, and visual detection of occlusion may be challenging. To acquire this information, it is essential to initially estimate the intravascular velocity field through imaging techniques and subsequently employ

[4] https://www.biomecardio.com

[5] https://www.hopkinsmedicine.org

fluid dynamics equations to estimate the trans-stenotic pressure drop.

The color Doppler mode of imaging is particularly advantageous for this purpose, as it is widely accessible, compatible with routine clinical practices, and offers ease of use and rapid implementation. Therefore, it serves as a suitable modality for acquiring the necessary data.

In this study, our objective is to develop and investigate the feasibility and applicability of a non-invasive technique utilizing clinical color Doppler imaging to estimate the trans-stenotic pressure loss in mild to moderate cases of carotid artery stenosis. This estimation will facilitate the evaluation of stenosis severity, enabling earlier diagnosis.

Chapters 2 and 3 of this study will present a comprehensive review of cutting-edge blood velocity imaging techniques, along with the corresponding fluid dynamics equations for cardiovascular pressure estimation. We will also emphasize our contribution to the advancement of research in this field.

2

State-of-the-Art of Blood Velocity Imaging Techniques

This chapter presents an overview of blood velocity imaging techniques, mainly magnetic resonance imaging and ultrasound imaging, outlining their pros and cons. Phase contrast MRI utilizes the magnetic properties of body atoms to measure blood flow, while ultrasound imaging uses sound waves, employing methods like blood speckle tracking and echocardiographic particle image velocimetry to estimate blood velocities. The primary mode for measuring blood flow velocity in ultrasonography is the Doppler mode, which includes pulsed-wave and color Doppler. The chapter also introduces particle image velocimetry as a method for measuring fluid flow velocities.

Contents

In this chapter, we investigate the details of two primary imaging modalities for blood flow imaging: phase contrast magnetic resonance imaging (PC-MRI) and ultrasound imaging. We will explore the various techniques associated with each modality, revealing the strengths and challenges they present in the field of blood flow imaging. We will shed light on the state-of-the-art developments for each method within this context. Subsequently, we will elaborate on the method that aligns most closely with our study's objectives. We will justify our choice, highlighting the reasons why it distinguishes itself among the available techniques.

2.1 Magnetic resonance imaging

Magnetic resonance imaging (MRI) is a non-invasive medical imaging technique that uses the principles of nuclear magnetic resonance (NMR) to visualize the internal structures of the human body. Its primary physical principles involve the characteristics of hydrogen atoms and their behavior in the presence of a magnetic field. The human body predominantly comprises almost 66% water, which contains a high concentration of hydrogen atoms [21]. Each of them has a single proton in its nucleus that exhibits a property called "spin". Due to their charge and spin, protons generate a magnetic moment, which causes them to behave like tiny magnets.

In a MRI scanner, a strong external magnetic field is applied to align the hydrogen protons magnetic moments along the direction of the field. A short, precisely timed radio frequency (RF) pulse is then applied perpendicular to the magnetic field, causing the protons to absorb energy and flip to a higher energy state. This phenomenon is called "resonance". Once the RF pulse is turned off, the protons gradually return to their original alignment, releasing energy as electromagnetic signals. A receiving coil detects the emitted signals, and the information is then processed using mathematical algorithms like the Fourier transform to reconstruct a detailed image of the internal structures. Then, the intensity of the received signal is plotted on a gray-scale, and cross-sectional images are built up. The phenomena of the orientation of magnetic moments and precession are depicted in Figure 2.1.

Phase contrast MRI (PC-MRI) is a specific application of MRI. It uses the same underlying principles of MRI but focuses on measuring the motion and flow of fluids, particularly blood flow. It uses the phase shifts induced by blood flow to determine the 4D (3D + time) velocity field within the vessels of interest. It applies a gradient to the magnetic field when acquiring the MRI signal. This gradient causes a phase shift in the MRI signal proportional to the blood's velocity. Using a velocity-encoded gradient, the phase shift can be converted to a velocity measurement, allowing the quantification of the flow. It can be performed using a 2D or 3D cine sequence to acquire images over the cardiac cycle. The images are then post-processed to calculate the velocity and flow rate at various locations in the vessel. An example of a three-dimensional blood flow in the thoracic aorta and renal artery stenosis of a patient is visualized in Figure 2.2. While PC-MRI is a valuable diagnostic tool for many medical conditions and allows the visualization of the flow, it also exhibits several disadvantages:

- MRI machines are expensive to purchase and maintain, making them less accessible and not transportable to the patient's bedside. Moreover, due to the limited availability of MRI machines in some medical facilities, patients needing an MRI scan may have to wait on a long waiting list.

- Its lengthy scan time and noise level can be uncomfortable for patients who must remain motionless during the entire acquisition to avoid any reconstruction problem and guarantee a good image quality. In addition, some patients may feel anxious or claustrophobic during an MRI scan, as they must lie inside a narrow enclosed tube.

- The magnetic field can have metal interference for patients with certain types of implants or devices (pacemakers, for example).

Considering the limitations of PC-MRI, for the purpose of blood flow imaging, it is predominantly used in clinical research rather than in routine examinations.

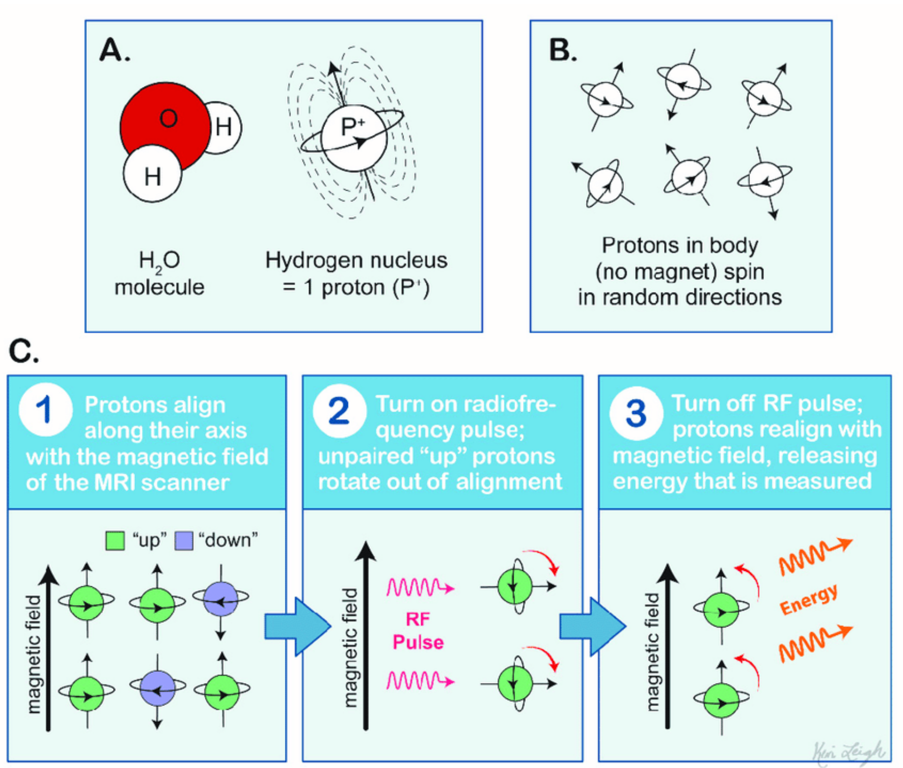

Figure 2.1: Mechanism of magnetic resonance imaging. (A) Hydrogen atoms are dispersed within the patient's tissue with intrinsic spin. (B) Hydrogen atoms are spinning in random directions without alignment with one another. (C) Protons align with the magnetic field in a parallel fashion; after applying a RF pulse, the protons realign with the magnetic field, releasing energy and generating a high-resolution image of the tissue [21].

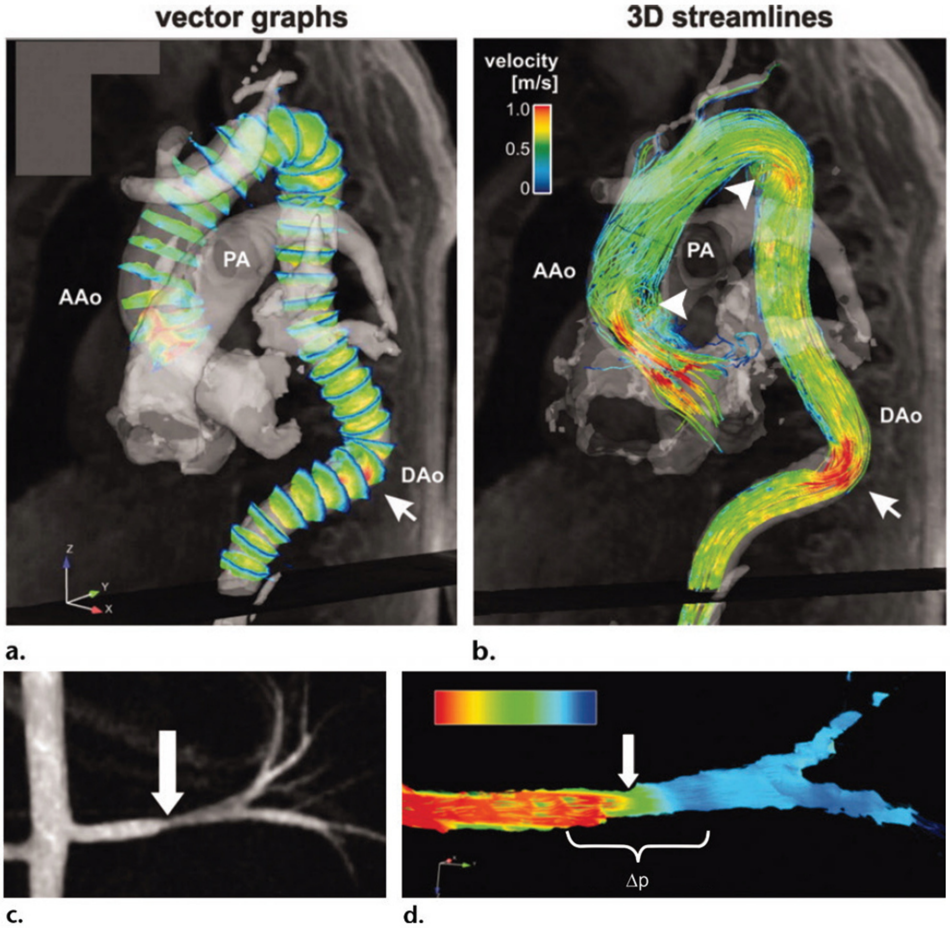

Figure 2.2: (a, b) Three-dimensional blood flow in the thoracic aorta is visualized in a patient using PC-MRI. (a) Vector graphs were used to visualize flow profiles in multiple planes along the aorta. Both the length and the color of the vector represent the local velocity. (b) Three-dimensional streamlines permit visualization of the 3D distribution of systolic velocities in the entire aorta. AAo = ascending aorta, PA = pulmonary artery, DAo = descending aorta. Arrowheads show changes in the velocities in these areas. (c) Shows renal artery stenosis (arrow) in a swine model. (d) Δp = pressure gradient, derived from velocity fields using fluid dynamics equations [22].

2.2 Ultrasound imaging

2.2.1 Physical principle of ultrasound

Ultrasound is a non-invasive imaging modality that employs the principles of sound wave propagation, mechanical waves, through the medium to produce detailed images of internal structures. Unlike audible sound, which the human ear can perceive, ultrasound waves are beyond the audible range and are typically detected using specialized equipment.

At the core of an ultrasound system is a small piezoelectric ceramic, which is placed on a probe and vibrates in response to an electric current, generating these waves. The underlying principle of this imaging technique is to emit these ultrasonic waves from a source and then receive the corresponding echoes, which are produced by "scatterers" or "diffusers" (points in space where the waves encounter different tissues or organs with varying acoustic properties), in all directions by a sensor. Some of these echoes are back-reflected to the probe, while others continue deeper into the body. The piezoelectric ceramic on the probe detects them. It generates an electric current, a RF signal (see Figure 2.3), which is collected and processed by the ultrasound machine to extract the data necessary to create an image. When imaging is performed, a gel is applied to the patient's skin, which helps to eliminate any air pockets between the probe and the skin. This gel also serves as a lubricant, allowing the clinician to adjust the position and orientation of the probe to achieve the best possible imaging results.

Different types of probes are available for ultrasound imaging to fulfill the clinical requirements. The most commonly used probes include the linear, convex, and phased array cardiac probe [23]. The linear probe is utilized for imaging the superficial vessels or tissues such as the carotid artery. On the other hand, the convex probe provides a broader field of view, allowing for better imaging of deeper tissues and organs. Lastly, the phased array cardiac probe is small and square-shaped, allowing it to pass through the ribs and capture a large field of view of the heart that includes all four chambers. Since our study focuses on carotid artery, we will exclusively use linear probes to acquire all our experimental ultrasound images.

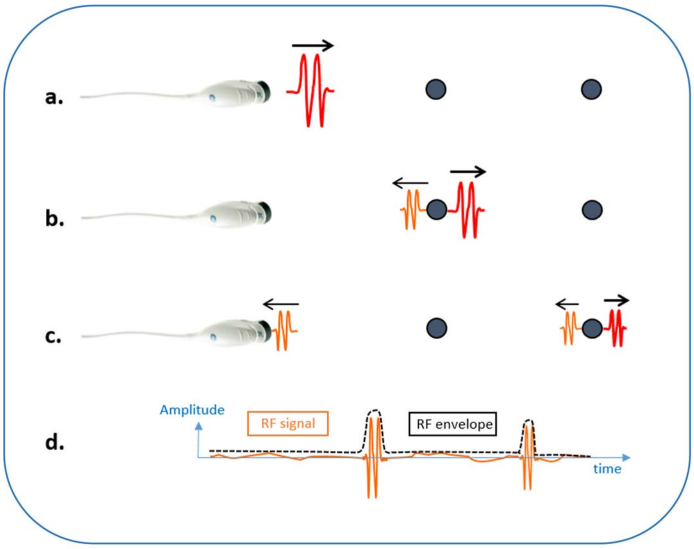

Figure 2.3: Example of propagation of a sound wave in a medium to acquire an image. (a) the transducer emits a short pulse, (b) the sound wave propagates in the medium, (c) reflected waves are received by the transducer, (d) the real envelope of the signal generates an ultrasound image.[1]

2.2.2 Ultrasound image generation

Ultrasound emission: Ultrasound probes used in clinics employ piezoelectric elements individually drive. The number of piezoelectric elements placed behind the acoustic lens in an ultrasound probe depends on the design and intended use of the specific probe type. Ultrasound probes utilize acoustic lenses to concentrate energy in a narrow zone around the image acquisition plane. These lenses can focus the beam into the image plane. During transmission, the delay applied to each element is tailored to the focal point's position. This technique allows elements furthest from the center to be activated first so that their emitted waves converge towards the focal point before diverging once it has passed. This process is illustrated in Figure 2.4.

[1] https://www.biomecardio.com

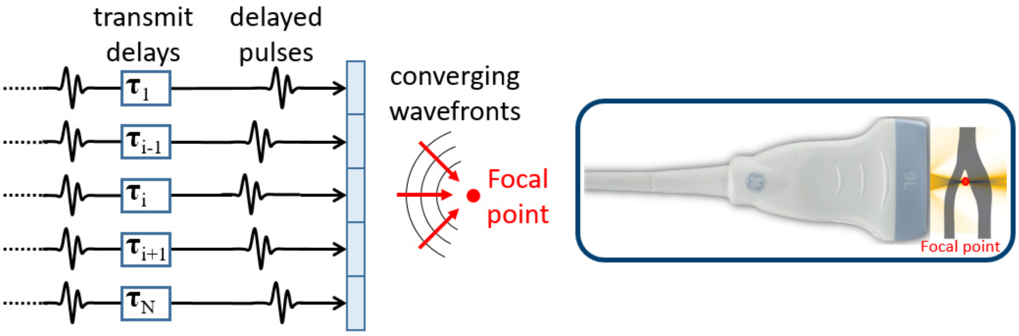

Figure 2.4: Diagram of focused sequences in vascular imaging. (left) Focused ultrasound shot and (right) corresponding sound pressure field.[2]

Ultrasound echo reception: Once the sound echoes from the diffusers hit back to the probe, it causes all the piezoelectric elements of the array to vibrate. These vibrations are converted into an electrical signal, known as the RF signal (see Figure 2.3). To account for the time it takes for the wave to return from the focal point, a delay is applied to each piezoelectric element's RF signal before being summed (Figure 2.5). This technique, called delay and sum (DAS), is widely used in ultrasound imaging [24]. This approach allows for dynamic focusing on reception of the signals, enabling optimal spatial focus on each point for reception.

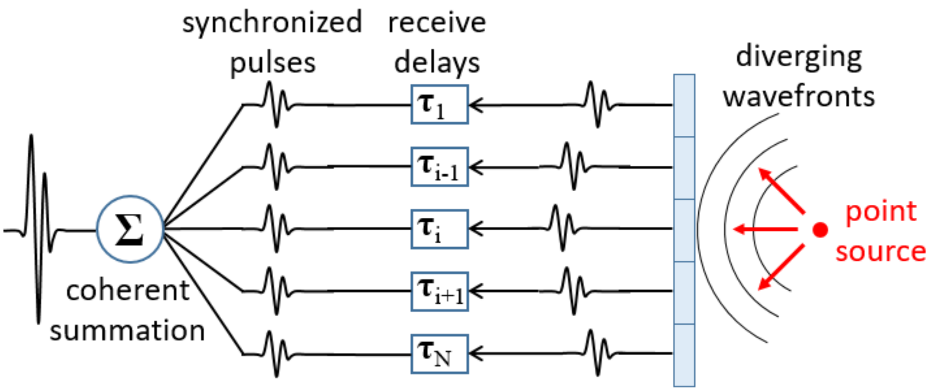

Figure 2.5: Diagram of delay and sum in ultrasound reception.[3]

Image formation: The received RF signals contain both amplitude and phase information. The amplitude information is used for tissue visualization, while the phase information is used to detect blood flow. By adding signal-processing steps to RF signals, the ultrasound machine undergoes in the process of image formation, whereby it reconstructs a grayscale representation of the internal body structure known as a "B-mode" image. Additionally, for the specific task of detecting blood flow, the machine generates "Doppler" signals, which will be explained upon in detail in section 2.2.4. Multiple ultrasonic acquisitions are performed to scan the entire area of interest, with each transmission/reception producing a partial image. These partial images are then integrated to create a complete image of the region-of-interest (ROI). Finally, it is displayed on the machine's screen and further interpreted by a trained healthcare professional. Figure 2.6 depicts an example of a B-mode image of the carotid artery.

[2] https://www.biomecardio.com
[3] https://www.biomecardio.com

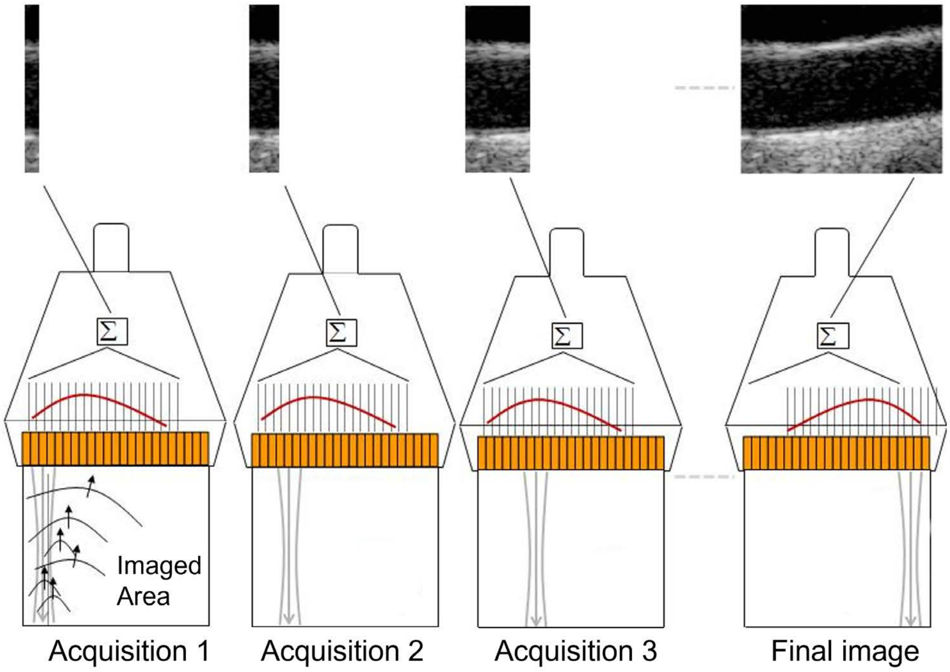

Figure 2.6: An example of conventional focused ultrasound-imaging sequences for a common carotid artery B-mode image. The focus spot is moved for each transmission and reception, in order to generate the full image [25].

2.2.3 Velocity estimation based on B-mode

There are two primary techniques for blood flow imaging utilizing ultrasound B-mode images: "blood speckle tracking (BST)" and "echocardiographic particle image velocimetry (echo-PIV)".

2.2.3.1 Blood speckle tracking (BST)

This is a technique used in ultrasound imaging to visualize and track the movement of blood during the slow time of ultrasound data acquisition. In echography, echoes returning to the transducer during the reception phase are recorded over time to create a series of ultrasound frames. The slow time refers to the duration over which these frames are acquired. The grouping of frames acquired or processed together as a unit during ultrasound data acquisition is called the packet size. In ultrasound images, "speckle" refers to the granular or grainy pattern observed in unfiltered B-mode images, appearing as dark and bright specks. This speckle pattern arises from the interference of sound waves reflected from scatterers present in the body, such as tissues, organs, or blood (Figure 2.7) [26].

Blood speckles are not easily visible in conventional B-mode images. Therefore, to enhance their visibility, clutter filtering is applied to the image. This is necessary to attenuate the strong signal originating from surrounding tissues, such as vessel walls, which can be typically stronger than the signal from blood. Therefore a high-pass filter is utilized to suppress signals from relatively stationary scatterers [27]. Once the speckles become detectable in the filtered image, assuming consistent movement of speckles from frame to frame, a block matching technique is used to estimate the velocity vector field by analyzing consecutive images.

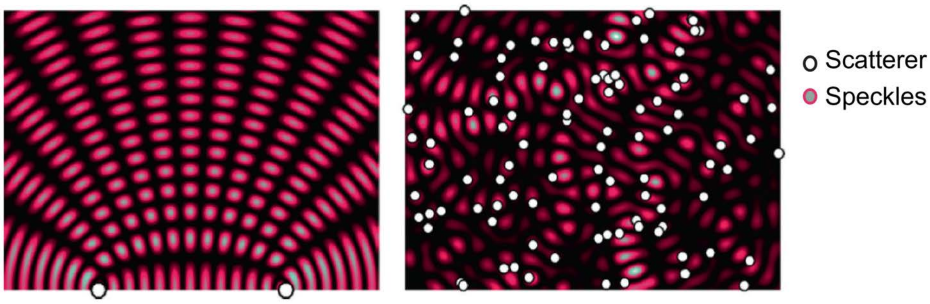

Figure 2.7: Speckle formation. (left) Interferences produced by two scatterers. (right) Speckles produced by the interference of backscattered waves generated by randomly distributed scatterers (white dots) [26].

The block matching technique involves dividing each image into small regions and attempting to find the best match for a corresponding speckle signature in the subsequent frame. By measuring similarity, such as using normalized cross-autocorrelation, each region in the first image is paired with the most similar region in the second image. This enables the determination of average particle displacement within that region. Dividing the displacement by the time elapsed between the two images yields the average velocity of the particles in that region (Figure 2.8) [28].

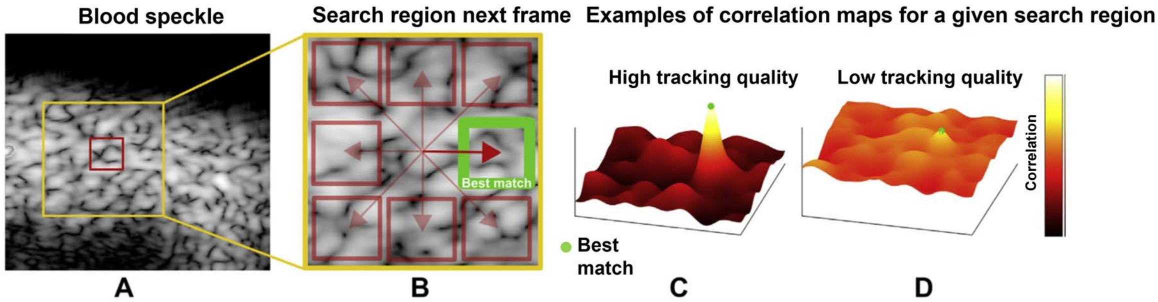

Figure 2.8: Speckle-tracking and tracking quality (TQ). A kernel is defined in the first frame (A), and the best match of this kernel is searched for in the next frame (B). If the best match can be clearly distinguished from the alternative matches, as shown in (C), the TQ is high. In contrast, if there is little difference between the best match and the alternative matches, the TQ is low (D). (TQ is a measure of the difference in correlation between the best match and the alternative matches in a search area) [28].

Figure 2.9 shows an example of estimated velocity field using BST technique in the left ventricle of a 9-year-old healthy child [28] and Figure 2.10 illustrates using this method to estimate 2D velocity vector field in a simulation of carotid bifurcation [29]. A significant limitation in employing the BST technique is its requirement for wall filtering, which necessitates raw ultrasound data. However, such data is not typically available from clinical scanners. While research scanners to which we have access do provide raw data, they do not have the necessary standards for patient application. Consequently, this method is predominantly used in clinical research, rather than routine clinical practice [30].

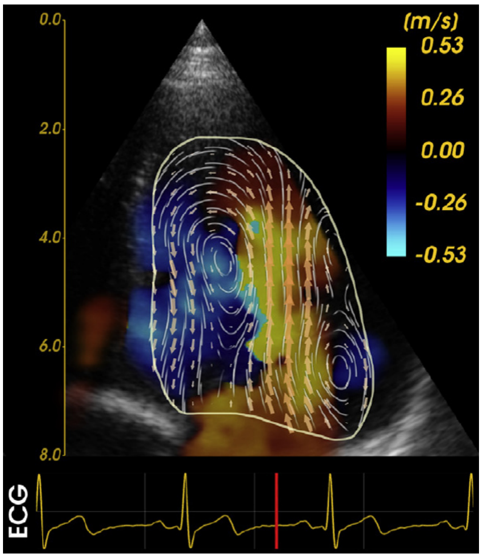

Figure 2.9: Intraventricular velocity field was reconstructed using the BST method in the left ventricle of a healthy 9-year-old child, including relevant information about the cardiac wall [28].

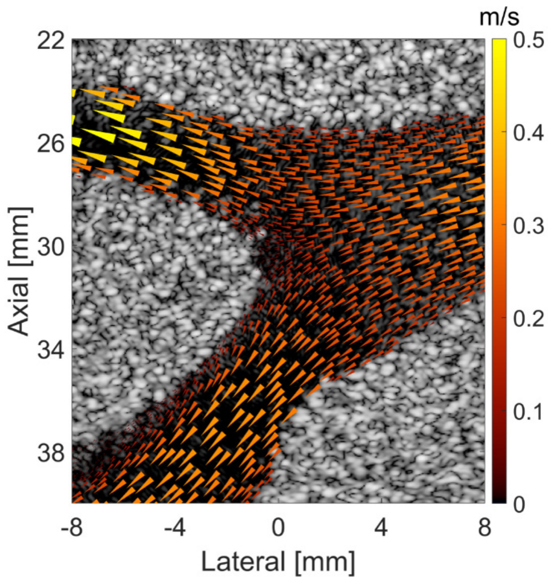

Figure 2.10: B-mode image superimposed with the flow estimate for a simulation of carotid bifurcation during systole using BST technique [29].

2.2.3.2 Echocardiographic particle image velocimetry (echo-PIV)

The concept of this imaging technique originated from the classical particle image velocimetry (PIV) technique, widely used in experimental fluid dynamics to measure two or three velocity components in a flow (detailed explanation in section 2.3). This technique shares similar principles with BST, but with the added advantage of utilizing ultrasound contrast agents, composed of gas encapsulated within a hydrophilic shell, in the form of microbubbles injected into the bloodstream. The presence of these microbubbles enhances the contrast of B-mode images, facilitating the application of block matching through normalized cross-correlation, similar to BST, for estimating the velocity vector field. Like other techniques, regularization or smoothing can be applied to eliminate outliers [26, 31]. Figure 2.11 illustrates an example application of echo-PIV in visualizing intraventricular vortices within the human heart [26]. However, the clinical adoption of this method is hindered by its reliance on an experienced clinician for gas injection, which requires additional time and coordination. Consequently, echo-PIV is primarily employed in research settings to investigate blood flow dynamics within the left ventricle [32, 33].

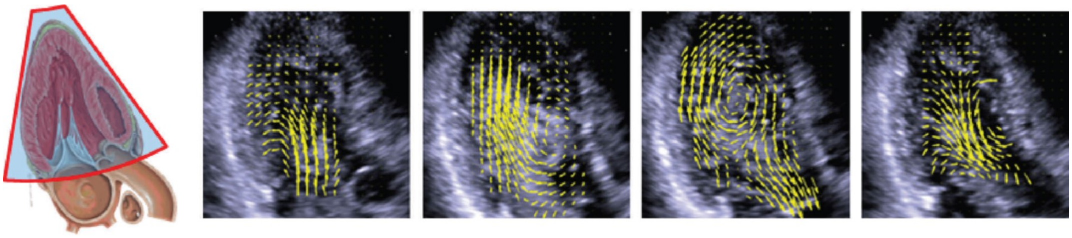

Figure 2.11: Sample application of echo-PIV in the human left ventricle [26].

2.2.4 Velocity estimation based on Doppler

Doppler mode in ultrasonography is a specialized imaging technique that utilizes the Doppler effect to detect and analyze the velocity and direction of blood flow within the body. The Doppler effect is a physical phenomenon that occurs when relative motion between the ultrasound probe and moving red blood cells occurs. In this mode, the ultrasound probe emits high-frequency sound waves that bounce off moving cells in the vessel. The probe then detects the echoes of the sound waves and measures the frequency and phase shift. Consequently, it returns the blood velocity projection along the ultrasound wave's propagation axis. If an ultrasound beam propagates in the same direction as the blood flow, the Doppler shift is proportional to the displacement velocity of the scatterer, resulting in a measured Doppler velocity. Conversely, if they are perpendicular, no Doppler shift is perceived. The measured Doppler velocity depends on the angle between the flow direction and the ultrasound axis which highlights the importance of obtaining an accurate angle correction when interpreting Doppler signals (see Figure 2.12).

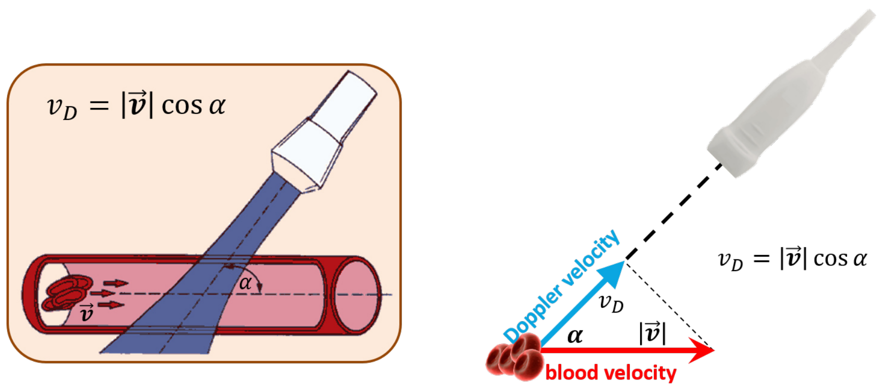

Figure 2.12: Principle of measurement of axial velocity using the Doppler effect.[4]

[4]https://www.biomecardio.com

In our research, we have focused on employing the color Doppler mode, which operates on the same physical principle as the pulsed-wave Doppler method. These two modes are widely used for evaluating blood flow velocity in ultrasound imaging. Consequently, in this manuscript, we will exclusively introduce and discuss these two modes.

Pulsed-wave Doppler: This mode is a velocity distribution analysis technique that allows users to select a sample volume based on the B-mode image (see Figure 2.13). It uses successive pulses in the same direction, with a limited pulse repetition frequency (PRF) to avoid echo confusion. Fourier Transform is used to compute the velocity distribution within the selected sample volume. The PRF in ultrasound imaging is the number of pulses of a repeating signal in a specific time unit. It represents the rate at which ultrasound pulses are emitted and received during the data acquisition process. This method allows for precise measurements at every point along the imaged axis. However, it is susceptible to spectral overlap or aliasing. Aliasing is a well-known phenomenon in Doppler imaging that occurs when Doppler frequency exceeds half of the PRF. In such instances, sampled frequencies might appear as negative frequencies, resulting in a reversal of the flow direction. This results in an underestimation of the true velocity of blood flow, where higher speeds appear as lower velocities in the opposite direction (Figure 2.14) [23].

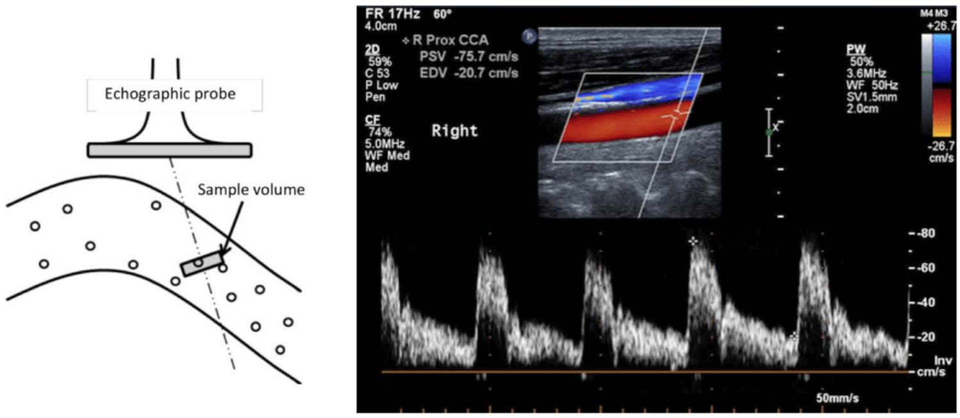

Figure 2.13: (left) Diagram of PW Doppler sample volume location. (right) Sample volume selection in B-mode and corresponding PW Doppler analysis of blood flow in the common carotid artery [23].

This limit velocity, beyond which there is aliasing, is called Nyquist velocity, which specifies the minimum sampling rate required to avoid it. The formula for estimating velocity highlights the relationship between Doppler velocity and Nyquist velocity (Equation (2.1)):

$$v_D = \frac{c \times PRF}{4 f_0} \frac{\Delta\phi}{\pi} = v_N \frac{\Delta\phi}{\pi} \tag{2.1}$$

where v_D is the Doppler velocity, c is the velocity of the ultrasound wave in the body (about $1540\ \mathrm{m \cdot s^{-1}}$), f_0 is the frequency of the wave sent by the probe, $\Delta\phi$ is the phase shift and v_N is the Nyquist velocity. Since the phase shift is between $-\pi$ and π, hence $v_D \in [-v_N; v_N]$.

Color Doppler: This mode allows for real-time visualization of bloodstreams as a color image. It provides a velocity-related information for a whole region of interest, rather than just a sample volume, using color-coding to represent the speed and direction of the flows superimposed on the grayscale B-mode image (Figure 2.15): blue indicates flows moving away from the probe, while red indicates flows approaching the array. In addition, the intensity of color is proportional to the blood flow velocity. Lighter colors correspond to higher speeds, whereas darker ones indicate lower velocities [23]. In this method, the velocity estimation principle utilized in pulsed-wave Doppler is extended to each image pixel, enabling real-time visualization of flow maps. The color Doppler mode has emerged as a common diagnostic tool for the assessment of vascular and cardiovascular diseases, owing to its accessibility and ability to provide real-time visualizations.

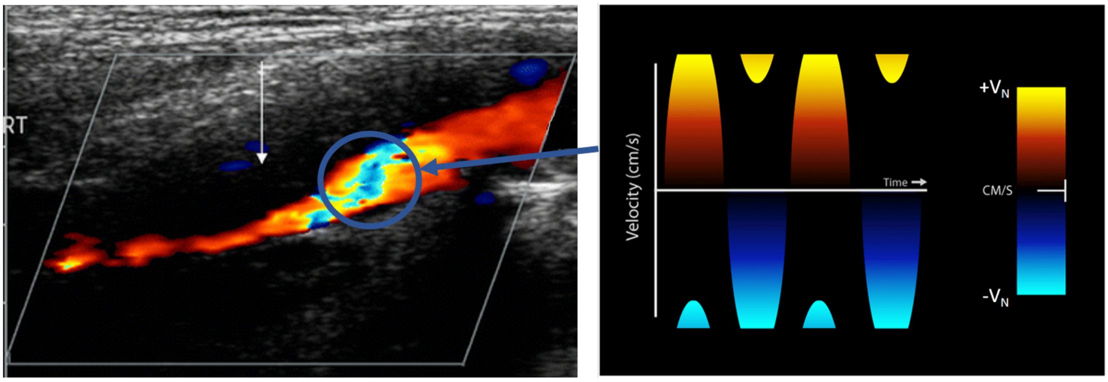

Figure 2.14: A clinical Doppler image of the carotid, with aliasing on the left. The color scale illustrates the effect of aliasing.[5]

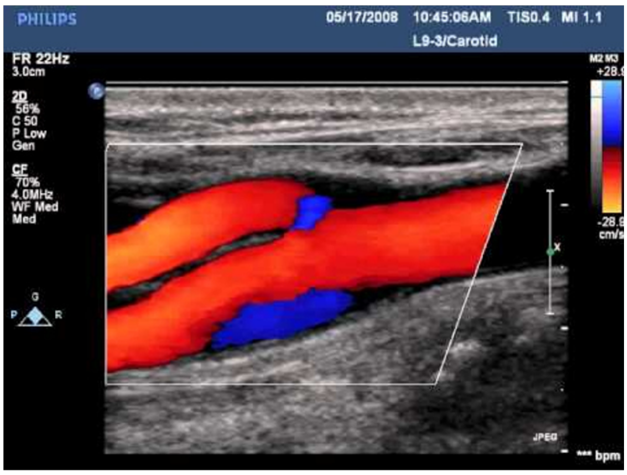

Figure 2.15: Example of color Doppler imaging in carotid bifurcation.

2.2.4.1 Vector flow imaging (VFI)

Both spectral and color Doppler modes in conventional Doppler ultrasound provide scalar fields that map the components of blood velocities along the ultrasound axes. However, in order to comprehensively analyze the cardiovascular flow from different hemodynamic perspectives, it is essential to extract a velocity vector field. To address this challenge, extensive research has

[5] https://www.biomecardio.com

been conducted to develop approaches for blood velocity vector flow imaging (VFI) [31] with the aim of capturing and visualizing the complete velocity vector information of blood flow.

One of the early approaches developed in this regard is the cross-beam Doppler or multi-beam Doppler [34] technique which is based on combination of different Doppler data. This technique involves emitting multiple ultrasound beams from different angles and acquiring Doppler echo returns. The resulting echoes provide projections of the blood velocity vector from various angles, which are then used to derive the flow vector information. Despite their initial success, the limitations of such a system were apparent. Manual adjustment of the beam orientation was required for vessels at different depths. However, maintaining coplanarity between the transducers and vessels proved challenging [35].

To address this limitation, a technique known as multi-angle Doppler estimation for plane-wave VFI was developed [36]. This technique expands the framework by incorporating more than two transmit-receive angle pairs and utilizes multiple transmits and multiple sub-apertures during beamforming. By acquiring data in different planes, the estimation of flow vectors can be reformulated as an overdetermined system of equations. However, despite their potential benefits, these techniques have not been implemented in medical ultrasound devices for routine clinical applications. Moreover, while research scanners are capable of executing these techniques, they do not have the medical standards necessary for patient application [31], thus restricting its current application to clinical research purposes.

To mitigate the beam-to-flow angle issue in color Doppler, several techniques have been proposed to drive vector velocity field especially in ultrafast ultrasound (see Figure 2.16) [37, 38]. One of these techniques is transverse oscillation (TO). This approach is based on beamforming of color Doppler images [39]. In a conventional ultrasound system, the pulse-echo field oscillates solely in the axial direction along the ultrasound beam axis which provides no information about the transverse velocity component. To overcome this limitation, a new pulse-echo field is generated in the TO method to introduce phase information in the lateral direction. Figure 2.17 illustrates an example of its application in carotid bifurcation [13].

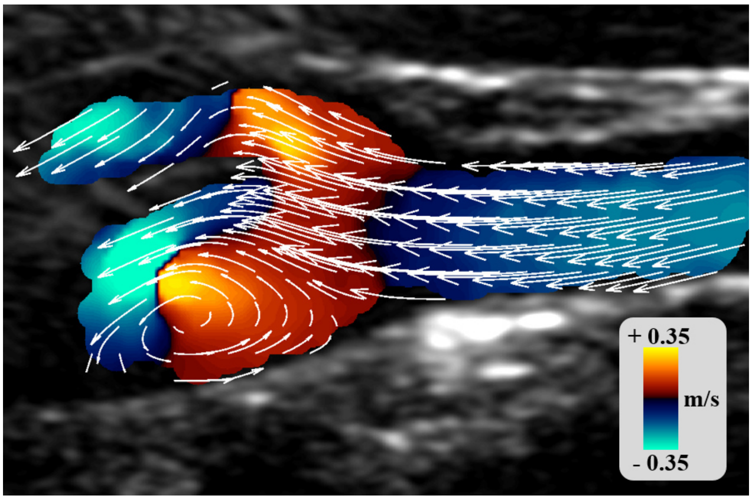

Figure 2.16: Example of vector flow imaging by high-frame-rate plane wave imaging in a carotid bifurcation [38].

This method exhibits sensitivity to the angle between the ultrasound beam and the flow direction [39]. Furthermore, it requires specialized scanners, which are not typically utilized in routine clinical practice. For the purpose of this study, our focus was directed towards traditional scanners, which are more widely available.

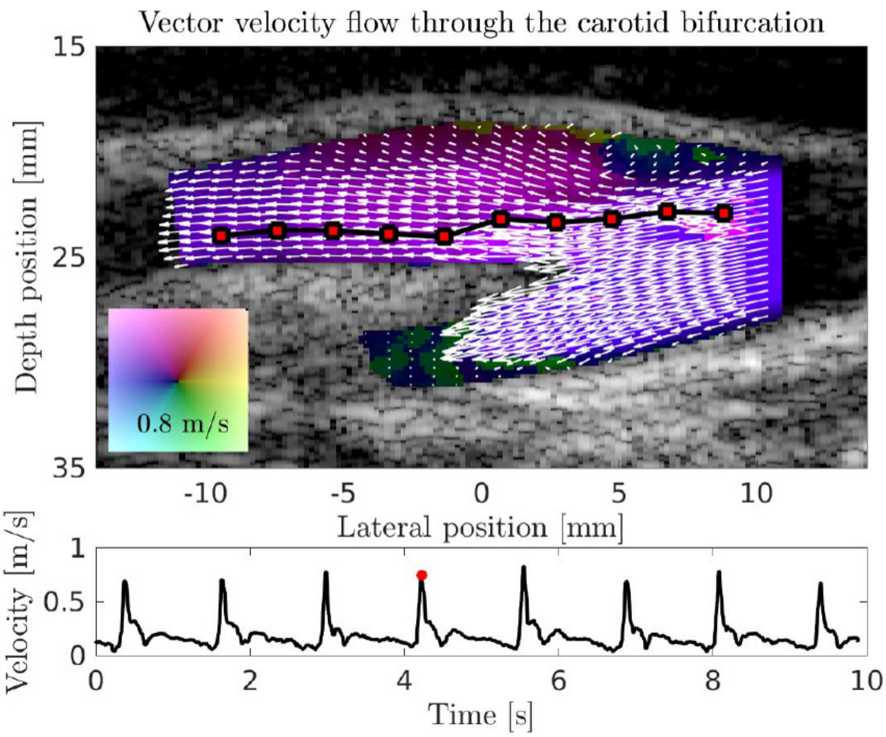

Figure 2.17: An example of vector flow scan in a long axis view of the carotid bifurcation during peak systole obtained with TO strategy. A streamline following the vector velocity field in the internal carotid artery at the level of the carotid bulb is also displayed. The arrows show flow direction and magnitude, and the color shows the velocity angle [13].

Next approach is the color-Doppler-based vector flow mapping, which involves the post-processing of color Doppler images [31]. These methods are grounded in physical constraints. For instance, Garcia *et al.* [40] assumed that blood behaves as an incompressible fluid, where zero divergence is enforced by mass conservation. By combining color Doppler velocities with left ventricle wall positions, they solved the continuity equation to construct a two-dimensional time-resolved (2D + t) velocity field of blood within the left ventricle from conventional transthoracic clinical acquisitions (Figure 2.18). Subsequently, Assi *et al.* [41], Vixège *et al.* [42] and Antonuccio *et al.* [43] proposed incorporating the continuity equation, wall slip conditions, and a smoother to estimate the intraventricular and abdominal aorta velocity field. The problem is formulated as a cost function that is minimized, wherein this cost function contains quadratic regularization terms [41, 43] or constraints terms [42] (Figure 2.19). Figure 2.20 depicts an example result of employing intraventricular vector flow mapping (*i*VFM) technique in left ventricle in one cardiac cycle of a patient.

The widespread availability of conventional color Doppler ultrasound devices in routine clinical settings establishes them as one of the preferred tools for echographic imaging. Furthermore, health professionals well trained in the operation of these devices. Inspired by the *i*VFM method, which focuses on retrieving the intraventricular velocity vector field, we decided to develop an intravascular version. This adaptation aims to enable the derivation of velocity vector fields within vascular regions.

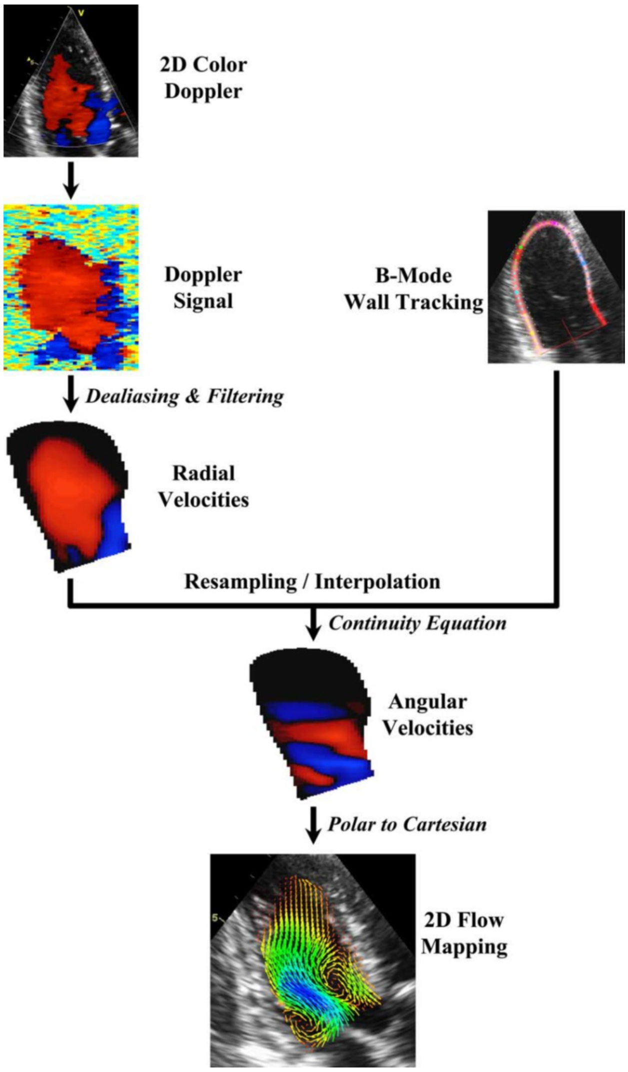

Figure 2.18: Flowchart of the method of Doppler and B-mode acquisitions and digital image processing for the reconstruction of the blood velocity vector field in left ventricle [40].

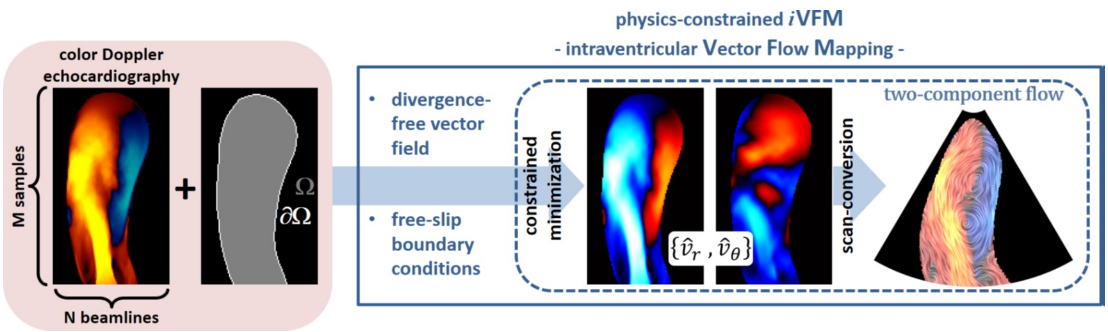

Figure 2.19: The *i*VFM algorithm, constrained by mass conservation and no-penetration conditions, minimizes in the polar coordinate system with pre-scan conversion color Doppler velocities. Ω and $\partial\Omega$ represent the region of interest and the boundary, respectively [41, 42].

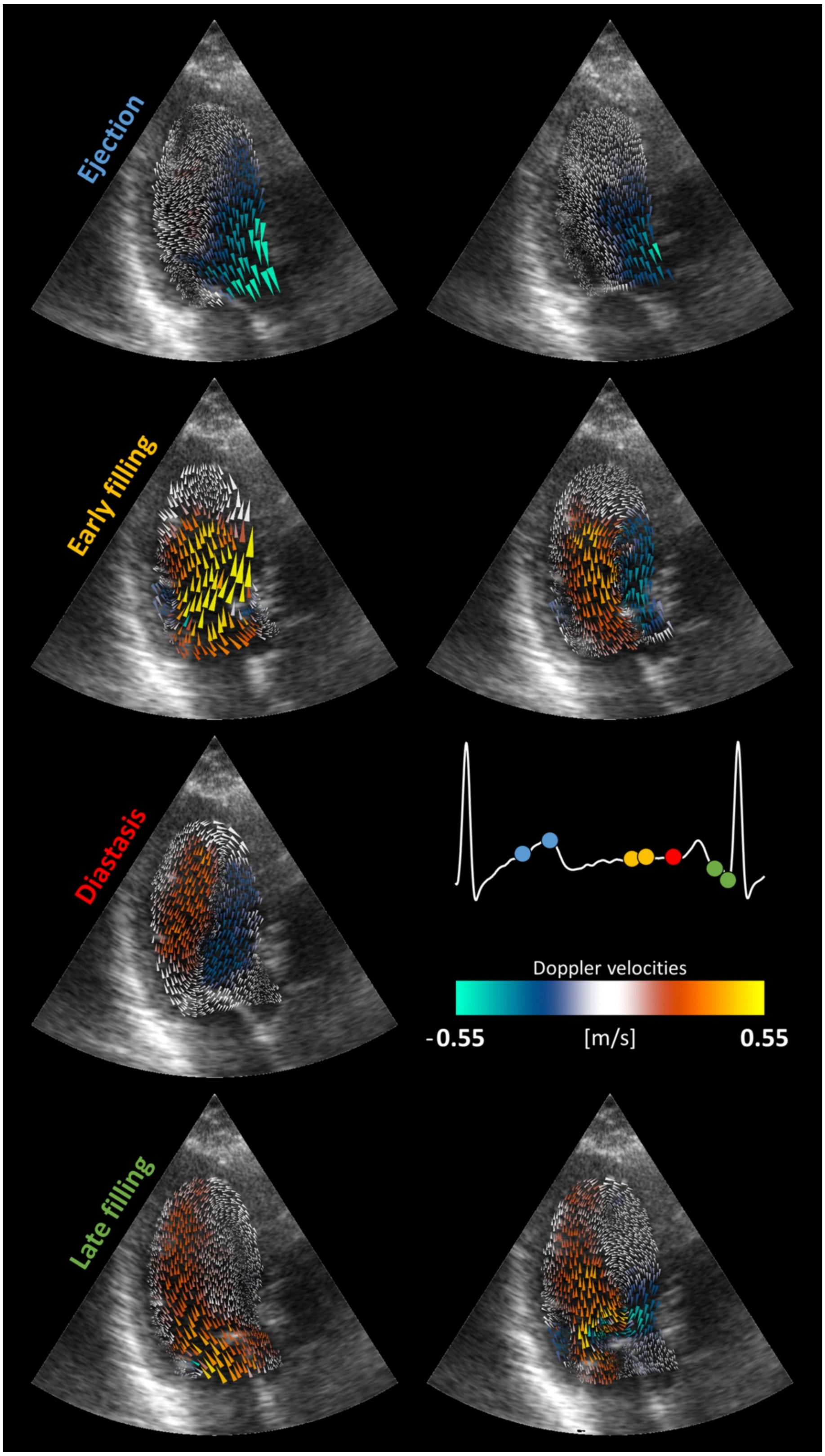

Figure 2.20: An example of blood flow dynamics during a cardiac cycle in a left ventricle of a patient derived from *i*VFM [42].

2.3 Particle image velocimetry (PIV)

Particle image velocimetry (PIV) is an experimental technique that allows for the accurate measurement of fluid flow velocities. It works by introducing small tracer particles into the flow and illuminating them with a laser sheet. The motion of the particles is captured using a high-speed camera, and the displacement of the particles between two consecutive frames is used to estimate the velocity vectors of the flow field (see Figure 2.21) [44].

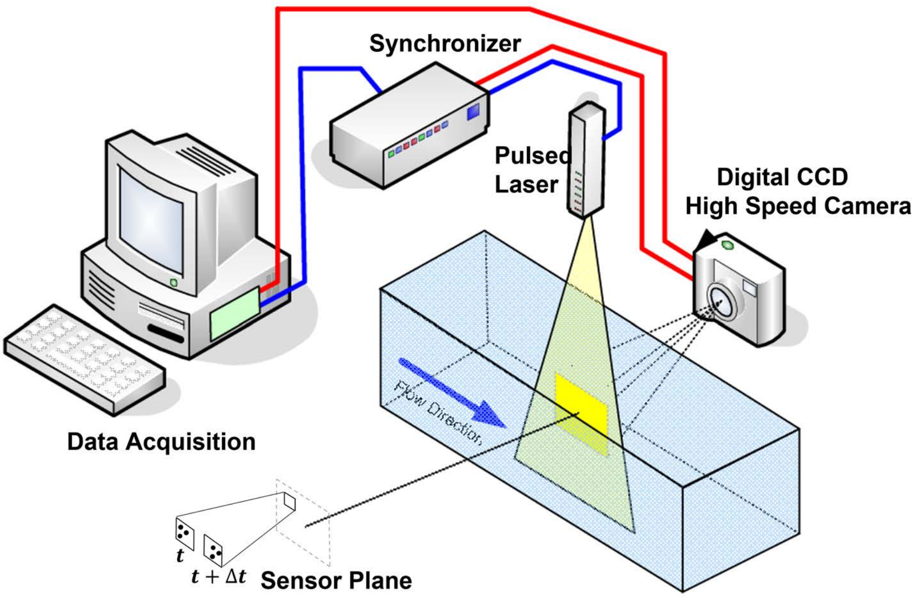

Figure 2.21: Diagram of the key components of a standard PIV system [45].

PIV has found numerous applications in fluid mechanics research, ranging from fundamental studies of turbulent flows to the investigation of flow in complex engineering systems. In recent years, PIV has become increasingly popular due to advancements in camera and laser technology, which have made the technique faster, more accurate, and more versatile.

Due to its high accuracy in estimating the velocity vector field of fluid flow and its ability to provide a clear and nearly precise flow pattern, this method has emerged as widely employed tool in numerous *in vitro* studies examining different hemodynamic aspects of cardiovascular flow. For instance Leinan *et al.* [46] assessed flow patterns in a left ventricular outflow tract phantom. Adopting from this optical technique, the echo-PIV imaging method was developed for non-invasive *in vivo* assessment of blood flow dynamics, as discussed in section 2.2.3.2 of this manuscript. Additionally, DiCarlo *et al*. [47] and Buchmann *et al*. [48, 49] utilized PIV to investigate the impact of carotid stenosis severity on wall shear stress, flow disruptions, and hemodynamic features of a human carotid bifurcation model. Similarly, Johari *et al.* [50] and Bale-Glickman *et al.* [51] conducted experiments on flow characteristics in replica phantoms of atherosclerotic carotid bifurcation (Figure 2.22).

Stereoscopic particle image velocimetry (SPIV) [52] is an advanced PIV technique that is commonly used in fluid mechanics research. Unlike conventional PIV, which employs a single camera to capture two-dimensional velocity measurements of particles illuminated by a laser sheet, SPIV requires two cameras positioned at different angles to capture simultaneous but distinct off-axis views of a designated region of interest. This setup enables the extraction of out-of-plane particle motion. By comparing the images recorder from different angles, the dis-

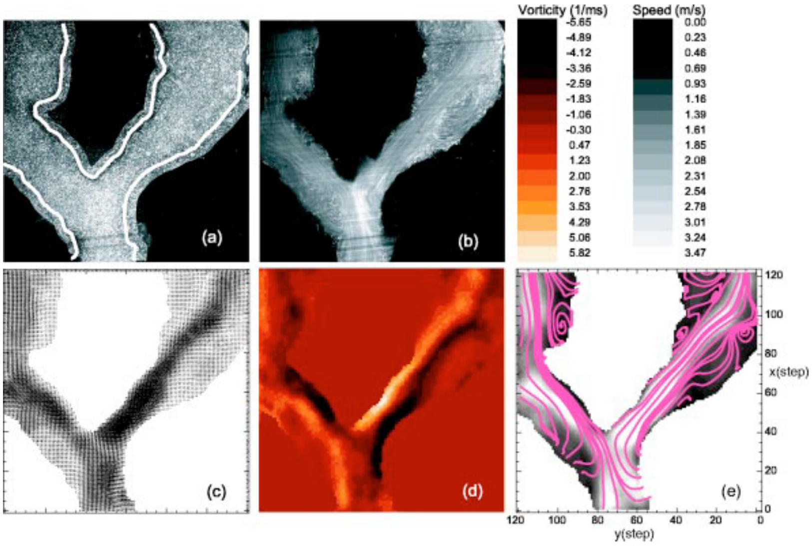

Figure 2.22: Sample flow illustrating PIV data analysis. (a) Extended PIV image. (b) Streaklines from continuous wave laser flow visualization experiments. (c) Velocity vector field. (d) Vorticity. (e) Streamlines on speed field; an alternate presentation of the velocity field [51].

placement of particles over time can be tracked in three dimensions, allowing the determination of the velocity vector field in three dimensions which enables a more comprehensive analysis of the flow. SPIV has been employed by researchers to measure velocity fields in various fluid flow applications [53]. Geoghegan *et al.* [54], for instance, utilized this technique to investigate the flow behavior in a simplified model of a stenotic artery *in vitro* (see Figure 2.23). Additionally, Deplano *et al.* [55] used SPIV to analyze vortical structures in abdominal aortic aneurysms.

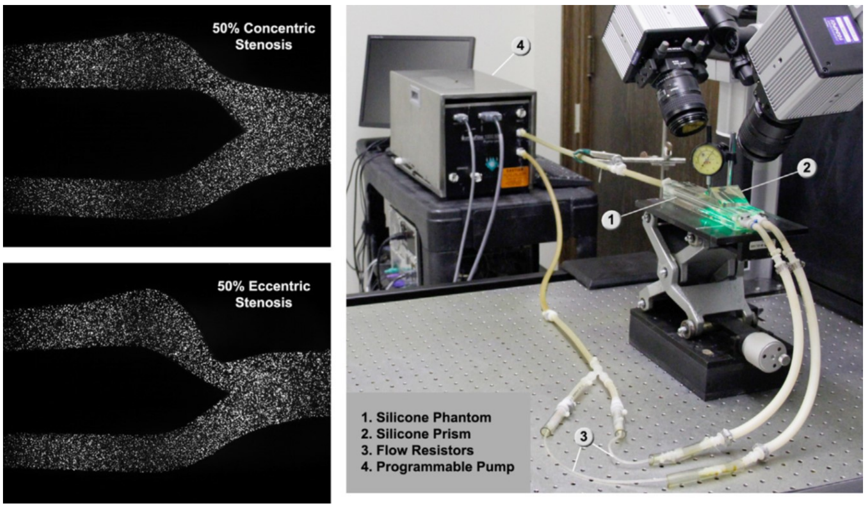

Figure 2.23: Experimental PIV flow measurement setup using a stereoscopic camera arrangement. Planar images capture the stream-wise flow direction as shown in the examples on the left from 50% concentrically (top) and 50% eccentrically (bottom) stenosed models [53].

The non-intrusive characteristic of PIV facilitates high spatial and temporal resolution measurements of the instantaneous velocity field with minimal perturbation to the flow. While its direct application in medical imaging is limited (as discussed in section 2.2.3.2), is widely recognized as a benchmarking tool in the field of fluid mechanics. This makes it an ideal method for validating other velocity measurement techniques.

Upon investigating the main blood flow imaging techniques in this chapter, the one that aligned with the objective of our study was the *i*VFM method, as developed by Assi *et al.* [41] and Vixège *et al.* [42]. Their work inspired us to develop the vascular vector flow mapping (*v*VFM) technique for estimating vascular velocity vector fields. A comprehensive description of this method will be provided in Chapter 4 of this manuscript. By estimating the 2D velocity vector field using *v*VFM from the color Doppler scalar field, to achieve the objective our study, we needed fluid dynamic equations to estimate the trans-stenotic pressure drop in vascular stenosis. Therefor, having illuminated our approach to blood flow imaging, the next chapter will review state-of-the-art for estimating intravascular pressures in this context.

Given the advantages of the PIV imaging method, discussed in this section, several studies using MRI have employed PIV as a validation method [56, 57]. However, extracting the velocity vector field from clinical color Doppler ultrasound imaging poses significant challenges, which have limited previous investigations in their ability to use PIV as a validation method for pressure drop estimation alongside conventional color Doppler imaging. Considering the development of our *v*VFM algorithm, we chose PIV as an *in vitro* validation method for our non-invasive technique to confirm accuracy and reliability of our proposed technique.

3
State-of-the-Art of Non-invasive Pressure Estimation Methods

This chapter introduces various methodologies for the non-invasive estimation of relative cardiovascular pressures through fluid dynamics. Several mathematical formulations are highlighted, including the Navier-Stokes equations, the Poisson pressure equation, the Bernoulli principle, and the work-energy equation. The chapter also discusses the advantages and challenges associated with each method. In conclusion, it determines which method provides the most accurate estimation of trans-stenotic pressure drop.

Contents

As the objective of our study is to non-invasively estimate the trans-stenotic pressure drop using color Doppler images, our attention is necessarily directed towards methods applicable within this context. This focus requires the application of fluid dynamics equations that define the relationship between velocity and pressure [58]. In this chapter, we introduce the fundamental fluid dynamics equations relevant for pressure estimation. For each equation, we provide a detailed exploration of its use in current state-of-the-art. This includes highlighting how these equations have been utilized to develop methods for estimating intravascular pressure drops. Furthermore, we discuss the advantages and limitations of each method within the specified context. Following this, we detail the method we propose, based on these fluid dynamics equations, for determining post-stenotic pressure losses in arterial stenosis. We justify our choice of this approach and explain how it can effectively serve to fulfill the aim of our study.

3.1 Navier-Stokes equations

The Navier-Stokes equations are a set of partial differential equations that govern the behavior of fluid flow [59]. They describe the conservation of mass and the conservation of linear momentum within a fluid. The conservation of mass, also known as the continuity equation, states that the rate of change of density with respect to time, plus the divergence of the mass flux vector, must be equal to zero. Mathematically, it can be expressed as follows:

$$\frac{\partial \rho}{\partial t} + \nabla \cdot (\rho \overrightarrow{V}) = 0 \tag{3.1}$$

here ρ represents the density of the fluid, t is time, "$\nabla \cdot$" is the divergence operator, and $\overrightarrow{V}$ is the velocity vector of the fluid. This equation reduces to ($\nabla \cdot \overrightarrow{V} = 0$) for a Newtonian incompressible fluid. With these assumptions, the linear momentum conservation equation of Navier-Stokes can be represented as:

$$\nabla P = -\rho \left(\frac{\partial \overrightarrow{V}}{\partial t} + \overrightarrow{V} \cdot \nabla \overrightarrow{V} \right) + \mu \nabla^2 \overrightarrow{V} + \rho \overrightarrow{g} \tag{3.2}$$

where P is the scalar pressure field, μ is the dynamic viscosity of the fluid, and $\overrightarrow{g}$ denotes the gravitational forces within the vessels which are negligible as patients are typically positioned in a supine posture during imaging scans. In the given equation, the term $\frac{\partial \overrightarrow{V}}{\partial t}$ corresponds to the local acceleration of the fluid representing the change in velocity over time. $\overrightarrow{V} \cdot \nabla \overrightarrow{V}$ is the convective acceleration, accounting for velocity changes induced by the fluid's geometry. Viscosity drag is represented by $\mu \nabla^2 \overrightarrow{V}$ which acts to dampen fluid motion in case of mixing fluid layers and dissipates fluid's energy irreversibly. These equations serve as a cornerstone in the field of fluid dynamics, providing a comprehensive mathematical framework for analyzing and predicting fluid motion. Due to their significance, the Navier-Stokes equations serve as the foundation for various related equations, such as the Poisson and Bernoulli equations, which are derived under different assumptions [60].

Except for a few studies [54, 61], most researchers, when estimating pressure drop, tend to simulate their preferred model and solve the Navier-Stokes equations numerically using Computational Fluid Dynamics (CFD) [18, 62]. Alternatively, they often rely on CFD results as a ground truth for comparing pressure drop estimates obtained from other modalities such as MRI [63] and ultrasound [13]. This approach provides researchers with the opportunity to gain further insights into the hemodynamic characteristics of the flow under ideal conditions, even when employing complex models. Figure 3.1 illustrates an example of pulsatile flow simulated using CFD in a stenotic model, demonstrating the temporal progression of the streamlines. In fluid dynamics, a streamline refers to a line that is tangent to the velocity vector of a fluid flow at any given point.

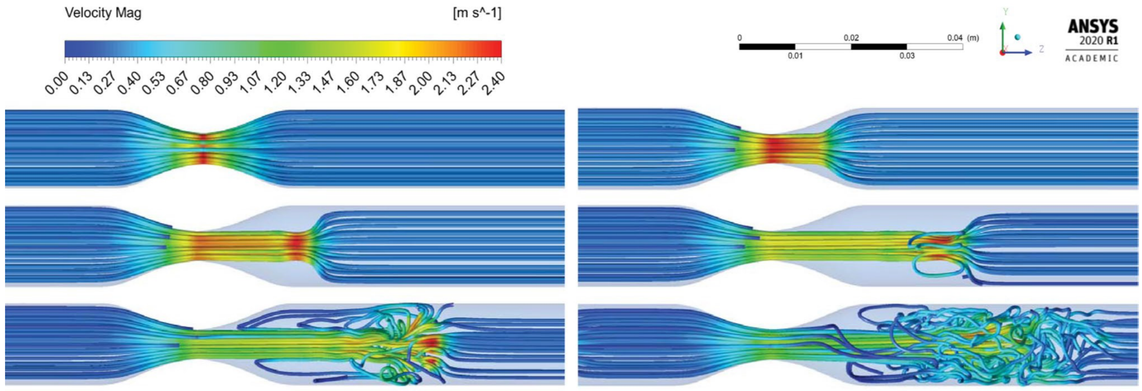

Figure 3.1: The temporal progression of streamlines colored by velocity magnitude in a pulsatile flow, obtained from CFD, is depicted at sequential time points along a flow waveform [63].

3.2 Poisson pressure equation

The Poisson pressure equation is obtained by applying the divergence operator to the Navier-Stokes equation, resulting in the following expression:

$$\nabla^2 P = -\rho \nabla \cdot (\overrightarrow{V} \cdot \nabla) \overrightarrow{V}. \tag{3.3}$$

There are several studies that used this approach for pressure drop estimation in arterial [57,64] or aortic [65] stenosis using acquired velocity from different imaging modalities. Figure 3.2 illustrates the pressure recovery toolchain employed in an aortic stenosis phantom for a 4D MRI flow image related to the study conducted by Nolte *et al*. [65].

Obtaining a solution for this equation relies heavily on accurate segmentation of the region of interest in order to establish the necessary fluid boundary conditions. This includes determining the interaction between the region of interest and its surrounding surfaces, which can be achieved by applying the normal component of the momentum equation on the boundary [57,66]. In practice, this approach is most effective when applied to imaging modalities with high resolution, as it allows for the consideration of the complete vessel geometry. However, accurately capturing the vessel segment around the narrowed site can present challenges [67].

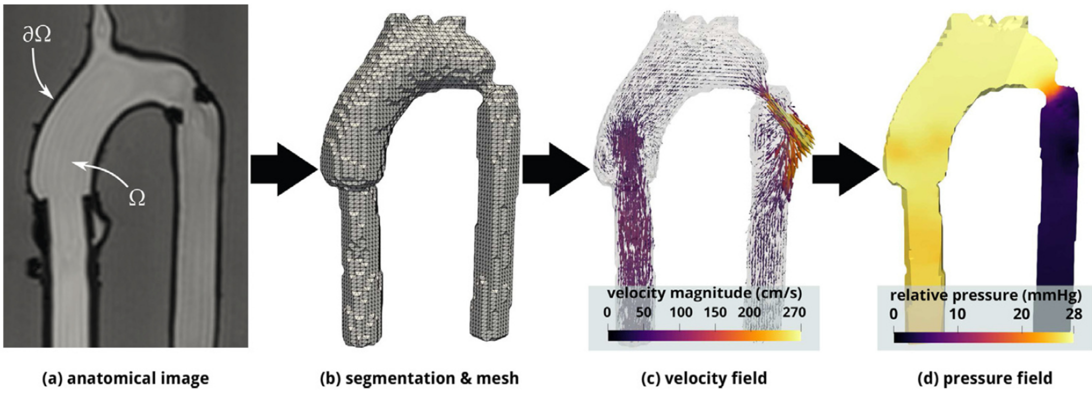

Figure 3.2: Pressure recovery toolchain for a 60% aortic stenosis phantom: (a) Segmentation of anatomic images (shown: a 2D slice of 3D image) identifies the 3D lumen (Ω) and the vessel walls ($\partial\Omega$) averaged over the cardiac cycle. (b) A structured tetrahedral mesh is created from the segmentation. (c) The 4D flow velocity data is represented on the mesh. (d) Relative pressure maps are computed from velocity data [65].

3.3 Bernoulli equation

When considering an inviscid flow, where the dynamic viscosity of the fluid is assumed to be zero, the Navier-Stokes momentum conservation equation can be reformulated into another mathematical representation known as the Euler equation:

$$\nabla P = -\rho\left(\frac{\partial \overrightarrow{V}}{\partial t} + \overrightarrow{V}\cdot\nabla\overrightarrow{V}\right) + \rho\,\overrightarrow{g}. \tag{3.4}$$

In certain studies considering the 1D-flow hypothesis, researchers have used the 1D Euler equation to analyze color M-mode Doppler data for the purpose of measuring intraventricular pressure gradients along the inflow and outflow jets [68–70]. In this framework, Figure 3.3 demonstrates an example of integrating Euler equation along a streamline for intraventricular pressure difference assessment [71].
To express Equation (3.4) following a streamline, Bernoulli equation can be derived as follows:

$$P_1 - P_2 = \frac{1}{2}\rho\,(V_2^2 - V_1^2) + \rho\int_1^2 \frac{\partial V}{\partial t}\cdot dS \tag{3.5}$$

where P_1/P_2 and V_1/V_2 are the upstream (before stenosis) and downstream (post-stenosis) pressures and velocities, respectively, and dS represents the location on the streamline connecting the two points.

Utilizing the PC-MRI blood flow imaging technique, a multitude of studies have utilized the Bernoulli equation as a valuable method for estimating cardiovascular pressure gradients. Notably, researchers have directed their attention towards evaluating pressure loss in arterial stenosis [64] and aortic stenosis [72]. However, this is true if we consider a high severity stenosis, where no pressure recovery is expected post-stenosis. Recently, Kazemi *et al.* [63] used different forms of the Bernoulli equation on 4D flow MRI data obtained from a stenotic phantom model. Their objective was to calculate the pressure drop and subsequently compare it with values derived from CFD simulations and pressure sensor catheter measurements as the established gold standard.

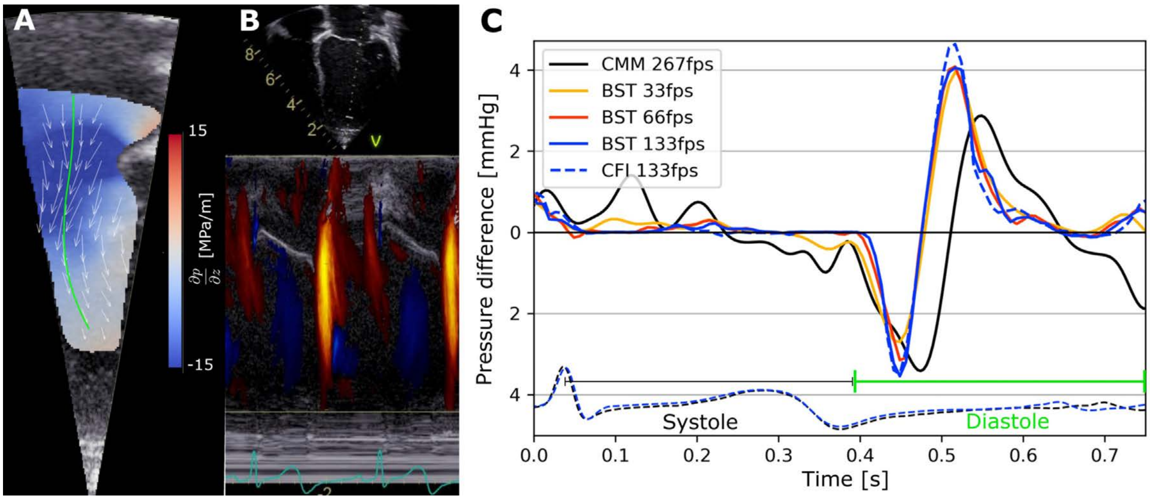

Figure 3.3: Panel A illustrates the flow line utilized for integration in blood speckle tracking (BST). Panel B displays the corresponding color Doppler M-mode (CMM). In Panel C, the intraventricular pressure difference is demonstrated using recordings obtained from BST at various frame rates [71].

Moreover, the application of this method extends to Doppler echocardiography, where it has been used for the estimation of instantaneous pressure gradients across the aortic valve [73]. Furthermore, in investigating instantaneous intraventricular pressure gradients using color Doppler M-mode velocities, researchers have simplified the intracardiac pressure-velocity relationship by neglecting gravitational potential energy and energy losses resulting from viscous dissipation. Consequently, the adoption of the Bernoulli equation has been employed for such calculations [74,75]. Figure 3.4 provides an illustrative example of the flowchart sequence encompassing pre- and post-processing steps utilized for assessing the peak diastolic intravascular pressure gradient.

In the field of echography, the intravascular pressure differences was measured using blood flow imaging and the Bernoulli equation. These investigations have examined non-stenotic vessels [76] (Figure 3.5), as well as the region between the inlet and *vena contracta* in the presence of stenosis, with a comparison of the results against pressure sensor gold standard values [77] (see Figure 3.6). It is noteworthy that in both studies, the researchers did not estimate post-stenotic pressure loss. Instead, they only calculated the pressure difference along a specific streamline, which represents only the conversion from static to dynamic pressure. The results indicates that if this pressure difference is expressed in mmHg, its value will be less than 1 mmHg.

Olesen *et al.* [13] investigated the estimation of intravascular pressure drop employing the Bernoulli equation for velocity vector field that they acquired using transverse oscillation in ultrafast imaging. Figure 3.7 demonstrates an example of their estimated pressure drop in comparison to values obtained from CFD simulations and catheter measurements in a carotid stenosis phantom.

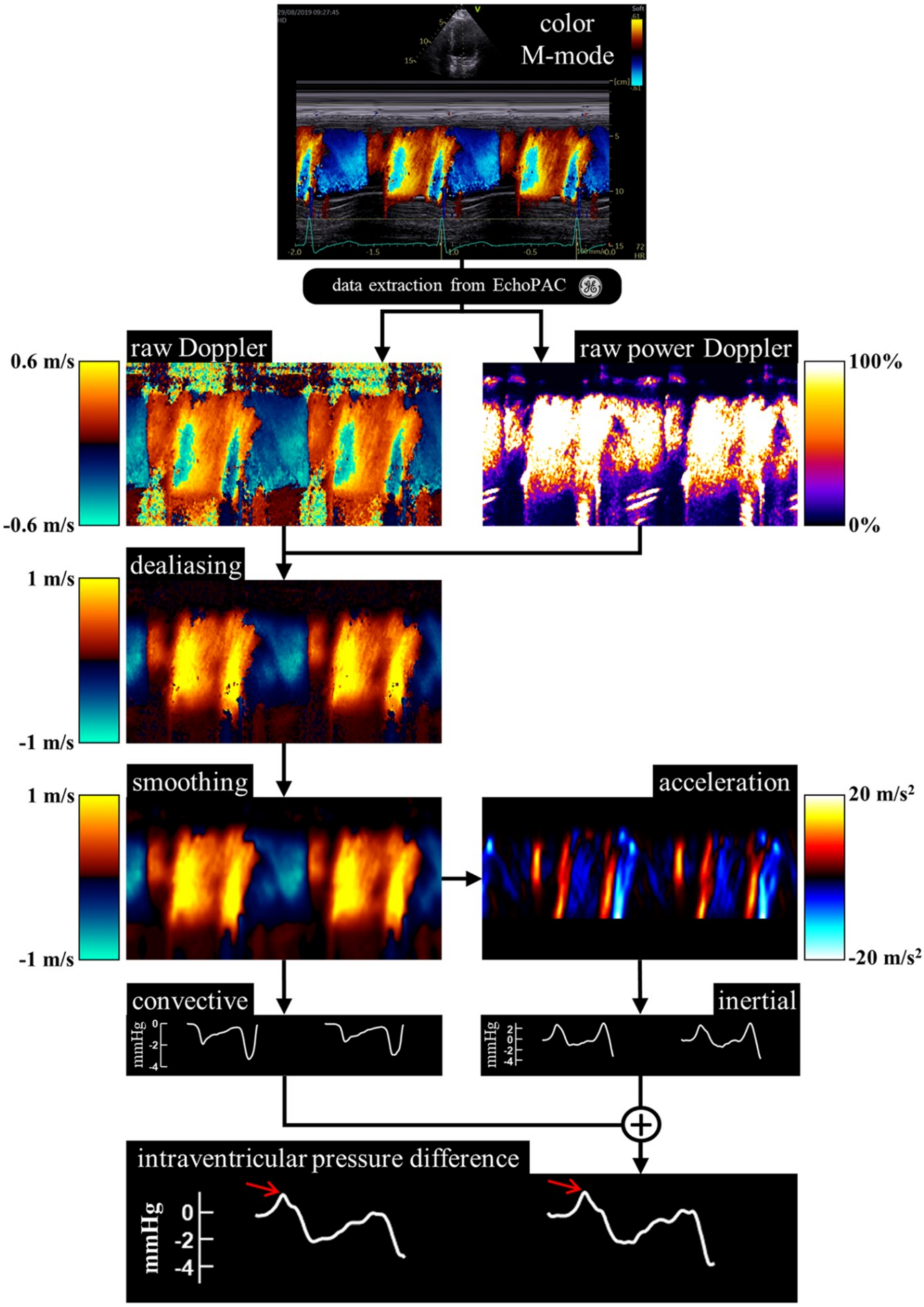

Figure 3.4: Semi-automatic assessment of peak diastolic IVPG using color Doppler M-mode echocardiograms post-processed with custom software (EchoPAC is a software application used in GE Healthcare ultrasound machines for image analysis and reporting) [74].

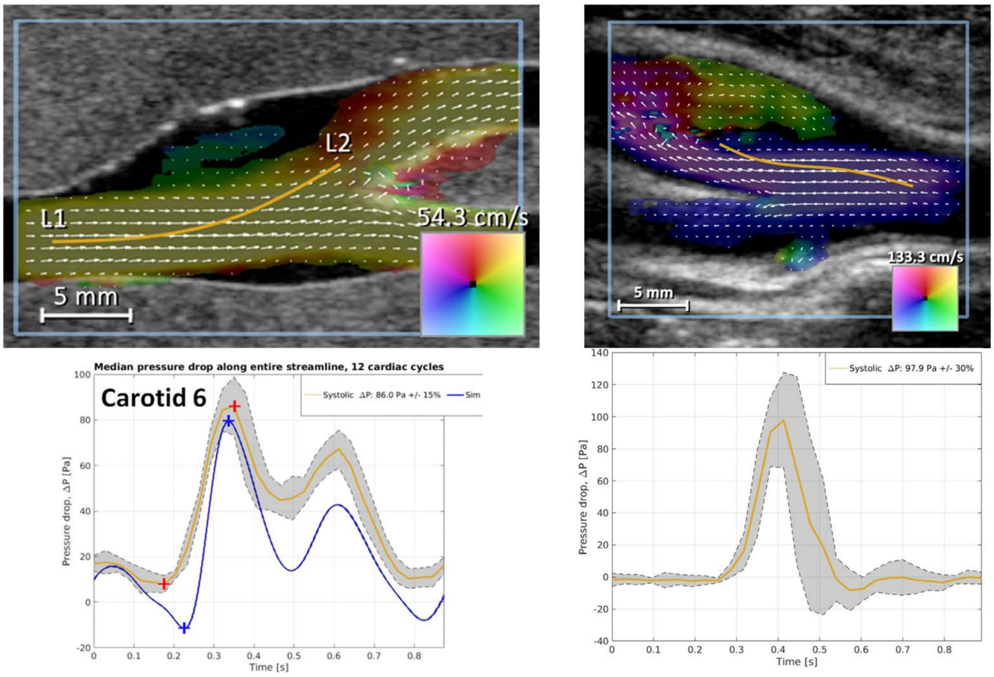

Figure 3.5: (left) VFI of a carotid phantom at peak systole with corresponding median pressure difference (yellow: VFI-based, blue: CFD-based) and standard deviation (gray) along a line connecting the common carotid artery (L1) and carotid bulb (L2). (right) VFI of the carotid bifurcation at peak systole in a healthy volunteer, depicting the measured pressure difference (yellow line) and standard deviation (grayed area) across 11 cardiac cycles [76].

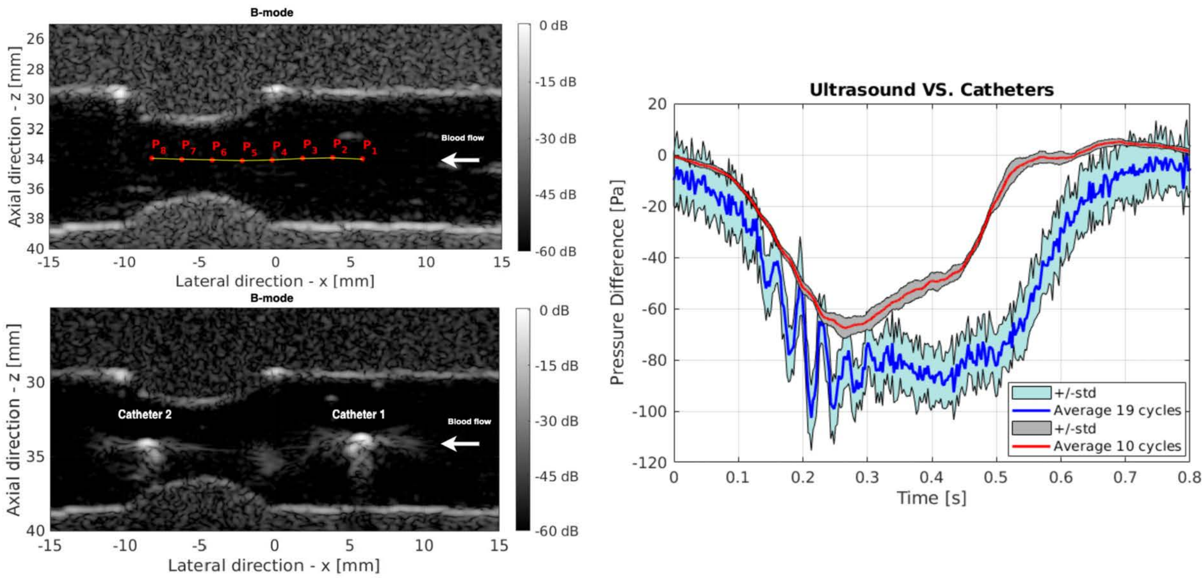

Figure 3.6: (left) Streamline path and catheter positions in the ultrasound method. (right) Comparison between pressure difference measured using invasive catheter method (blue) and ultrasound-based estimated values (red) in a stenotic blood vessel (60% cross-sectional area reduction) [77].

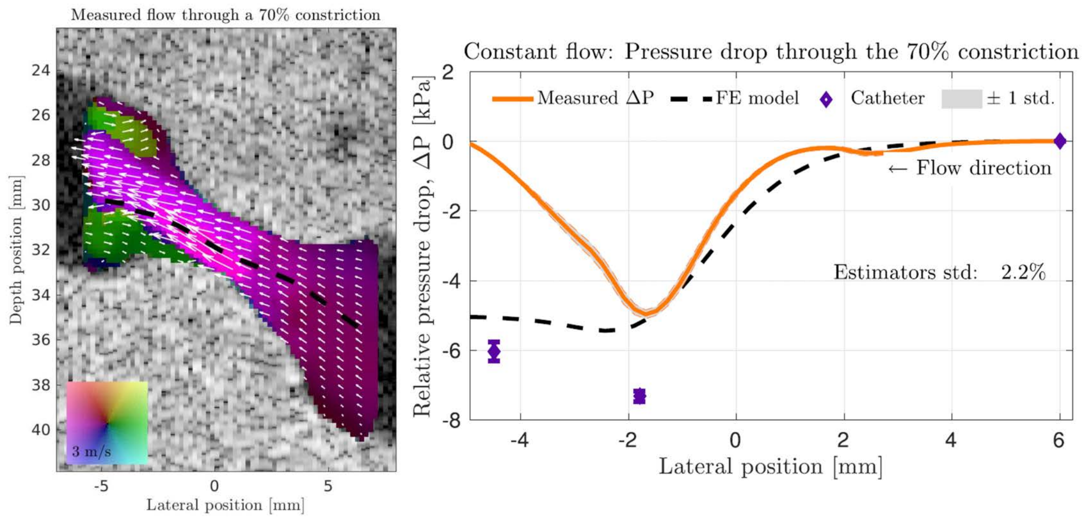

Figure 3.7: (left) Vector velocity ultrasound image over the 70% constriction flow phantoms under steady flow rate. (right) Estimated pressure drop using Bernoulli method along the black-dotted streamline passing through the center of the constriction, compared to measured and simulated pressure drop values [13].

One major limitation of using the mentioned equation is its simplification, which assumes inviscid flow and disregards energy dissipation caused by post-stenotic turbulence resulting from frictional forces. As a result, it solely provides an estimate of the conversion from static to dynamic pressure, representing the change in kinetic energy. In reference to Figure 3.7, which visualizes the research of Olesen *et al.*, the orange plot represents the estimated pressure drop across the stenosis. It is apparent that the Bernoulli equation, used in this context, does not account for the pressure loss, as evidenced by the plot returning to its initial value. Upon comparing the outcomes of finite element (FE) model and catheter measurements, this discrepancy becomes particularly pronounced and show that the traditional Bernoulli equation may be insufficient in estimating pressure loss in the post-stenotic region. While this method may be suitable for severe stenosis cases where the constriction degree is high and it assumes no pressure recovery occurs after the stenosis. Consequently, the problem is simplified to a 1D scenario, considering the maximum pressure drop in the *vena contracta* (refer to Figure 1.5) as the pressure loss.

It is noteworthy that in the PIV imaging method, in a general context, various approaches have been employed for pressure estimation. These include using the Navier-Stokes [78], Poisson [79], and Bernoulli equations [80].

3.4 Energy concept

3.4.1 Energy loss index method

The severity of aortic stenosis is commonly determined by measuring the transvalvular pressure gradient or the effective orifice area (EOA) of the aortic valve [81]. In aortic stenosis, there is an abrupt change in flow geometry, resulting in a loss of fluid energy dissipated as heat (refer to section 1.3), according to the principles of hydraulics. However, these traditional parameters do not account for the extent of pressure recovery that may occur downstream of the stenosis. To address this limitation, a new Doppler echocardiographic parameter based on the concept of energy loss was proposed [81,82]. This parameter aims to adjust the EOA for pressure recovery and is known as the energy loss index (ELI). It was hypothesized that ELI would enhance the assessment of stenosis severity and facilitate risk classification in aortic stenosis. Furthermore, clinical validation of ELI was conducted to confirm its applicability in clinical settings [83]. By employing the principles of fluid mechanics, specifically the Bernoulli equation (Equation (3.5)) and momentum conservation between the left ventricle and the aorta, one can derive the mathematical formulation for quantifying energy loss (E_L) in this context:

$$E_L = 4V_{VC}^2 \left(1 - \frac{\text{EOA}}{A_A}\right)^2 \tag{3.6}$$

where V_{VC} represents the velocity in the stenosis (*vena contracta*), EOA denotes effective orifice area, and A_A refers to aortic cross-sectional area (Figure 3.8).

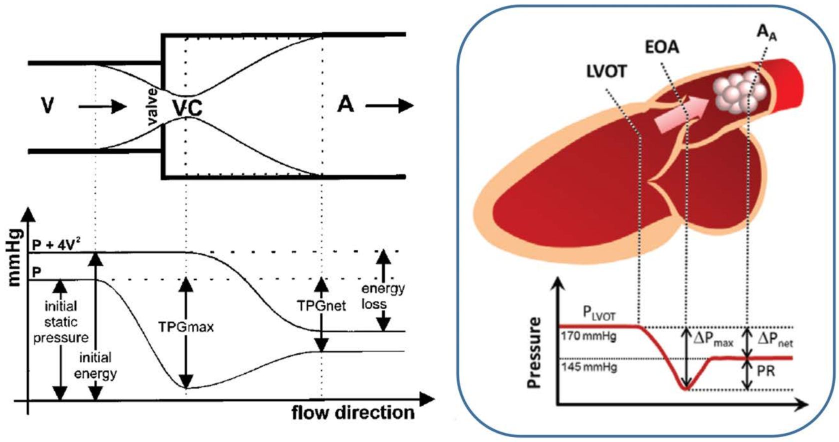

Figure 3.8: (left) Schematic representation of system composed of left ventricle, aortic valve, and ascending aorta, with corresponding static pressure (P) and energy in terms of total pressure (P+4V^2). V indicates left ventricular outflow tact; VC, *vena contracta*; A, aorta and TPG, transvalvular pressure gradients [82]. (right) The phenomenon of pressure recovery in aortic stenosis. Schematic representation of flow and blood pressure across the left ventricular outflow tract (P_{LVOT}), aortic valve, and ascending aorta (A_A) during systole in a patient. EOA represent valve effective orifice area [83].

3.4.2 Work-energy equation

Several researchers have used the work-energy equation for non-invasive estimation of relative pressure differences from PC-MR imaging in the aorta [84, 85]. This equation represents an alternative formulation of the Navier-Stokes equations. The derivation of this fundamental energy relation for an incompressible Newtonian fluid (in the absence of gravity), can be approached in two ways: either by directly formulating the conservation law for energy or by multiplying the Navier-Stokes equations (Equation (3.2)) by velocity field of the fluid (virtual work) and integrating over the entire fluid domain considering its boundary. This yields the classic work-energy equation and provides insight into the actual work and energy held within the fluid at a given time [84, 86]. Figure 3.9 presents an illustrative example of the application of this method to assess pressure differences across varying cross-sectional areas in a coarcted aorta.

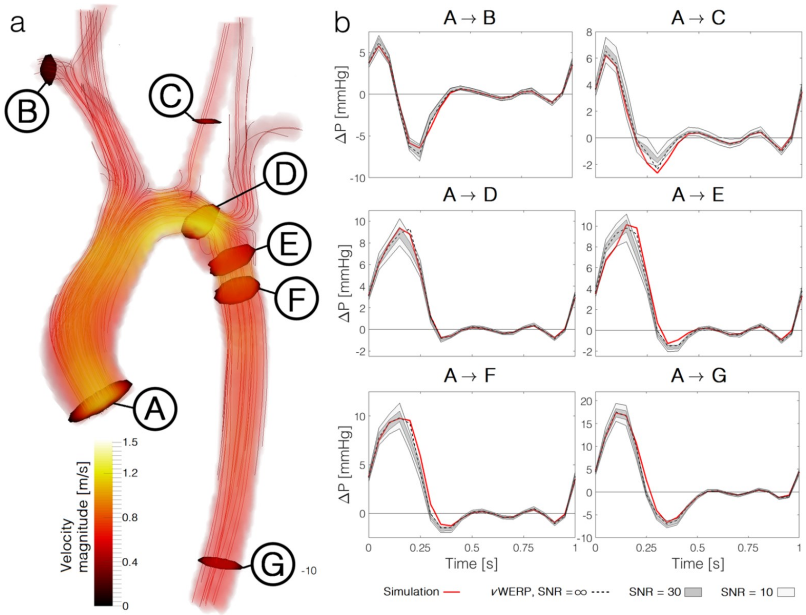

Figure 3.9: Estimated relative pressure differences in a patient-specific coarcted aorta using work-energy method. (a) Visualisation of velocity magnitude with streamlines, along with all selected inlet and outlet planes indicated by A – G. (b) Relative pressure estimations from aortic inlet (A) to all selected outlet planes (B – G) as a function of time. True pressure from simulations is given by the red continuous line, work-energy based given by the dashed black, dark gray, and light gray fields, for SNR = ∞/30/10, respectively [85].

The primary limitation of employing this method is the requirement for precise segmentation of the region of interest, which necessitates high-resolution imaging [84]. Moreover, the numerical calculations involved in implementing this method, including equation solving and force integration, are susceptible to potential numerical errors which have the potential to affect the accuracy of the pressure difference estimation.

To achieve the objective of our study, which involved estimating pressure loss after an arterial stenosis, we initially attempted to use several methods individually that appeared suitable for our case. However, we were unable to obtain accurate estimations of pressure loss with any of them. For instance, when applying the Navier-Stokes equation to the entire stenotic artery model, we encountered numerical issues, particularly in calculating second-order derivatives within the stenosis area. Despite the inherent limitations of the Poisson pressure approach, which requires a well-segmented arterial vessel, we also tried employing it to estimate pressure loss, but accurate results could not be obtained. The Bernoulli equation, commonly used in clinical practice for symptomatic patients with severe stenosis, did not meet our needs for pressure loss estimation. As mentioned earlier, it fails to account for energy dissipation caused by friction forces induced by turbulence after the stenosis. Moreover, our study focused on mild to moderate stenosis cases, which present greater challenges for assessment and early diagnosis. Thus, relying solely on the Bernoulli equation would be insufficient to comprehensively understand the physical process of pressure recovery involved in pressure loss estimation. Therefore, a more precise relative pressure map was required.

Through an extensive literature review, we examined the advantages and limitations of various methods for estimating pressure loss in intravascular stenosis, considering their compatibility with our objectives. Based on this analysis, we arrived at a conclusion: combining the Bernoulli equation (Equation (3.5)) and the Navier-Stokes equations (Equation (3.2)) could provide robust coverage of the physical phenomena occurring in intravascular flow, leading to accurate estimations of trans-stenotic pressure loss. Consequently, we proposed a method that utilizes the Bernoulli equation alone in the initial section of the stenosis, from the inlet to the *vena contracta* (as illustrated in Figure 1.5), where the absence of turbulence results only in static-to dynamic pressure change without energy dissipation. This approach is suitable for estimating the maximum pressure drop occurring at *vena contracta*, where the area is significantly narrowed. Subsequently, in the second section extending from the *vena contracta* to the outlet, the flow undergoes divergence and encounters a sudden change in geometry (as discussed in section 1.3). In this region, energy dissipation occurs due to frictional forces within the fluid induced by its viscosity. Therefore, incorporating the Navier-Stokes equation is appropriate to account for the energy losses associated with these frictional forces.

Chapter 4 will provide a detailed description of our two-fold approach, which includes the developed *v*VFM method for deriving a 2D velocity vector field and our proposed approach for estimating trans-stenotic pressure loss, combining the Bernoulli and Navier-Stokes equations.

4

Vascular Vector Flow Mapping and Pressure loss Estimation

In this chapter, we detail our non-invasive approach for post-stenotic pressure drop measurement using clinical color Doppler imaging. The approach has two main sections: first, we introduce the vascular vector flow mapping (vVFM) technique, which recovers a 2D velocity vector field from scalar Doppler velocity. We then formulate and solve this optimization problem using a least-squares approach based on fluid dynamic constraints. Second, we explain our method for pressure drop measurement, which employs a combination of the Navier-Stokes and Bernoulli equations.

Contents

4.1 2D Vascular vector flow mapping (vVFM)

4.1.1 2D-vVFM optimization problem

The vascular vector flow mapping (vVFM) technique, which aims to derive a 2D intravascular vector velocity field from a scalar color Doppler velocity, was inspired by the recent works of Assi *et al.* [41] and Vixège *et al.* [42] (refer to section 2.2.4). Their intraventricular vector flow mapping (iVFM) technique, based on physics-constrained optimization problems, was developed specifically for clinical applications and utilizes readily available clinical data. The intraventricular velocity vector field can be retrieved by solving the optimization problem for the scalar Doppler velocity in the left ventricle. An example of the validity of their algorithm tested in a patient-specific CFD model of the left heart flow is shown in Figure 4.1.

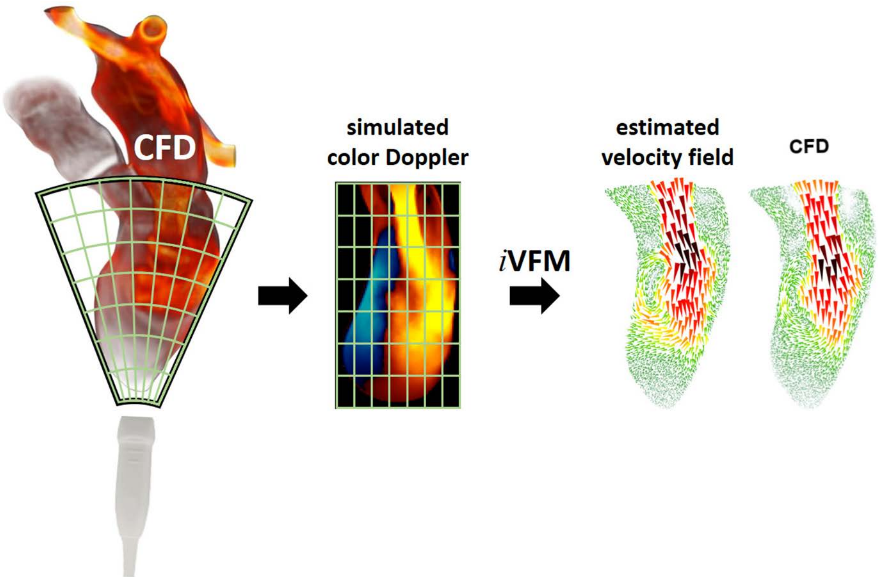

Figure 4.1: From left to right: the physics-constrained iVFM algorithm was tested in a patient-specific CFD model of the left heart flow. Color Doppler fields were simulated from the radial velocity components. The velocity vector fields estimated by iVFM were compared with the ground-truth CFD fields [42].

The main objective of using the vVFM is to recover the 2D velocity vector field $\overrightarrow{v} = \{v_x, v_z\}$ from the scalar Doppler field u_D in a quasi-axisymmetric stenoses. The parameters used in this context include θ_D, the Doppler pulse-echo angle, and ϕ, the angle of the vessel axis to the transducer, both about the z axis. In addition, the distance between the vessel axis and the center of the transducer (d) is an important parameter (as shown in Figure 4.2).

As per convention, the scalar Doppler field u_D is considered positive when the flow is directed towards the transducer. The angles used in this context are defined counter-clockwise, following the trigonometric direction. Considering the Doppler vector direction, $\overrightarrow{d_D}$, we have:

$$\overrightarrow{d_D} = -\sin(\theta_D)\, \overrightarrow{e_x} - \cos(\theta_D)\, \overrightarrow{e_z} \tag{4.1}$$

since

$$\overrightarrow{v} = v_x\, \overrightarrow{e_x} + v_z\, \overrightarrow{e_z} \tag{4.2}$$

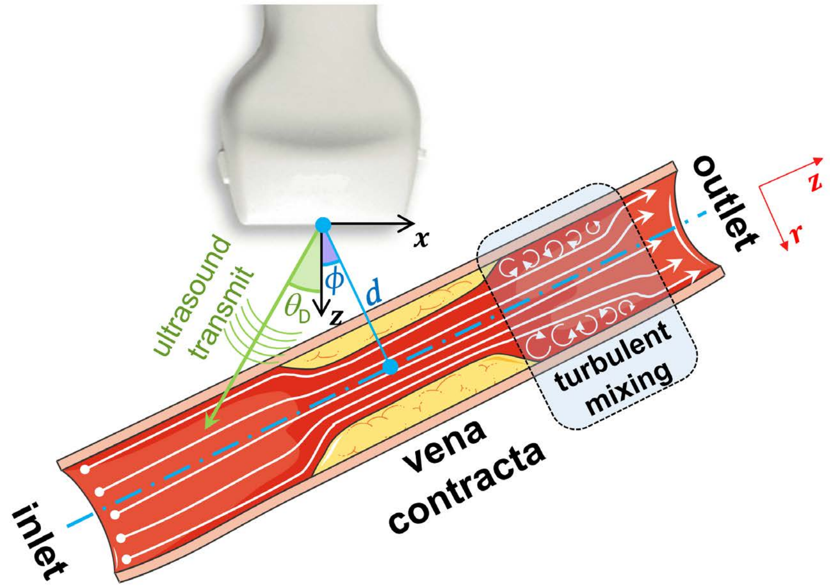

Figure 4.2: Color Doppler ultrasound in quasi-axisymmetric arterial stenosis. θ_D is the Doppler pulse-echo angle, d is the distance between the transducer center and the vessel axis and ϕ is the angle of the vessel axis to the transducer.

the Doppler velocity can be defined as follow:

$$u_D = \overrightarrow{v} \cdot \overrightarrow{d_D} = -\sin(\theta_D)\, v_x - \cos(\theta_D)\, v_z \tag{4.3}$$

therefore the relationship between measured Doppler, u_d, and the true velocity value, $u_{D_{\text{real}}}$, can be expressed as follows:

$$u_D = u_{D_{real}} + \varepsilon = -\sin(\theta_D)\, v_x - \cos(\theta_D)\, v_z + \varepsilon \tag{4.4}$$

where ε represents noise in the measured velocity data.

4.1.2 Continuity equation

The continuity equation, expressed as Equation (4.5) in the absence of sources and sinks, is a fundamental fluid mechanics equation governing the conservation of mass for any fluid flow. In this equation, ρ represents the mass density and $\overrightarrow{v}$ indicates the fluid velocity vector, which are particularly convenient to describe the flow as a set of reference volumes (such as pixels or voxels) where the fluid can enter or exit. By accounting for variations in mass density, the continuity equation provides a way to quantify how the amount of fluid within a given reference volume changes over time and how fluid is exchanged between adjacent volumes:

$$\frac{\partial \rho}{\partial t} + \mathrm{div}(\rho \overrightarrow{v}) = 0. \tag{4.5}$$

We assume that blood is an incompressible fluid, meaning its mass density remains constant within the considered volume and over time. This assumption simplifies the continuity equation for cylindrical coordinate of (z,r) (red color coordinate system in Figure 4.2) as follows:

$$\mathrm{div}(\overrightarrow{v}) = \partial_r v_r + \frac{v_r}{r} + \partial_z v_z = 0. \tag{4.6}$$

To ensure numerical stability in particular in the center of the vessel axis (where $r = 0$), we multiply both sides of the equation by r. As a result, we obtain the following expression:

$$r\,\mathrm{div}(\overrightarrow{v}) = r\,\partial_r v_r + v_r + r\,\partial_z v_z = 0. \tag{4.7}$$

After reformulating 2D-vVFM problem from cylindrical coordinate to a right-handed Cartesian grid associated with a linear transducer (x,z) (black color coordinate system in Figure 4.2), considering the angle ϕ between the transducer and the vessel axis, the equation can be modified to:

$$\begin{aligned}(-x\,\sin\phi + z\,\cos\phi - d)\,\mathrm{div}(\overrightarrow{v}) &= (-x\,\sin\phi + z\,\cos\phi - d)\,\partial_z v_z - v_x\,\sin\phi \\ &+ v_z\,\cos\phi + (-x\,\sin\phi + z\,\cos\phi - d)\partial_x v_x = 0 \text{ on } \Omega\end{aligned} \tag{4.8}$$

where Ω indicates the intravascular region of interest and multiplicative term, $(-x\,\sin\phi + z\,\cos\phi - d)$, represents the distance from the main axis (vessel axis). We used the continuity equation as our first physical constraint to reconstruct the intravascular flow. Since the flow reconstruction is in two dimensions, this relation is verified, allowing us to generate a physically consistent flow.

4.1.3 Free-slip wall boundary condition

The second constraint we used to reconstruct the intravascular flow is a condition on blood flow at the wall, also known as a boundary condition. There are two main wall boundary conditions in fluid mechanics: the slip boundary condition and the no-slip boundary condition at the wall (in our case, the endothelium). The no-slip and no penetration condition are the most commonly used boundary condition in fluid mechanics. First one describes a flow where the fluid adheres to the wall, meaning that the flow velocity at the wall is equal to that of the wall. This condition considers the boundary layer, a thin region where viscosity forces dominate the flow due to the interaction with the wall. The second one, which is the condition that we used, considers the intravascular wall to be a smooth surface to impose this tangential boundary condition, in such a way that, in the normal direction, the blood is bound to the wall, so it cannot penetrate or detach from it. It rises to the following wall condition:

$$\overrightarrow{v} \cdot \overrightarrow{n}|_{\mathrm{wall}} = v_x n_x + v_z n_z = 0 \text{ on } \partial\Omega \tag{4.9}$$

where the unit vector normal to the vessel walls is noted $\overrightarrow{n}|_{\mathrm{wall}} = \{n_x, n_z\}$ and $\partial\Omega$ stands for the boundary of the intravascular region of interest.

4.1.4 Minimization of the problem

As previously discussed, our problem can be expressed as a constrained minimization problem where we search for a minimum cost function subject to certain constraints. In other words, we are only considering solutions that satisfy the constraints, and the chosen solution will be the one that minimizes the cost function. The cost function $J(\overrightarrow{v})$, is based on the consistency between Doppler velocities and the 2D reconstructed velocity field associated with the linear transducer coordinate system (see Equation (4.4)) and includes a smoothing term. Therefore, our problem can be written in the following form:

Minimize

$$J(\overrightarrow{v}) = \int_{\Omega}((u_D + \sin(\theta_D)\, v_x + \cos(\theta_\mathrm{D})\, v_z)^2 + \alpha\, \mathscr{L}(\overrightarrow{v}))\, d\Omega$$

subject to

$$\begin{cases} \mathrm{div}(\overrightarrow{v}) = 0 \text{ on } \Omega \\ \overrightarrow{v} \cdot \overrightarrow{n}|_{\mathrm{wall}} = v_x n_x + v_z n_z = 0 \text{ on } \partial\Omega. \end{cases} \tag{4.10}$$

The term $\mathscr{L}(\overrightarrow{v})$ is a smoothing function that contains second-order partial derivatives of the velocity with respect to x and z. It is tuned by α, a positive scalar heuristically selected, which induces spatial smoothing. By minimizing this cost function, the vector velocity field, $\overrightarrow{v} = \{v_x, v_z\}$, is estimated.

To solve this constrained least-squares problem, the Lagrange multipliers method is used. In this technique the multipliers $\boldsymbol{\lambda_1}$ and $\boldsymbol{\lambda_2}$ become variables in the function, where $\boldsymbol{\lambda_1}$ is a vector of multipliers corresponding to the conservation of mass constraint, and $\boldsymbol{\lambda_2}$ is a vector of multipliers corresponding to the free-slip boundary condition.Considering **v** as the velocity vector field and **n** unit vector normal to the vessel walls, the targeted solution involves solving for (**v**, $\boldsymbol{\lambda_1}$, $\boldsymbol{\lambda_2}$) in the final problem, expressed as follows:

$$J(\mathbf{v}, \boldsymbol{\lambda_1}, \boldsymbol{\lambda_2}) = \int_{\Omega}(u_D + \sin(\theta_D)\, v_x + \cos(\theta_D)\, v_z)^2 + \alpha\, \mathscr{L}(\mathbf{v})\, d\Omega + \boldsymbol{\lambda_1}\mathrm{div}(\mathbf{v}) + \boldsymbol{\lambda_2}\, \mathbf{v}\cdot\mathbf{n}|_{\mathrm{wall}}. \tag{4.11}$$

To determine the minimum of J(**v**, $\boldsymbol{\lambda_1}$, $\boldsymbol{\lambda_2}$), we need to find the values of (**v**, $\boldsymbol{\lambda_1}$, $\boldsymbol{\lambda_2}$) as the problem solutions, such that its derivative is equal to zero. The reconstructed 2D velocity field is contained in the variable **v**. Therefore, only this is considered for the study of intravascular flow.

4.2 Finite-difference discretization of the problem

4.2.1 Introduction to mathematical operators

In this chapter, we distinguish between scalars (0D), vectors (1D) and matrices (2D). To ensure better visibility and understanding, we will denote scalars in lowercase (b), vectors in bold lowercase (**b**) and matrices in bold uppercase (**B**). This distinction will help clarify the differences between these fundamental mathematical objects and their properties.

To solve the constrained least squares problem using the Lagrange multipliers method numerically, we employ a finite-difference discretization scheme. It requires writing the entire problem as a matrix-vector product, so we must first transform the matrix into a vector form through vectorization (so called "vec"), as depicted in Figure 4.3. By doing so, we can effectively represent the problem as a linear algebraic system and use standard numerical methods to solve it. To rewrite the problem in matrix form, we must introduce two mathematical concepts:

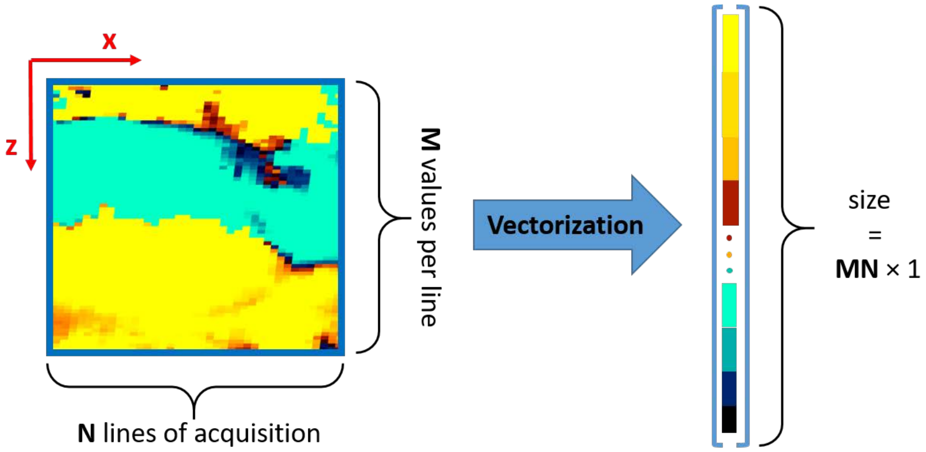

Figure 4.3: Diagram of a matrix containing a Doppler acquisition and its corresponding vector.

the Hadamard and the Kronecker product.

- Firstly, the Hadamard product (also known as the element-wise product) is the product of the corresponding elements in two matrices or tensors. It is denoted by the symbol "$\circ$" and is defined as follows:

$$A \circ B = \begin{bmatrix} a_1 & a_2 \\ a_3 & a_4 \end{bmatrix} \circ \begin{bmatrix} b_1 & b_2 \\ b_3 & b_4 \end{bmatrix} = \begin{bmatrix} a_1 b_1 & a_2 b_2 \\ a_3 b_3 & a_4 b_4 \end{bmatrix}. \tag{4.12}$$

- The second one, the Kronecker product, denoted by $\otimes$, is the multiplication of each term in a matrix A by the matrix B:

$$\begin{aligned} A \otimes B &= \begin{bmatrix} a_1 & a_2 \\ a_3 & a_4 \end{bmatrix} \otimes \begin{bmatrix} b_1 & b_2 \\ b_3 & b_4 \end{bmatrix} = \begin{bmatrix} a_1 \begin{bmatrix} b_1 & b_2 \\ b_3 & b_4 \end{bmatrix} & a_2 \begin{bmatrix} b_1 & b_2 \\ b_3 & b_4 \end{bmatrix} \\ \\ a_3 \begin{bmatrix} b_1 & b_2 \\ b_3 & b_4 \end{bmatrix} & a_4 \begin{bmatrix} b_1 & b_2 \\ b_3 & b_4 \end{bmatrix} \end{bmatrix} \\ A \otimes B &= \begin{bmatrix} a_1 b_1 & a_1 b_2 & a_2 b_1 & a_2 b_2 \\ a_1 b_3 & a_1 b_4 & a_2 b_3 & a_2 b_4 \\ a_3 b_1 & a_3 b_2 & a_4 b_1 & a_4 b_2 \\ a_3 b_3 & a_3 b_4 & a_4 b_3 & a_4 b_4 \end{bmatrix}. \end{aligned} \tag{4.13}$$

4.2.2 Finite-difference discretization of the problem

To recap, our goal is to minimize Equation (4.11). We will expand the equation before converting it into matrix-vector form to achieve this. This matrix-vector form can then be solved numerically to obtain a solution. Before processing, we introduce the different notations we will use throughout this chapter in Table 4.1, including the different forms of each variable (whether it is a matrix, vector, or scalar) and other necessary concepts to understand the equations. In the rest of this chapter, we rewrite the problem as a whole in vector form using these notations. In addition, Figure 4.3 specifies the element sizes used in the calculations.

Table 4.1: Notation for the various variables and other concepts necessary to understand the equations of the 2D-vVFM (inspired from Vixège *et al.* [42]).

Scalar	Column vector Size = $(MN \times 1)$	Matrix Size = $(M \times N)$	Description
u_D	$\mathbf{u_D}$	$\mathbf{U_D}$	Doppler velocities before scan conversion.
x	$\mathbf{x}$	$\mathbf{X}$	x coordinates of grid nodes.
z	$\mathbf{z}$	$\mathbf{Z}$	z coordinates of grid nodes.
v_x	$\mathbf{v_x}$	$\mathbf{V_x}$	Velocity in x direction.
v_z	$\mathbf{v_z}$	$\mathbf{V_z}$	Velocity in z direction.
	$\mathbf{n_x}$	$\mathbf{N_x}$	x component of the unit vector normal to the inner wall of the vessel. It is zero if the node does not belong to the vascular inner wall.
	$\mathbf{n_z}$	$\mathbf{N_z}$	z component of the unit vector normal to the inner wall of the vessel. It is zero if the node does not belong to the vascular inner wall.
	$\boldsymbol{\delta}$	$\boldsymbol{\Delta}$	The region of interest ($\boldsymbol{\Delta} = 1$ in the area inside and on the edge of the vessel and $\boldsymbol{\Delta} = 0$ elsewhere).
h_x			Step size in the x direction. It is constant due to the evenly spaced grid.
h_z			Step size in the z direction. It is constant due to the evenly spaced grid.
	$\mathbf{v}$		$\mathbf{v} = [\mathbf{v_x^T}\ \mathbf{v_z^T}]^\mathbf{T}$ is the column vector of size $(2MN \times 1)$, solution of the constrained problem.
	$\boldsymbol{\lambda}_1$		Lagrange multipliers for the first constraint (zero divergence).
	$\boldsymbol{\lambda}_2$		Lagrange multipliers for the second constraint (slip conditions on the wall).
Scalar	**Vector**	**Matrix**	Other concepts
	$\mathbb{I}_\mathbf{p}$	$\mathbf{I_p}$	$\mathbf{I_p}$ is an identity matrix of size $(p \times p)$. $\mathbb{I}_\mathbf{p}$ is a column vector of ones of size $(p \times 1)$.
	$\mathbb{O}_\mathbf{p}$	$\mathbf{O_p}$	$\mathbf{O_p}$ is an identity matrix of size $(p \times p)$. $\mathbb{O}_\mathbf{p}$ is a column vector of ones of size $(p \times 1)$.
		$\dot{\mathbf{D}}_\mathbf{p}$	1^{st} order derivative operator matrix of size $(p \times p) = \begin{bmatrix} -0.5 & 0.5 & & & & & \\ -0.5 & 0 & 0.5 & & & & \\ & -0.5 & 0 & 0.5 & & & \\ & & & \ddots & & & \\ & & & -0.5 & 0 & 0.5 & \\ & & & & -0.5 & 0 & 0.5 \\ & & & & & -0.5 & 0.5 \end{bmatrix}$
		$\ddot{\mathbf{D}}_\mathbf{p}$	2^{nd} order derivative operator matrix of size $(p \times p) = \begin{bmatrix} -1 & 1 & & & & & \\ 1 & -2 & 1 & & & & \\ & 1 & -2 & 1 & & & \\ & & & \ddots & & & \\ & & & 1 & -2 & 1 & \\ & & & & 1 & -2 & 1 \\ & & & & & 1 & -1 \end{bmatrix}$

<ins>Note</ins>: For matrices **A**, **B**, and **C** of sizes $k \times l$, $l \times m$, and $m \times n$, it is recalled that:

$$\mathrm{vec}(\mathbf{AB}) = (\mathbf{I_m} \otimes \mathbf{A})\mathrm{vec}(\mathbf{B}) = (\mathbf{B^T} \otimes \mathbf{I_k})\mathrm{vec}(\mathbf{A}) \tag{4.14}$$

$$\mathrm{vec}(\mathbf{ABC}) = (\mathbf{C^T} \otimes \mathbf{A})\mathrm{vec}(\mathbf{B}) \tag{4.15}$$

$$\mathrm{vec}(\mathbf{A} \circ \mathbf{B}) = \mathrm{vec}(\mathbf{A}) \circ \mathrm{vec}(\mathbf{B}) \tag{4.16}$$

$$\mathbf{A}^{\circ 2} = \mathbf{A} \circ \mathbf{A} \tag{4.17}$$

Velocity: Using these notations, we can rewrite the velocity vector, as defined in Equation (4.4), in the following form:

$$(u_D + \sin\theta_D\, v_x + \cos\theta_D\, v_z)_\Omega \xrightarrow{\text{matrix form}} \mathbf{\Delta} \circ (\mathbf{U_D} + \sin\theta_D\, \mathbf{V_x} + \cos\theta_D\, \mathbf{V_z}). \tag{4.18}$$

If the matrices are vectorized, we get:

$$\boldsymbol{\delta} \circ (\mathbf{u_D} + \sin\theta_D\, \mathbf{v_x} + \cos\theta_D\, \mathbf{v_z}) = [\sin\theta_D\, \mathrm{diag}(\boldsymbol{\delta}) \quad \cos\theta_D\, \mathrm{diag}(\boldsymbol{\delta})]\mathbf{v} + \mathrm{diag}(\boldsymbol{\delta})\mathbf{u_D} \tag{4.19}$$

we note:

$$Q_0 = [\sin\theta_D\, \mathrm{diag}(\boldsymbol{\delta}) \quad \cos\theta_D\, \mathrm{diag}(\boldsymbol{\delta})] \tag{4.20}$$

where Q_0 has the size of $(MN \times 2MN)$.

Divergence: In this regard, we can rewrite the continuity equation constraint introduced in Equation (4.8) as follows:

$$\begin{aligned} &((-x\sin\phi + z\cos\phi - d)\,\partial_z v_z - v_x\sin\phi + v_z\cos\phi \\ &+ (-x\sin\phi + z\cos\phi - d)\,\partial_x v_x)_\Omega \xrightarrow{\text{matrix form}} \\ &\mathbf{\Delta} \circ \left((-\sin\phi\,\mathbf{X} + \cos\phi\,\mathbf{Z} - d) \circ \left(\frac{1}{h_z}\mathbf{\dot{D}_M}\,\mathbf{V_z}\right) - \sin\phi\,\mathbf{V_x} + \cos\phi\,\mathbf{V_z}\right. \\ &\left. + (-\sin\phi\,\mathbf{X} + \cos\phi\,\mathbf{Z} - d) \circ \left(\frac{1}{h_x}\mathbf{V_x}\,\mathbf{\dot{D}_N^T}\right)\right). \end{aligned} \tag{4.21}$$

Once the matrices are vectorized, we obtain:

$$\begin{aligned} &\frac{1}{h_z}\boldsymbol{\delta} \circ (-\sin\phi\,\mathbf{x} + \cos\phi\,\mathbf{z} - d) \circ \left((\mathbf{I_N} \otimes \mathbf{\dot{D}_M})\,\mathbf{v_z}\right) - \sin\phi\,\boldsymbol{\delta} \circ \mathbf{v_x} + \cos\phi\,\boldsymbol{\delta} \circ \mathbf{v_z} + \\ &\frac{1}{h_x}\boldsymbol{\delta} \circ (-\sin\phi\,\mathbf{x} + \cos\phi\,\mathbf{z} - d) \circ (\mathbf{\dot{D}_N} \otimes \mathbf{I_M})\mathbf{v_x} = Q_1\,\mathbf{v} \end{aligned} \tag{4.22}$$

we note:

$$\begin{aligned} Q_1 = [&\frac{1}{h_x}\mathrm{diag}(\boldsymbol{\delta} \circ (-\sin\phi\,\mathbf{x} + \cos\phi\,\mathbf{z} - d))(\mathbf{\dot{D}_N} \otimes \mathbf{I_M}) - \sin\phi\,\mathrm{diag}(\boldsymbol{\delta}) \\ &\frac{1}{h_z}\mathrm{diag}(\boldsymbol{\delta} \circ (-\sin\phi\,\mathbf{x} + \cos\phi\,\mathbf{z} - d))(\mathbf{I_N} \otimes \mathbf{\dot{D}_M}) + \cos\phi\,\mathrm{diag}(\boldsymbol{\delta})] \end{aligned} \tag{4.23}$$

where Q_1 has the size of $(MN \times 2MN)$.

Boundary condition: If we rewrite the second constraint (Equation (4.9)) in a matrix form and then its vectorized form, we will have:

$$\vec{v} \cdot \vec{n}|_{\text{wall}} \xrightarrow{\text{matrix form}} \mathbf{V_x} \circ \mathbf{N_x} + \mathbf{V_z} \circ \mathbf{N_z} \tag{4.24}$$

$$\mathbf{n_x} \circ \mathbf{v_x} + \mathbf{n_z} \circ \mathbf{v_z} = [\text{diag}(\mathbf{n_x}) \quad \text{diag}(\mathbf{n_z})]\ \mathbf{v} \tag{4.25}$$

we note:

$$Q_2 = [\text{diag}(\mathbf{n_x}) \quad \text{diag}(\mathbf{n_z})] \tag{4.26}$$

where Q_2 is of size $(MN \times 2MN)$.

Smoothing: Finally, the smoothing constraint takes into account, for each component, the square of the second and cross derivatives in the region of interest, which can be written as follows:

$$\mathscr{L}(\mathbf{v}) = \sum_{m \in \{x,z\}} \int_{\Omega} ((\partial_z^2\, v_m)^2 + (\sqrt{2}\partial_{xz}^2\, v_m)^2 + (\partial_x^2\, v_m)^2)\, d\Omega \tag{4.27}$$

upon rewriting the v_z component of this constraint in matrix form, prior to squaring each term individually, we derive the following system of equations:

$$(\partial_z^2\, v_z)_\Omega \xrightarrow{\text{matrix form}} \mathbf{\Delta} \circ \left(\frac{1}{h_z^2}\ddot{\mathbf{D}}_\mathbf{M}\mathbf{V_z}\right) \xrightarrow{\text{vectorization}} \frac{1}{h_z^2}\left(\text{diag}(\boldsymbol{\delta})\left(\mathbf{I_N} \otimes \ddot{\mathbf{D}}_\mathbf{M}\right)\right)\mathbf{v_z} \tag{4.28}$$

$$\sqrt{2}(\partial_{zx}^2\, v_z)_\Omega \xrightarrow{\text{matrix form}} \sqrt{2}\,\mathbf{\Delta} \circ \left(\frac{1}{h_z h_x}\dot{\mathbf{D}}_\mathbf{M}\mathbf{V_z}\,\dot{\mathbf{D}}_\mathbf{N}^\mathbf{T}\right) \xrightarrow{\text{vectorization}} \frac{\sqrt{2}}{h_z h_x}\left(\text{diag}(\boldsymbol{\delta})\left(\dot{\mathbf{D}}_\mathbf{N} \otimes \dot{\mathbf{D}}_\mathbf{M}\right)\right)\mathbf{v_z} \tag{4.29}$$

$$(\partial_x^2\, v_z)_\Omega \xrightarrow{\text{matrix form}} \frac{1}{h_x^2}\mathbf{\Delta} \circ \left(\mathbf{V_z}\ddot{\mathbf{D}}_\mathbf{N}^\mathbf{T}\right) \xrightarrow{\text{vectorization}} \frac{1}{h_x^2}\left(\text{diag}(\boldsymbol{\delta})\left(\ddot{\mathbf{D}}_\mathbf{N} \otimes \mathbf{I_M}\right)\right)\mathbf{v_z} \tag{4.30}$$

correspondingly, for terms including $\mathbf{v_x}$ we follow the same approach. Finally, we have $Q_3\mathbf{v}$ with

$$Q_3 = \begin{bmatrix} \mathbf{I_2} \otimes \frac{1}{h_z^2}\left(\text{diag}(\boldsymbol{\delta})(\mathbf{I_N} \otimes \ddot{\mathbf{D}}_\mathbf{M})\right) \\ \mathbf{I_2} \otimes \frac{\sqrt{2}}{h_z h_x}\left(\text{diag}(\boldsymbol{\delta})(\dot{\mathbf{D}}_\mathbf{N} \otimes \dot{\mathbf{D}}_\mathbf{M})\right) \\ \mathbf{I_2} \otimes \frac{1}{h_x^2}\left(\text{diag}(\boldsymbol{\delta})(\ddot{\mathbf{D}}_\mathbf{N} \otimes \mathbf{I_M})\right) \end{bmatrix} \tag{4.31}$$

where Q_3 is of size $(6MN \times 2MN)$.

Constrained problem: By this method, we can transform the entire constrained problem from Equation (4.10) in a discretized matrix form:

$$
\begin{aligned}
&\text{Minimize} \\
&\qquad (Q_0\mathbf{v}+\mathrm{diag}(\boldsymbol{\delta})\,\mathbf{u_D})^{\mathbf{T}}(Q_0\mathbf{v}+\mathrm{diag}(\boldsymbol{\delta})\,\mathbf{u_D})+\alpha\,\mathbf{v}^{\mathbf{T}}Q_3^{\mathbf{T}}Q_3\mathbf{v} \\
&\text{subject to} \\
&\qquad \begin{cases} Q_1\mathbf{v}=\mathbb{O}_{\mathbf{MN}} \\ Q_2\mathbf{v}=\mathbb{O}_{\mathbf{MN}}. \end{cases}
\end{aligned}
\tag{4.32}
$$

Cost function: After reformulating the cost function defined in Equation (4.11), we can represent it as a matrix-vector product:

$$
\begin{aligned}
J(\mathbf{v},\lambda_{\mathbf{1}},\lambda_2) = &(Q_0\mathbf{v}+\mathrm{diag}(\boldsymbol{\delta})\,\mathbf{u_D})^{\mathbf{T}}(Q_0\mathbf{v}+\mathrm{diag}(\boldsymbol{\delta})\,\mathbf{u_D})+ \\
&\alpha\,\mathbf{v}^{\mathbf{T}}\,Q_3^{\mathbf{T}}\,Q_3\,\mathbf{v}+\lambda_{\mathbf{1}}^{\mathbf{T}}\,Q_1\,\mathbf{v}+\lambda_{\mathbf{2}}^{\mathbf{T}}\,Q_2\,\mathbf{v}.
\end{aligned}
\tag{4.33}
$$

As mentioned earlier, to minimize the cost function and obtain the desired solutions, we set its derivative equal to zero:

$$
\nabla_{\mathbf{v},\lambda_{\mathbf{1}},\lambda_{\mathbf{2}}}\,J(\mathbf{v},\boldsymbol{\lambda}_1\boldsymbol{\lambda}_2)=\mathbb{O}
\tag{4.34}
$$

this yields

$$
\begin{cases}
2\,Q_0^{\mathbf{T}}(Q_0\mathbf{v}+\mathrm{diag}(\boldsymbol{\delta})\,\mathbf{u_D})+2\,\alpha\,Q_3^{\mathbf{T}}\,Q_3\mathbf{v}+Q_1^{\mathbf{T}}\,\boldsymbol{\lambda}_1+Q_2^{\mathbf{T}}\,\boldsymbol{\lambda}_2=\mathbb{O}_{\mathbf{2MN}} \\
Q_1\mathbf{v}=\mathbb{O}_{\mathbf{MN}} \\
Q_2\mathbf{v}=\mathbb{O}_{\mathbf{MN}}.
\end{cases}
\tag{4.35}
$$

By restructuring this set of equations, they can be expressed more concisely as a single matrix-vector product, as shown below:

$$
\begin{bmatrix}
2\,Q_0^{\mathbf{T}}\,Q_0+2\,\alpha\,Q_3^{\mathbf{T}}\,Q_3 & Q_1^{\mathbf{T}} & Q_2^{\mathbf{T}} \\
Q_1 & \mathbf{O_{MN}} & \mathbf{O_{MN}} \\
Q_2 & \mathbf{O_{MN}} & \mathbf{O_{MN}}
\end{bmatrix}
\begin{bmatrix} \mathbf{v} \\ \boldsymbol{\lambda}_1 \\ \boldsymbol{\lambda}_2 \end{bmatrix}
=
\begin{bmatrix} -2\,Q_0{}^{\mathbf{T}}\,\mathrm{diag}(\boldsymbol{\delta})\,\mathbf{u_D} \\ \mathbb{O}_{\mathbf{MN}} \\ \mathbb{O}_{\mathbf{MN}} \end{bmatrix}
=
\begin{bmatrix} -2\,Q_0^{\mathbf{T}}\,\mathbf{u_D} \\ \mathbb{O}_{\mathbf{MN}} \\ \mathbb{O}_{\mathbf{MN}} \end{bmatrix}.
\tag{4.36}
$$

A more compact form can be achieved by further simplifying this last formulation:

$$
\mathbf{A}\,\mathbf{x}=\mathbf{b}.
\tag{4.37}
$$

Here, $\mathbf{A}$ is a sparse, symmetric and rank-deficient matrix with dimensions of $(4MN\times MN)$. To simplify the computations, it is necessary to eliminate its rows and columns that contain only zeros. Figure 4.4 shows this matrix before and after removal of the zero rows and columns. In addition, $\mathbf{b}$ and $\mathbf{x}$ are column vectors of size $(4MN\times 1)$. $\mathbf{b}$ contains our acquired Doppler velocity data inside the intravascular region, and $\mathbf{x}$ is the vector of unknowns, which represents the estimated 2D velocity vector field as well as the two Lagrange multipliers. Here, we are interested in estimated velocity vector field, denoted as $\overrightarrow{v}=\{v_{x-v\mathrm{VFM}},\,v_{z-v\mathrm{VFM}}\}$.

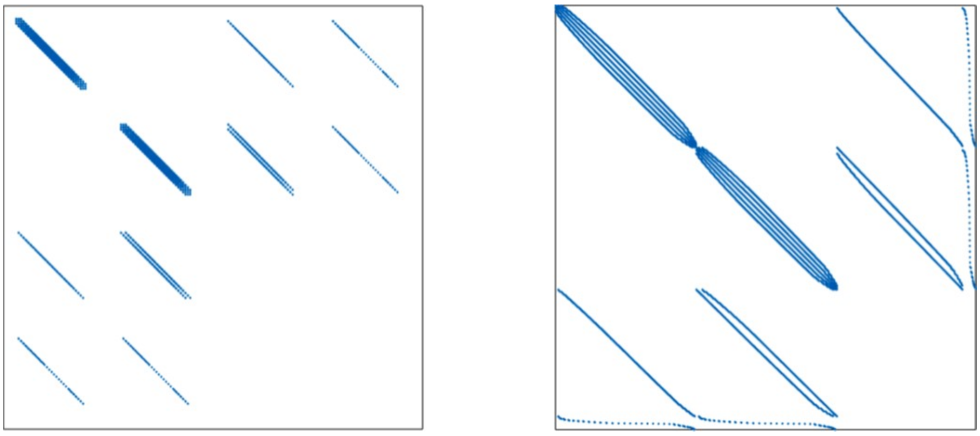

Figure 4.4: Representation of the sparse **A** matrix, before (left) and after (right) removal of the zero rows and columns.

4.3 Pressure drop estimation approach

In Chapter 3, we conducted a comprehensive exploration of diverse methodologies for estimating cardiovascular pressure drops by employing fluid dynamics equations on the acquired cardiovascular velocity data. We also reviewed relevant state-of-the-art studies regarding to this field. Each of these approaches demonstrated unique strengths and limitations, conditional on the particular cardiovascular system region they were designed for, as well as the velocity estimation techniques used across various imaging modalities.

Previously, we mentioned our study's aim is to estimate the pressure loss occurs following an arterial stenosis using clinical Doppler imaging. In pursuit of this objective, we chose to employ some of the introduced fluid dynamics equations to estimate this pressure loss (see Figure 1.5). Notable among these are the Navier-Stokes (Equation (4.39)) and Poisson pressure (Equation (3.3)) equations. However, applying these methods individually posed certain challenges, and we were unable to achieve our desired results. For instance, with Navier-Stokes, we faced numerical difficulties in calculating the second-order derivatives, especially in the stenosis area. To address this, we proposed a compensation method using the Algebraic Turbulence Model, also known as the zero-equation model [87]. In this approach, we added a turbulent viscosity (μ_T) to the fluid's dynamic viscosity, following Prandtl's mixing length theory. The mixing length represents the average distance a turbulent fluid packet and eddy can travel before dissipating. In our case, we modeled it as the minimum between the shortest distance to the walls and a characteristic length. However, it is worth noting that this compensatory method eventually led to a significant overestimation of the pressure loss values. The Poisson equation as was expected did not perform up to our anticipations due to weak detection of the arterial stenosis model's boundary, particularly in setting the boundary conditions and existing numerical challenges during the problem-solving process. Furthermore, the Bernoulli equation (Equation (4.38)) was inappropriate for assessing pressure losses as it ignores the impact of fluid viscosity and the resultant energy dissipation caused by frictional forces within the fluid.

Taking all factors into account, we proposed a method that combines the Bernoulli and Navier-Stokes equations. We divided the geometry into two sections, allowing us to use both equations in estimating the pressure loss ($\Delta P = P_{inlet}-P_{outlet}$) by addressing various physical aspects of flow within the stenotic region. Figure 4.5 illustrates the strategy as follows:

- In the region extending from the inlet to the *vena contracta*, the fluid flow exhibits consistent behavior without energy dissipation (see section 1.3). Consequently, the Bernoulli equation, as recapped in Equation (4.38), can be applied within this region. This allows for the estimation of the conversion between static and dynamic pressure and the identification of maximum pressure drop values. Under ideal conditions, the maximum pressure drop occurs at the midpoint of the stenosis within the *vena contracta*, where the velocity of the divergent flow (jet) reaches its maximum value.

$$P_1 - P_2 = \frac{1}{2}\rho\,(V_2^2 - V_1^2) + \rho \int_1^2 \frac{\partial V}{\partial t}\, dS. \tag{4.38}$$

- In the presence of a constriction, the flow undergoes a convergence towards the *vena contracta*, followed by a subsequent divergence to regain its initial geometry. The majority of energy dissipation occurs within the divergent zone, attributed to frictional forces arising from fluid viscosity. In this scenario, the Navier-Stokes equation proves to be the most appropriate choice, as it accounts for the energy loss resulting from turbulent mixing in the post-stenotic region. For recap, refer to Equation (4.39):

$$\nabla P = -\rho \left(\frac{\partial \overrightarrow{V}}{\partial t} + \overrightarrow{V} \cdot \nabla \overrightarrow{V} \right) + \mu \nabla^2 \overrightarrow{V} + \rho \overrightarrow{g}. \tag{4.39}$$

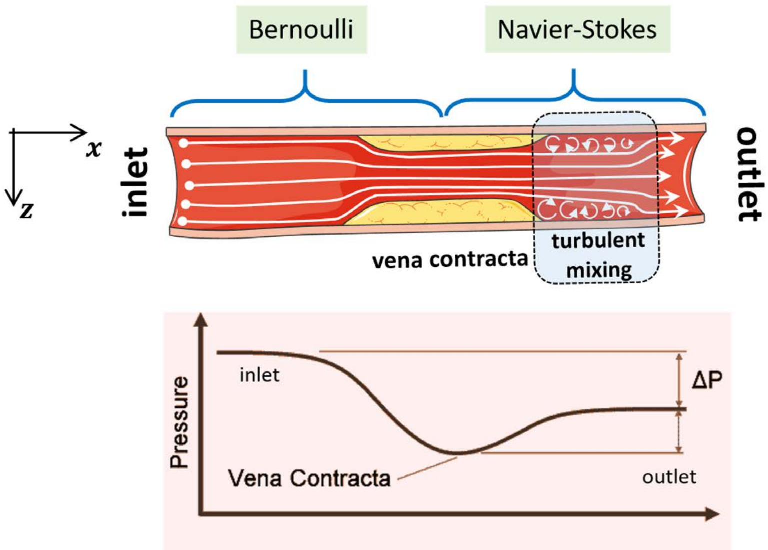

Figure 4.5: An illustration of an arterial stenosis with corresponding sections.

In conclusion, our proposed non-invasive method for estimating post-stenotic pressure loss using conventional color Doppler has two stages: first, we estimate the velocity vector field of the Doppler velocity using 2D-vVFM, and then we estimate the trans-stenotic pressure loss using our combined fluid dynamics equations approach, which is a joining of Bernoulli and Navier-Stokes equations. In the next phase, our proposed non-invasive method will undergo a two-steps validation process. First, *in silico*, using CFD and ultrasound imaging simulations with SIMUS software on carotid stenosis models. Second, *in vitro*, via PIV and color Doppler imaging on carotid stenosis phantoms. The methodology and materials used in each validation step will be detailed in Chapter 5.

5

Method and Materials of Validation Process

This chapter outlines the method and materials used to validate the non-invasive technique involving 2D-vVFM and trans-stenotic pressure drop estimation in various carotid stenosis models. The process involves in silico validation through CFD and ultrasound simulations, and in vitro validation using PIV and color Doppler ultrasound. Details on phantom design, setup configurations, and the challenges and solutions encountered are also discussed.

Contents

The aim of this study is to establish a non-invasive method for measuring trans-stenotic arterial pressure drop using clinical color Doppler imaging. In order to accomplish this objective, our research focused on addressing two optimization problems. The first problem involves estimating the 2D velocity vector field from the scalar velocity obtained through color Doppler imaging, referred to as vVFM (section 4.1). The second optimization problem aims employing a newly proposed fluid dynamics method to estimate the pressure loss based on the obtained two-dimensional velocity data (section 4.3). Both optimization problems were formulated and solved using the MATLAB software. These problems were successfully transformed into linear matrix systems (first optimization) and finite discretization scheme (second problem), allowing for efficient computations that yielded solutions within fractions of a second. After the development of this non-invasive approach, it was necessary to validate it using various methods. We performed the validation process in two ways:

- *In silico*, through CFD and ultrasound imaging simulations (SIMUS).
- *In vitro*, through PIV and color Doppler ultrasound.

This chapter provides a comprehensive overview of the required methods and materials utilized for each step of the validation process. By employing these validation procedures, we aimed to establish the validity and reliability of the non-invasive approach.

5.1 CFD and ultrasound simulations

CFD is popular for fluid dynamics validation due to its cost and time efficiency, as well as its numerical simulation capabilities. It enables researchers to control experimental conditions, and visualize fluid behavior by conducting virtual simulations; therefore, it provides a valuable tool for studying fluid dynamics.

We first simulated blood flow in axisymmetric models of carotid stenoses using the COMSOL Multiphysics (COMSOL, Inc) software. The diameter of the common carotid artery was considered 8 mm, based on physiological values reported in the literature [13,47]. Two stenosis shapes, Cosine and Gaussian, with two degrees of stenosis (60% and 70% diameter reduction) were created to reflect moderate and severe stenoses. Three steady flow rates of 0.3, 0.6, and 1 $\mathrm{L \cdot min^{-1}}$ were studied for each configuration. Blood was assumed as a Newtonian fluid, and turbulent flow conditions were simulated using the $k-\varepsilon$ turbulence model [87], a widely used two-equation model for fluid dynamics simulations of mean flow characteristics. This model describes turbulence through two transported variables: the turbulent kinetic energy (k) and the dissipation rate of turbulent kinetic energy (ε). We conducted simulations to calculate each model's 2D velocity vector fields and trans-stenotic pressure drops, which were used as the ground-truth data.

Following CFD simulations, we seeded the 2D velocity fields with approximately 50,000 pseudo-randomly distributed point scatterers. Subsequently, we performed color Doppler simulations using SIMUS, an open-source ultrasound imaging simulator [88,89] that is part of the MATLAB UltraSound Toolbox (MUST) [90]. The SIMUS software operates based on the principle of linear acoustic equations with a constant propagation velocity, assuming that there is no exchange of signals between echoes from each scatterer. It simulates acoustic pressure fields and radiofrequency (RF) signals by considering the transmission of an ultrasound wave and the received echoes, using uniform linear or convex probes. The utilized properties included a 128-element 7.6-MHz linear array, focused transmits with sliding sub-apertures of 16 elements, a beam-to-flow angle of 15°, and a Doppler packet size of 6. The simulated ultrasound signals were post-processed (demodulation, beamforming, auto-correlation) using the MUST toolbox to obtain Doppler velocities on a Cartesian grid.

5.2 Particle image velocimetry (PIV) experiment

In section 2.3, we provided a comprehensive explanation of the PIV method, its underlying principles, and its application. This method is an advanced non-intrusive optical imaging technique employed to accurately measure and visualize the velocity field of a fluid flow. This method offers high spatial and temporal resolution, enabling precise characterization of flow patterns. Due to its numerous advantages, PIV has become a benchmarking tool in the field of fluid mechanics in validating various parameters, including velocity and pressure, by providing reliable and accurate data. Consequently, in our study, we employed PIV experiments as an essential part of our validation process.

In order to conduct PIV experiments, it was necessary to develop a phantom model that is compatible with this imaging technique, along with the implementation of a well-designed experimental set-up. In the upcoming sections, we will provide a comprehensive explanation of each component, outlining their specific characteristics and roles within our experimental framework.

5.2.1 PIV phantom fabrication

One of the crucial aspects of an *in vitro* experiment is the fabrication of a phantom. A well-constructed phantom is essential for conducting the experiment effectively and obtaining reliable and accurate results. When creating a PIV phantom, two critical criteria must be met. Firstly, the phantom should be completely transparent, ensuring that there are no bubbles present within its walls. This is necessary to prevent any interference with particle detection and accurate estimation of the velocity field. Secondly, the material used for the phantom should possess adequate consistency and rigidity to withstand deformation caused by the passage of fluid at high flow rates. This is crucial to maintain the integrity of the phantom structure and ensure accurate measurements during the experiment.

Several experimental studies have focused on fabricating phantoms specifically designed for optic modality purposes such as PIV. These studies have employed various methods and materials to create these phantoms. The predominant fabrication technique utilized in the literature is the "lost-core casting technique" to make a wall-less phantom. This method involves the following steps:

- *Core preparation*: A core is created using materials with low melting points, typically a low melting point metal (LMPM) such as Carrolow 117 alloy [91] or water-soluble plaster [92, 93]. These core materials can be easily washed away with water.

- *Core fixation*: The prepared core is then positioned and secured within a casting box.

- *Transparent material pouring*: The desired transparent material for the phantom is poured into the casting box, encapsulating the core.

- *Curing*: The poured material is allowed to cure or solidify, forming a solid structure.

- *Core removal*: To create a phantom box without walls, the fabricated structure is immersed in a water bath in a specific temperature. The heat causes the core material to melt away, leaving behind a coreless and wall-less phantom box.

Smith *et al.* [94] are considered pioneers in this method, and their technique has been widely referenced by subsequent studies [95]. In addition to the lost-core casting technique, there are alternative methods available for casting phantoms that involve creating a wall using a mold, allowing for adjustable wall thickness for precise customization [51, 91]. Figure 5.1 illustrates examples of both phantom models.

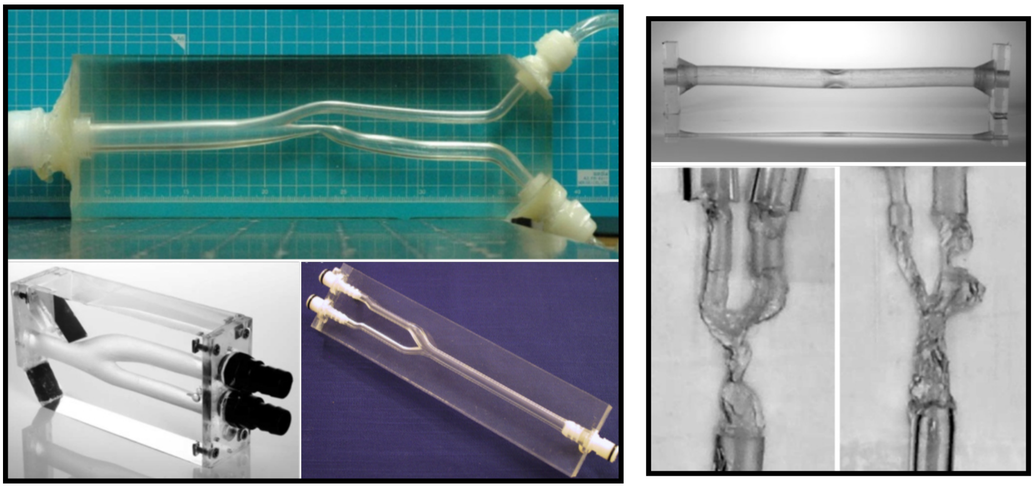

Figure 5.1: (left) Examples of wall-less phantom fabricated using the lost-core casting box technique [51, 93, 95]. (right) Samples of phantoms with walls [51, 53, 92] for optical modality purposes.

One of the primary limitations of the lost-core casting technique lies in the incomplete removal of core material residues when washing the core with water [95]. This can result in undesired remnants of the material being present on the inner surface of the phantom, leading to disruptions in the flow pattern and alterations in the intended experimental conditions. Additionally, when using cores created through 3D printing, their surfaces lack the necessary smoothness [92]. Consequently, these surface patterns persist on the inner surface of the phantom, reducing its transparency, particularly for the purpose of PIV imaging. Furthermore, if disposable cores are employed, each time a phantom is required, a new core must be produced, which can be time-consuming, costly, and dependent on scheduling and facility accessibility. To address these limitations, we have developed an innovative approach to fabricating phantoms, which will be discussed in detail in the following sections.

5.2.1.1 Designing core of phantom

For this study, we initiated with a simplified model of a common carotid artery, representing it as an axisymmetric cylindrical tube with a concentric stenosis located along its length. As previously mentioned, to overcome the limitations associated with existing methods for fabricating phantoms used in PIV experiments, we designed an aluminum core, which eliminated the need for core melting during the fabrication of each new phantom. This design allowed for the separation of the core at the stenosis level, comprising two distinct pieces that could be extracted from both ends of the phantom. Aluminum was chosen as the core material due to its durability, stability, and sufficiently smooth surface for optimal PIV optical imaging purposes.

In accordance with physiological dimensions reported in the literature for the common carotid artery [13, 47] the diameter of the phantom was set to 8 mm. This diameter value aligns with the typical diameter observed in the common carotid artery of adults aged 60 to 70 [94]. To incorporate different stenosis geometries, we selected two shapes: Cosine and Gaussian. In terms of the degree of occlusion, our cores were designed to simulate stenosis with 50% and 60% diameter reduction, representing mild to moderate stenoses as per the criteria established by the North American symptomatic carotid endarterectomy trial (NASCET) [96]. We deliberately refrained from selecting a higher value for the severity of the stenosis due to two reasons. First, as mentioned earlier (section 1.3), the purpose of our study is to estimate the pressure drop in mild to moderate arterial stenosis for earlier diagnosis. Second, even for the purpose of extending the experiment to higher stenoses, the diameter value of 8 mm posed limitations when using a pressure wire to measure the stenosis or downstream pressure within the phantom. The pressure wire, with a diameter of 0.36 mm as specified in its instruction for use notebook, would significantly obstruct the main portion of the stenosis diameter. Such obstruction could disrupt the flow dynamics and substantially alter the experimental results. To maintain experimental integrity and avoid these complications, we determined that the chosen stenosis degree values were appropriate and aligned with the objective of the study.

To ensure that the velocity profile within the phantom could fully develop and that the pressure could be adequately recovered after passing through the stenotic area, we determined the inlet and outlet lengths of the core to be 14 and 16 times the diameter respectively (14D and 16D). This configuration allowed for a sufficiently long inlet section that promotes the complete development of the velocity profile, as well as an outlet section that enables full pressure recovery. We also conducted a comprehensive literature review to determine an appropriate length for the stenosis in our phantoms. The findings from various studies indicate that the length of the lesion has a minimal impact on pressure drop in stenotic vessels, in comparison to the diameter of the stenosis [97], and that the shape of the stenosis, particularly its eccentricity, has a more significant influence [98]. Additionally, Freidoonimehr *et al.* [99] reported that based on clinical data, plaque lengths in the coronary arterial system typically range from 1D to 3D. Taking these factors into consideration, we decided to select a stenosis length of twice the diameter (2D). This choice aligns with the observed plaque lengths in clinical settings and provides a manageable length for catheter measurements in the *vena contracta*. In the Gaussian-shaped model, we considered the length of the stenosis to be equal to three times the standard deviation of the Gaussian shape.

Following the determination of the required dimensions for the cores, we utilized SolidWorks 2021 (Dassault systemes SolidWorks corporation, Waltham, MA, USA) for their design. The construction of the cores was carried out by the "MECA3D innovation technical centre" at INSA-Lyon using computer numerical control (CNC) machining technique, which involves using computer-controlled machines to precisely cut, shape, and finish parts based on the design specifications provided in digital files. The resulting structured phantom cores are depicted in Figure 5.2, illustrating the outcome of the fabrication process.

5.2.1.2 Phantom fabrication process

Material: In the fabrication process of phantoms, researchers have employed various transparent materials, including resin [94], polydimethylsiloxane (PDMS) [47, 50], and even plexiglas in few studies [46]. Previous studies predominantly utilized transparent resin, which belongs to a class of solid or semi-solid compounds. Resins are chemically synthesized from petrochemicals or other raw materials and are renowned for their ability to harden into durable

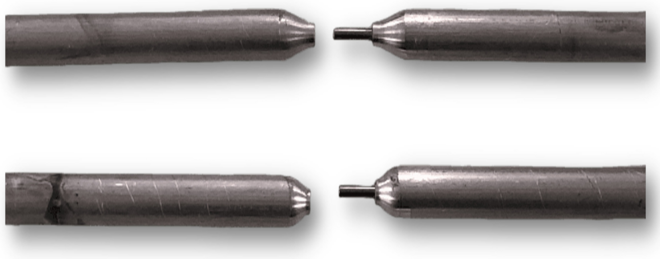

Figure 5.2: Two samples of aluminium cores fabricated using the CNC machining technique. The top sample displays a Cosine-shaped 50% stenosis, while the bottom sample features a Gaussian-shaped 60% stenosis. Each core consists of two distinct parts that can be separated from each other.

and often transparent materials upon curing. However, in more recent phantom fabrication studies, there has been a shift towards the use of PDMS, specifically the Sylgard-184 type from Dow Corning Company (Dow Corning Corp., Midland, MI, USA). PDMS is a silicone-based polymer with its own unique properties. It exhibits high transparency, ensuring clear visualization in experimental setups. In addition to its non-toxicity during preparation and application, it also offers exceptional durability and thermal stability, making it suitable for a range of applications in the field of phantoms. Based on a comprehensive analysis of its properties and a thorough review of relevant literature, we have arrived at the decision to employ PDMS as the material for the PIV phantom.

Mold construction: To facilitate the creation of phantoms with well-defined walls, it was necessary to develop a suitable mold. To accomplish this, a four-piece mold was designed using SolidWorks 2021, ensuring that the main individual components could be easily separated along the midline. Subsequently, the mold was fabricated using a 3D printer available at the multimodal imaging platform of LyonTech (PILoT, Lyon, France). The wall thickness of the phantoms was established at 2mm in order to maintain consistency in the phantom's wall structure. Additionally, this thickness was chosen to ensure sufficient transparency, enabling the visualization of particles passing through the phantom during PIV imaging. Figure 5.3 illustrates an example of the constructed mold in 3D printer.

Preparation process: To prepare the PDMS for phantom fabrication, two primary ingredients were required: a base and a curing agent. The stiffness and flexibility of the final material could be adjusted by varying the amount of curing agent used. A higher concentration of curing agent yields a stiffer material [100]. However, the standard mixing ratio specified in the user manual of the purchased product is 10 parts base to 1 part curing agent. The preparation process involved several steps. Initially, the standard quantities of base and curing agent were thoroughly mixed, followed by gentle manual stirring for a duration of 10 minutes. Subsequently, the mixture was placed in a vacuum chamber to eliminate any formed bubbles.

To ensure a smooth outer surface and maintain transparency in the resulting phantom, strips of electrical duct tape were adhered to the inner surfaces of the 3D-printed mold pieces. To prevent material leakage from the separated pieces, we employed mold dough as a sealing agent. Due to the delicate thickness of the wall, the PDMS material was poured into the mold with precision. To minimize bubble formation, the material was poured in a step-by-step manner, with each step followed by 15 minutes of vacuum chamber treatment. The mold was placed in vacuum chamber for the duration of 45 minutes after the final step. The manipulation time for

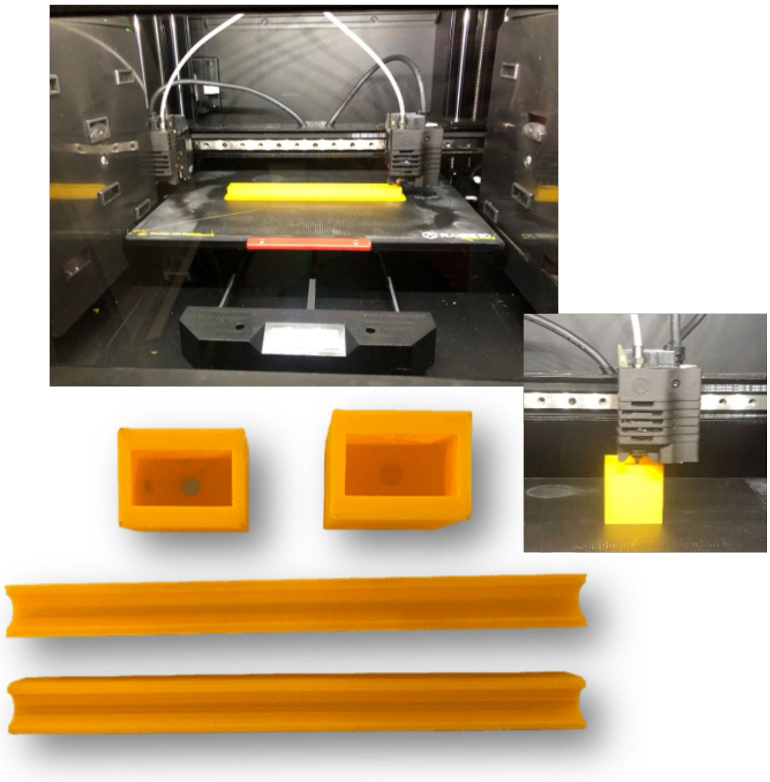

Figure 5.3: 3D-printed mold pieces for PIV phantom fabrication.

the PDMS material was approximately 2 hours. Once the entire PDMS material was poured into the mold, the upper piece of the mold was employed to align and secure the core in the center. The curing time of PDMS is influenced by temperature, with higher temperatures leading to shorter curing times. In light of our available facilities, where an oven was not accessible, we allowed the material to cure at room temperature for a period of 2 days. After 2 days, the product exhibited optimal dryness, enabling the subsequent step of carefully opening the mold and extracting the core pieces from each side. This procedure presents inherent challenges due to the vacuum that forms within the phantom. However, employing delicate handling and patience, we successfully extracted the core pieces from the phantom. Figure 5.4 illustrates the sequential preparation process involved in fabricating the final sample PIV phantom.

5.2.1.3 Alternative materials to PDMS

Having a single setup for both PIV and color Doppler ultrasound experiments offers several advantages. Firstly, conducting both experiments simultaneously saves a significant amount of time and energy and minimizes changes to the experimental properties. Moreover, maintaining consistent conditions such as flow rate enhances the precision and reliability of the results. To explore the possibility of using PDMS in color Doppler ultrasound imaging, we conducted a literature review to find out if the acoustic properties of this material had been previously measured. Avigo *et al.* [101], reported that the speed of sound in PDMS is approximately 12% lower than that in water and soft tissue, where the speed of sound is typically 1540 $\mathrm{m \cdot s^{-1}}$. Furthermore, other studies have noted that resin-based materials and silicone exhibit unusual speed of sound and/or acoustic attenuation [102]. Consequently, we decided to measure the speed of sound in PDMS ourselves. For this purpose, we constructed a cube from it (74 × 45 ×

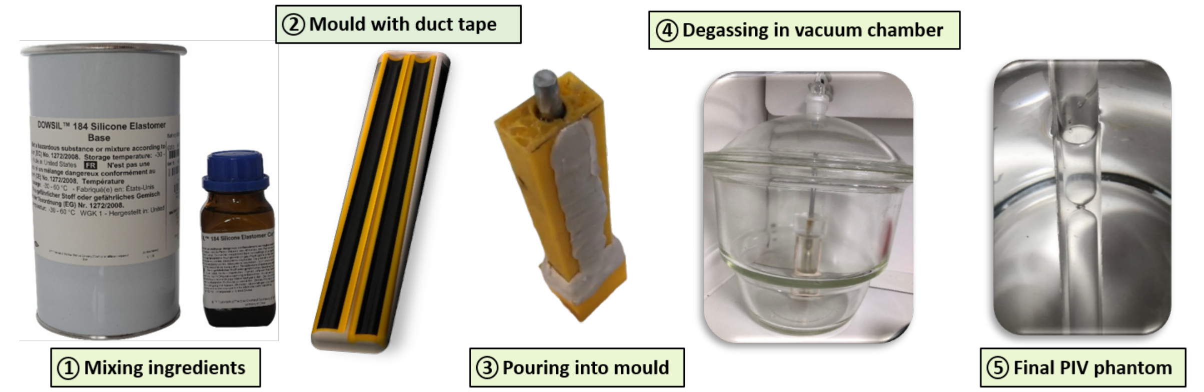

Figure 5.4: Illustration of the PDMS components, left to right: base and curing agent (1), the mold pieces with electrical duct tape applied (2), the mold with sealing dough (3), bubble removal process (4), and the resulting sample PIV phantom (5).

19 mm) and used an ultrasound probe as a source and as well as a hydrophone as a detector for the measurement (see Figure 5.5). After performing the necessary calculations, we determined the speed of sound within the PDMS cube 1127 $m \cdot s^{-1}$, which is 27% lower than that of water and tissue samples. Due to the observed lower speed of sound in PDMS compared to water and

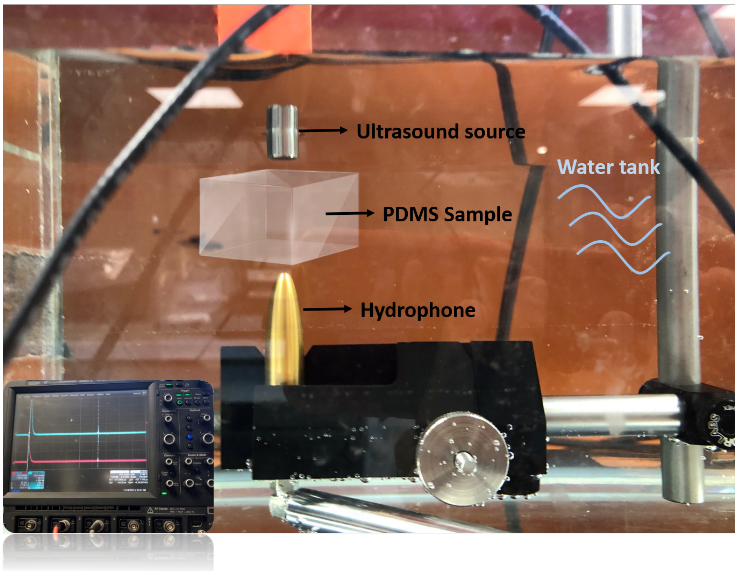

Figure 5.5: Measuring speed of sound in a cubic sample of PDMS material, using an ultrasound probe and hydrophone in a water tank.

body tissue, we decided to explore alternative transparent materials that are compatible with both imaging modalities. Our search in the literature yielded several potential options, which are summarized as follows:

Polyvinyl chloride plastisol (PVCP): PVCP is widely employed in the fabrication of phantoms for various multimodal imaging techniques such as ultrasound, CT, and MRI [103], with particular relevance in the field of photoacoustic imaging. This material exhibits optical transparency and possesses density and acoustic parameters comparable to that of water. Literature reports suggest that the speed of sound in this material is approximately 1400 $m \cdot s^{-1}$, representing a decrease of around 15% compared to the average value observed in soft tissue. However, the acoustic properties of PVCP can be modified by incorporating plastic hardeners and softeners, enabling control over sound speed and elasticity [104]. We attempted to fabricate a phantom using this material; however, certain challenges were encountered. Initially, PVCP did not demonstrate the desired level of rigidity and consistency essential for constructing a cylindrical phantom with a thin wall. In fact, even a minor touch caused it to tear apart. The curing process required heat, but the material solidified rapidly upon cooling, trapping bubbles within. Consequently, we determined that PVCP was not suitable for our intended purpose. Figure 5.6 illustrates the sample phantom created using this material.

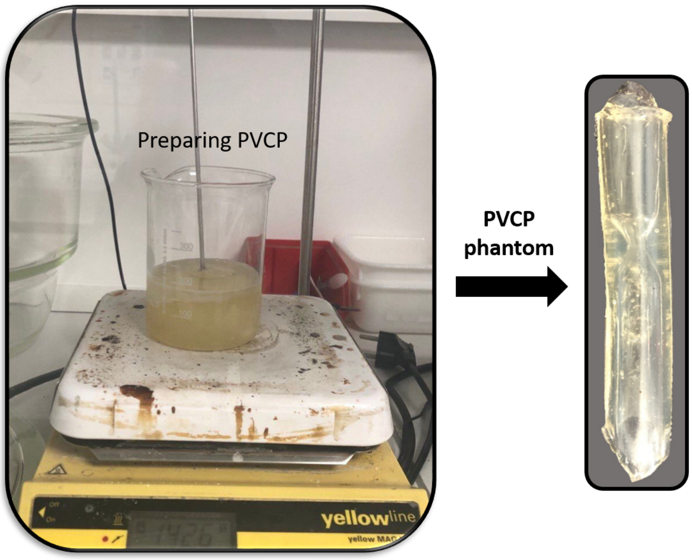

Figure 5.6: Creating a transparent phantom using PVCP material.

Polyvinyl alcohol hydrogel (PVA): PVA is widely utilized in ultrasound imaging applications due to its effective transmission of ultrasound waves and its ability to mimic the acoustic properties of human tissue [105]. It is commonly mixed with water to form a gel-like solution that imitates soft tissue characteristics. The fabrication of this hydrogel involves subjecting the mixture to freezing and thawing processes, which can result in varying properties depending on the number of cycles employed [106]. Initially, the PVA-water mixture is transparent, but as it undergoes multiple freezing and thawing cycles, it transitions to an opaque or white appearance. Consequently, these phantoms cannot be employed for applications where internal visualization or optical imaging is required.

In response to the challenge of developing a transparent PVA hydrogel that is suitable for ultrasound imaging and possesses optical transparency, several researchers have conducted studies in this area. Notably, Hyon *et al.* [107] have emerged as pioneers in this field, and their research has been extensively cited in subsequent studies [108, 109]. Hyon's method involves incorporating dimethyl sulfoxide (DMSO) as a solvent alongside water to prepare a transparent PVA hydrogel. It is important to note that DMSO is an irritating material, and precautions such as working under a flue hood should be taken when handling it. In his approach, he created a homogeneous PVA solution with a concentration of 15%wt, maintaining a water to DMSO mixing ratio of 20/80 by weight as the liquid component. The solution was heated at 140°C for 2 hours. Subsequently, the temperature was reduced to 60°C, and the solution was cast into a mold of choice. It was then placed in a freezer at -20°C for 10 hours to facilitate PVA crystallization. The frozen gel was subsequently exposed to flowing water for 4 days to replace the DMSO within the gel with water. Hyon also reported that the yield stress of the transparent

PVA hydrogel obtained using this formula is significantly higher than that of the translucent one prepared using water alone.

Taking inspiration from Hyon's work, we successfully fabricated a transparent PVA hydrogel sample cube of the same size as the PDMS sample cube. This served as a preliminary example before proceeding to create a stenotic common carotid phantom, with the objective of measuring the speed of sound within it. To conduct this measurement, a single-element ultrasound probe was utilized, as depicted in Figure 5.7. The obtained speed of sound value within the sample was found to be 1686 $m \cdot s^{-1}$, exhibiting consistency and agreement with other relevant studies. For instance, Hasuro *et al.* [110] recently achieved a similar value of

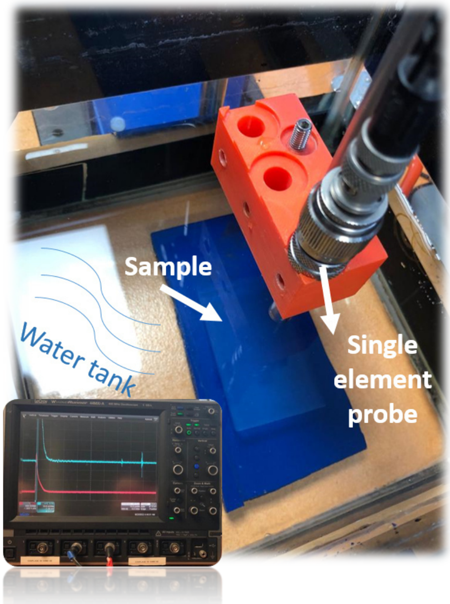

Figure 5.7: Measuring speed of sound in a cubic sample of transparent PVA material, using a single element ultrasound probe in a water tank.

approximately 1792 $m \cdot s^{-1}$. Additionally, the findings of Funamoto *et al.* [111] reported a speed of sound of 1567$\pm$4 $m \cdot s^{-1}$, which aligns closely with our observations. Upon confirming its compatibility with ultrasound imaging and sufficient transparency for PIV imaging, we proceeded to fabricate a stenotic phantom. However, the phantom did not meet the required criteria for our experiments, posing several challenges. Firstly, it exhibited inadequate rigidity and consistency, leading to easy inflation even with low flow rates passing through it. This compromised the stability and accuracy of our experimental setup. Furthermore, the material's high viscosity and rapid solidification posed difficulties in eliminating small bubbles. Despite using a vacuum chamber to degas the material, the bubbles remained trapped within it. In an attempt to mitigate this issue, we allowed the poured material to rest at room temperature for 4 hours before initiating the freezing process. The intention was to provide sufficient time for any bubbles to rise to the surface. However, due to the thin wall thickness of the phantom and the small size of the mold, the bubbles were unable to escape and became trapped within the material. Figure 5.8 showcases an example of the stenotic phantom fabricated using transparent PVA, illustrating the challenges encountered during the process.

Following the fabrication of carotid stenosis phantoms using various materials in our pursuit of a suitable dual-modality imaging medium (ultrasound and PIV imaging), none of the materials met the required criteria for our experiments. Consequently, considering the lower speed

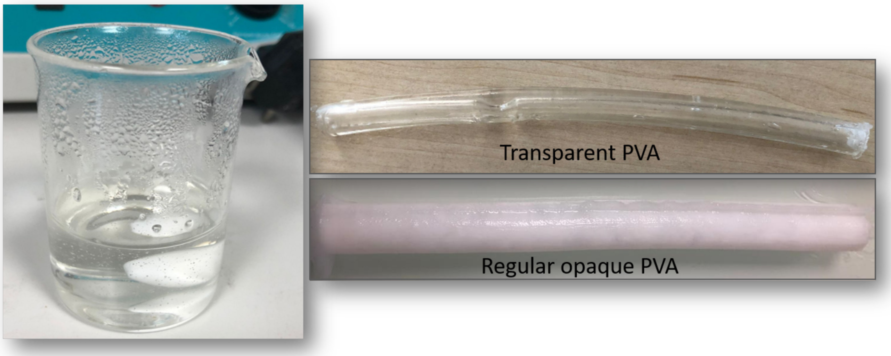

Figure 5.8: (left) Transparent PVA hydrogel prepared for casting into the mold. (right) Fabricated phantoms using PVA hydrogel, with the top phantom representing the transparent PVA and the bottom one showing a regular opaque one.

of sound in PDMS compared to water and body tissue, we decided to conduct both imaging techniques within the same experimental setup. Transparent phantoms constructed with PDMS were utilized for this purpose. This approach allowed us to obtain the required PIV images while simultaneously investigating the feasibility of acquiring color Doppler images from the same phantoms. Unfortunately, we faced challenges in obtaining accurate color Doppler images, especially in the stenosis section. These challenges were primarily caused by the deviation and refraction of sound waves due to the difference in sound speed between the mediums (reservoir water, PDMS, and water inside the phantom). An example of one of the acquired color Doppler images will be presented in Chapter 6 of the manuscript. Consequently, the next section will introduce the experimental setup utilized for these experiments.

5.2.2 Dual modality experimental setup (PIV and color Doppler imaging)

5.2.2.1 Flow setup

Flow measurements were carried out on transparent, life-size carotid stenosis phantoms fabricated from PDMS with an 8 mm diameter and 2 mm wall thickness. The detailed fabrication process is explained in section 5.2.1. The experiments involved investigating four different carotid stenosis models. Each model comprised of a concentric stenosis with a diameter reduction of 50% or 60%. The stenoses were designed in two different shapes: Cosine and Gaussian.

These phantoms were connected to a closed circuit filled with a blood mimicking fluid (BMF). The BMF used in the experiments was prepared following the formulation outlined in the literature [13,54,63] by carefully combining 60% filtered water and 40% glycerol, resulting in a dynamic viscosity of approximately 4×10^{-3} Pa$\cdot$s and a density of 1030 kg$\cdot$m^{-3} which closely resemble the flow characteristics of human blood. Moreover, the chosen composition of the BMF was carefully determined to yield a refractive index of approximately 1.4 [50,91,101], which closely aligns with the refractive index of the PDMS material employed in the construction of the carotid stenosis phantoms to ensure accurate optical characterization. In addition, to minimize any optical distortion during PIV measurement process, the phantom portion of the experiment was immersed within a reservoir containing deionized water. This approach helps maintain the consistency of refractive indices and reduces the likelihood of optical deviations, thus enhancing the reliability and precision of the PIV measurements. Following the preparation of the BMF, the flow was seeded with Polyamide particles (PSP-50, 250g, DAN-

TEC DYNAMICS, Denmark) having a diameter of 50 μm. As per the observations made by Leinan *et al*. [46], it was ensured that these particles effectively followed the flow path and acted as tracers. This characteristic allowed for precise tracking and characterization of the particles within the experimental setup.

A gear pump drive with variable speed capability (Cole Parmer, USA) was utilized to generate a consistent flow for the experiments. The selected flow rates ranged from 0.2 to 1.2 $\mathrm{L \cdot min^{-1}}$, with a step size of 0.1 $\mathrm{L \cdot min^{-1}}$. These values were determined based on extensive review of existing literature that covers the typical range of mean and peak blood flow observed in pulsatile flow studies [112–114]. To ensure precise measurement of the flow rate, an electromagnetic flow meter (Picomag IO-Link, Endress+Hauser, Reinach, Switzerland) was employed. On the other hand, in order to ensure accurate flow rate measurement by the flow meter, it is recommended to adhere to the conductivity requirement stated in the user manual, which specifies a minimum conductivity of 20 $\mu\mathrm{s \cdot cm^{-1}}$ for the liquid. To meet this criterion while avoiding any alteration in the refractive index of the fluid, a sufficient amount of salt was dissolved in the liquid. This ensures that the conductivity level is maintained within the specified range. Furthermore, to stabilize and ensure consistency in the circulating fluid, it is advisable to allow it to flow uninterrupted for a period of at least half an hour. This duration allows the fluid to stabilize and minimizes any potential disturbances or fluctuations that could affect the accuracy of the flowrate measurement.

The relative pressures at the phantom inlets and outlets were carefully monitored using a catheter-based pressure transducer (VOLCANO ComboWire XT pressure/flow guide wire, Philips, CA, USA), shown in Figure 5.9, which was connected to a ComboMap pressure and flow system device. The obtained pressure drop values between the inlet and outlet were regarded as the reference standard (gold standard) [115, 116] against which the experimental results were compared. This approach allowed for precise evaluation and validation of the experimental outcomes, ensuring a reliable assessment of the measured parameters.

Figure 5.9: Pressure sensor tip guidewire used for measuring relative pressures during the *in vitro* experiment as gold standard values.

5.2.2.2 PIV data acquisition and analysis

For the PIV experiment, as described in section 2.3, a laser source (Laser interferometer MGL-F-532-2W, CNI, China) was used to generate a laser sheet that illuminated the region of interest. A digital high-speed camera (Phantom, Vision Research, NJ, USA) was employed, connected to a computer for data acquisition and image storage to capture the displacement of tracer particles in the flow and estimate the velocity vector field. The camera was set to its maximum resolution of 1024×512 pixels during image acquisition. Acquisitions were performed at a frame rate of 11000 frames per second, with an exposure time of approximately 90 μs and 533 frames were acquired for each case. All the mentioned equipment is part of LabTAU (Inserm U1032, Lyon, France) laboratory.

For processing the acquired images and estimating the 2D velocity vector field, we employed PIVlab [117], a user-friendly graphical user interface (GUI) software. PIVlab not only calculates the velocity distribution within particle image pairs but also facilitates the derivation, display, and export of multiple parameters related to the flow pattern. This comprehensive functionality of PIVlab enables fast and efficient data processing for PIV experiments. Within this software, the computation of particle displacement is accomplished by assessing the cross-correlation of numerous small sub-images, referred to as interrogation areas. Cross-correlation, being a statistical pattern matching technique, provides the most probable displacement for a group of particles moving along a linear path between pairs of images. The discrete cross-correlation function, as depicted by Equation (5.1), is as follows:

$$C(m,n) = \sum_i \sum_j A(i,j)B(i-m, j-n). \tag{5.1}$$

In the aforementioned equation, A and B represent the corresponding interrogation areas extracted from image A and image B, respectively. By analyzing the resulting correlation matrix C, the correlation peak's position provides the most likely displacement of the particles from A to B. PIVLab consists of three main stages, namely pre-processing, image evaluation, and post-processing:

During the *pre-processing* step, PIVLab applies several techniques to enhance the quality of the input images. These techniques include background subtraction, image filtering, and image correlation, which collectively contribute to improving the accuracy and reliability of velocity measurements.

In the *image evaluation* step, which constitutes the main stage of PIVLab, two commonly employed approaches are used to solve Equation (5.1) to determine the particle displacements and velocities:

- The first approach is the direct cross-correlation (DCC), which is the most straightforward method. It involves calculating the correlation matrix in the spatial domain.

- The second approach involves computing the correlation matrix in the frequency domain using a fast Fourier transform (FFT).

Each approach has its own advantages and drawbacks. In our study, we decided to employ the FFT approach for data processing due to its lower computational cost. However, it is worth noting that the FFT method assumes interrogation areas of identical size, resulting in some loss of information for each particle displacement. To mitigate this loss of information, we performed multiple passes of the FFT approach on the same data. This iterative approach helps minimize the overall impact of particle displacement-induced information loss.

The final step in PIVLab is the *post-processing* stage. During this step, PIVLab incorporates validation techniques to evaluate the quality and reliability of the measured velocities. This involves the implementation of outlier rejection algorithms, which are designed to eliminate invalid or inconsistent velocity vectors that may result from noise, false particle images, or other sources of error. Furthermore, it provides a comprehensive set of visualization tools to analyze and interpret the obtained velocity fields. These tools include vector display, contour plotting, statistical analysis, and the ability to export data for further analysis.

5.2.2.3 Color Doppler ultrasound data acquisition and analysis

To acquire color Doppler ultrasound images, we used the GE ultrasound scanner (Vivid iq Premium, GE Healthcare) along with a GE 9L linear probe for measuring color Doppler velocities. During acquisition, we adjusted the frequency to 5 MHz and the pulse repetition frequency between 3 and 11.37 kHz, depending on the flow rate (ranging from 0.2 to 1.2 $\mathrm{L \cdot min^{-1}}$). Each acquisition had a duration of 3 seconds, resulting in 50 frames. The angle of acquisition was set to $-15°$ and $-20°$. To enhance acoustic coupling, minimize interference, and improve image quality while imaging the carotid stenosis phantom, we employed water as a medium material. To achieve this, we immersed the head of the probe in a water reservoir. This setup facilitated efficient energy transfer and reduced artefacts.

After the acquisition of color Doppler data, the raw data were extracted using the EchoPAC. EchoPAC is a software application specifically designed for GE Healthcare ultrasound devices. The extracted data contains various parameters, including the type of probe utilized, the ultrasound system employed, the acquisition mode, B-mode and Doppler data information. Subsequently, this extracted information was consolidated into an HDF file. The file was then processed using the functions developed in the MUST toolbox, as described in section 5.1. Figure 5.10 depicts the final experimental setup employed for the acquisition of dual modalities, namely PIV and color Doppler ultrasound.

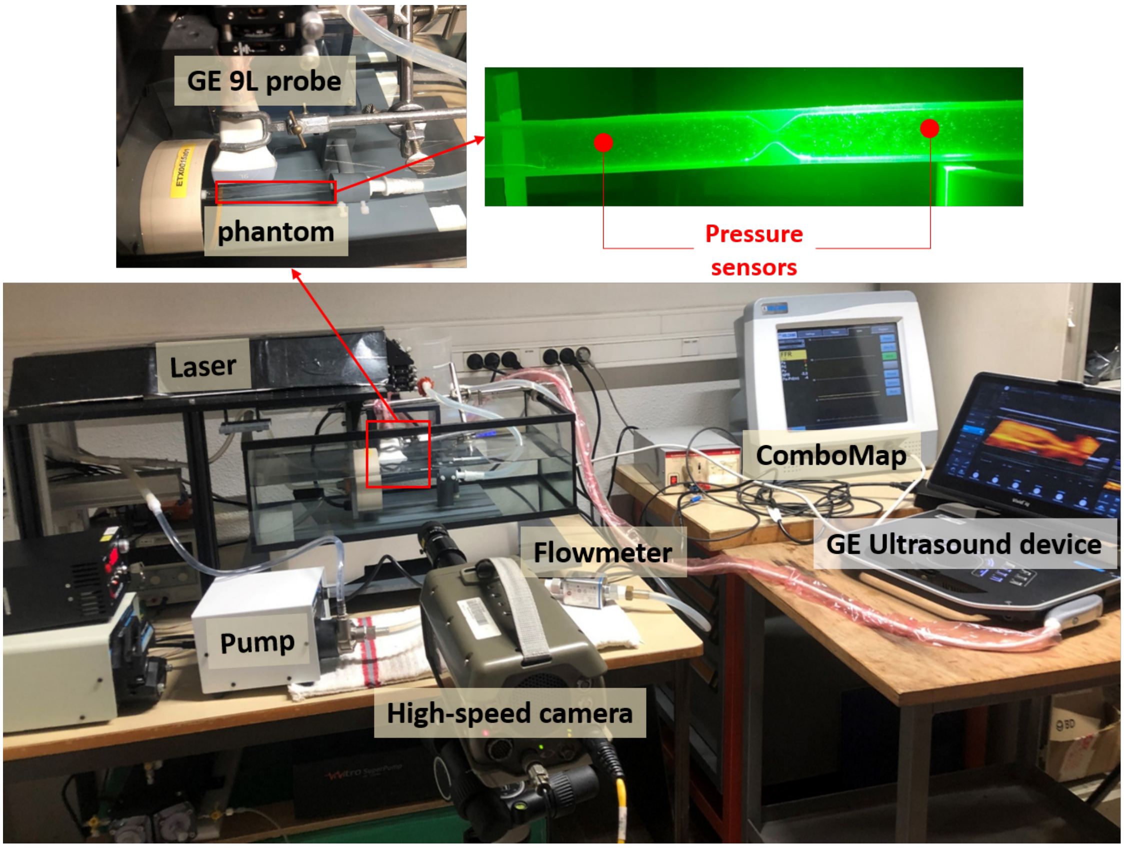

Figure 5.10: Single experimental setup for PIV and color Doppler ultrasound imaging.

5.3 Color Doppler ultrasound experiment

5.3.1 Color Doppler phantom fabrication

Since we could not obtain accurate results from the PDMS phantom during ultrasound imaging, as described in section 5.2.1.3, we decided to conduct separate color Doppler experiments in a distinct experimental setup to ensure reliable and scientifically sound data acquisition. To facilitate this, we recognized the need for a suitable phantom that would not only be compatible with echography but also fulfill other criteria specific to our study. According to the existing literature, materials that are commonly considered as optimal and compatible for ultrasound imaging are those that exhibit favorable characteristics similar to water and human body tissue in terms of speed of the sound and attenuation. Among these materials, PVA cryogel and agar have undergone extensive study and have been widely acknowledged for their suitability in this context.

PVA hydrogel: As explained in section 5.2.1.3, this material can be used for ultrasound phantom fabrication, displaying its suitability for creating both walled and wall-less phantoms depending on the specific experimental requirements and objectives. For instance Chee *et al.* [118] used it to fabricate walled anatomically realistic carotid bifurcation phantoms with artery-like vessel elasticity and high acoustic compatibility then mounted that inside a box and filled it with agar. In contrast, Olesen *et al.* [13] and Nguyen *et al.* [76] adopted a wall-less phantom approach using the lost-core technique (section 5.2.1), where PVA was cast within a designated container.

Agar: It is a gelatinous substance derived from red algae which is commonly used in scientific applications. Its fabrication process involves carefully mixing a specific percentage of agar powder with water, with the ratio depending on the desired stiffness. The mixture is stirred using a magnetic stirrer in a step-by-step manner. Subsequently, the mixture is heated to $80°C$ to achieve the desired consistency. Finally, the prepared mixture is poured into the desired cast or mold to solidify. The mechanical characteristics of agar, such as its inherent lack of rigidity and consistency, make it suitable for creating wall-less phantoms primarily through the lost-core casting technique [94, 119].

In accordance with the existing literature, we initially fabricated phantoms with walls using PVA (as detailed in section 5.2.1). However, despite subjecting the samples to a high number of freeze and thaw cycles to enhance the material's rigidity, we encountered challenges in meeting our desired criteria for rigidity and consistency. Specifically, even at low flow rates, the passage of flow through the phantom resulted in undesired inflation, compromising the experimental consistency conditions and impacting the quality of the obtained data. Consequently, the obtained results were affected adversely. As a result, we made the decision to transition to a wall-less phantom approach, and in this regard, agar emerged as a superior choice compared to PVA. It exhibited several advantages, including a shorter preparation time and a simpler fabrication process. Using the same cores employed in the PIV phantom fabrication (section 5.2.1.1), we proceeded by affixing them within a designated box, ensuring a distance of 2cm between the core and the box surface. Subsequently, we carefully poured the previously prepared agar mixture into the container, allowing it to cool down and solidify. The phantoms were then placed in a refrigerator for a duration of one day. The following day, once the agar material had sufficiently solidified, we delicately removed the two core pieces. This process posed certain challenges due to the vacuum created between the two core parts and the presence of sharp connectors. Regrettably, this resulted in some phantom damage, necessitating the production of multiple phantoms. To assess the integrity and completeness of the delicate and sensitive stenosis section of the phantom, we utilized B-mode ultrasound imaging. This meticulous evaluation aimed to ensure that the stenosis region remained intact and free from any defects. Figure 5.11 illustrates example of fabricated color Doppler ultrasound phantoms.

Figure 5.11: Color Doppler ultrasound phantoms fabrication. (top) Pre-poured cast shows the core placement. (bottom) Casts after pouring agar into them. The black grips were employed to secure and maintain the cohesion of the two core pieces, ensuring the creation of an intact stenosis section.

5.3.2 Color Doppler ultrasound experimental setup

For the *in vitro* experimental setup involving color Doppler ultrasound imaging, we employed the same flow setup as described in section 5.2.2.1 for PIV experiments. However, instead of incorporating Polyamide particles, we introduced corn starch particles into the fluid. These particles were utilized to simulate the behavior of red blood cells in blood flow, ensuring the generation of sufficient echoes from the scatterers. This modification enabled us to accurately capture and analyze the Doppler signals during the imaging process. For the acquisition and analysis of the color Doppler ultrasound images, we followed the method and utilized the same materials as described in section 5.2.2.3. Figure 5.12 depicts the employed experimental setup for the acquisitions.

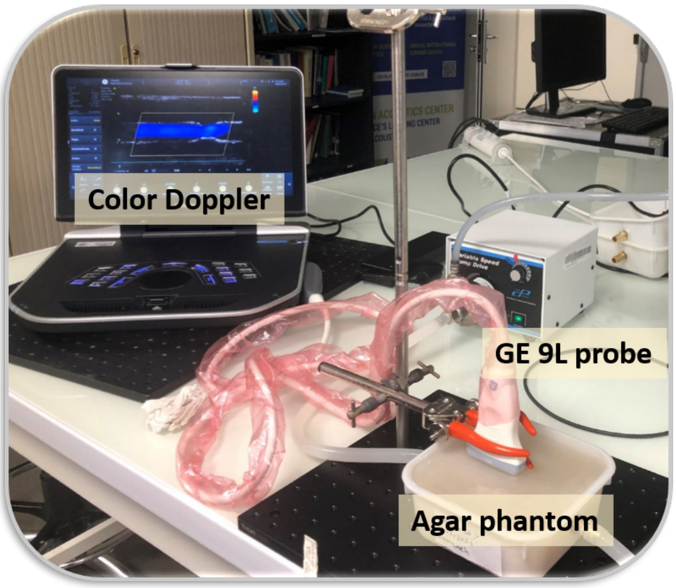

Figure 5.12: Color Doppler ultrasound experimental setup for acquisition of color Doppler images.

6

Results of the Non-invasive Pressure Loss Estimation

This chapter presents all the results of the validation process for the developed non-invasive method of estimating trans-stenotic pressure loss using clinical color Doppler. The validations were carried out in two stages. The first stage was an in silico validation through CFD and color Doppler simulation (SIMUS) on carotid stenosis models. The second stage was an in vitro validation through experiments using PIV and color Doppler ultrasound imaging on carotid stenosis phantoms. The results demonstrated a strong correlation between the estimated pressure losses and the provided reference values, confirming the reliability and feasibility of this method.

Contents

To achieve the objective of our study, non-invasive estimation of trans-stenotic pressure loss from clinical color Doppler images in carotid stenosis, we developed a two-fold method. Initially, we employed the 2D-vVFM technique (refer to section 4.1) to extract a velocity vector field from the color Doppler velocities. Following this, we applied our fluid dynamics equation method which is a combination of the Bernoulli and Navier-Stokes equations (refer to section 4.3), to compute the post-stenotic pressure loss. In order to verify this non-invasive technique, we initiated two validation steps. The first involved an *in silico* validation via CFD and ultrasound simulations (SIMUS). We simulated flow conditions in carotid stenosis models using CFD, then replicated Doppler velocities from the CFD results using SIMUS. We retrieved the velocity vector field from the simulated color Doppler field using vVFM and then estimated pressure losses from them, comparing it with the CFD-derived ground truth. The second validation was conducted *in vitro*, employing PIV and color Doppler ultrasound imaging experiments on carotid stenosis phantoms. We estimated the pressure losses using our developed method and compared it to pressure loss values measured by pressure sensors throughout the experiment, considered as the gold standard. Similarly, for the Doppler technique, we retrieved the 2D velocity field from color Doppler velocities using vVFM, estimated the pressure from them, and then compared it with pressure sensor values which served as our reference. In this chapter, we present the results of each validation step, affirming the validity of our proposed strategy. The results provide compelling evidence of the accuracy and reliability of our non-invasive approach to estimating trans-stenotic pressure loss in carotid stenosis.

6.1 CFD and ultrasound simulations

As a reminder, the *in silico* simulations were executed on two types of stenosis shapes: Cosine and Gaussian. These were evaluated at stenosis degrees of 60% and 70% diameter occlusion, and across three different flow rates (for more details refer to section 5.1). To validate the vVFM technique (4.1) *in silico*, we conducted a step in which we employed this method to estimate the velocity vector field from simulated Doppler velocities. Subsequently, we compared the resulting velocity values obtained from vVFM ($\{v_{x-v\mathrm{VFM}}, v_{z-v\mathrm{VFM}}\}$) with those obtained from the original CFD velocity fields ($\{v_{x-\mathrm{CFD}}, v_{z-\mathrm{CFD}}\}$). Figure 6.1 presents an illustrative example of simulated color Doppler for a 60% stenosis (diameter reduction) Cosine-shaped common carotid model, with a blood flow rate of 1 $\mathrm{L \cdot min^{-1}}$. The corresponding 2D velocity field obtained via the vVFM method is compared with the ground-truth field, derived from CFD. The comparison between these two fields enables a quantitative evaluation of the performance of the vVFM approach in terms of velocity values (measured in $\mathrm{m \cdot s^{-1}}$). In addition, Figure 6.2 demonstrates the 2D velocity map of the same carotid stenosis model, comparing both approaches.

To estimate the accuracy of the velocity field reconstruction proposed by the 2D-vVFM, we compared the error between the x and z components of the velocity fields estimated by our technique and the reference from the CFD model using the root-mean-squared errors (RMSE), normalized by the maximum velocity (nRMSE), which is defined by the following equation:

$$\mathrm{nRMSE} = \frac{1}{\max \parallel v_{\mathrm{CFD}} \parallel} \sqrt{\frac{1}{n} \sum_{k=1}^{n} \parallel v_{v\mathrm{VFM}_k} - v_{\mathrm{CFD}_k} \parallel^2} \tag{6.1}$$

where, n represents the number of velocity samples within the common carotid artery. The estimated velocity and the reference velocity are denoted by $v_{v\mathrm{VFM}}$ and v_{CFD}, respectively. Finally,

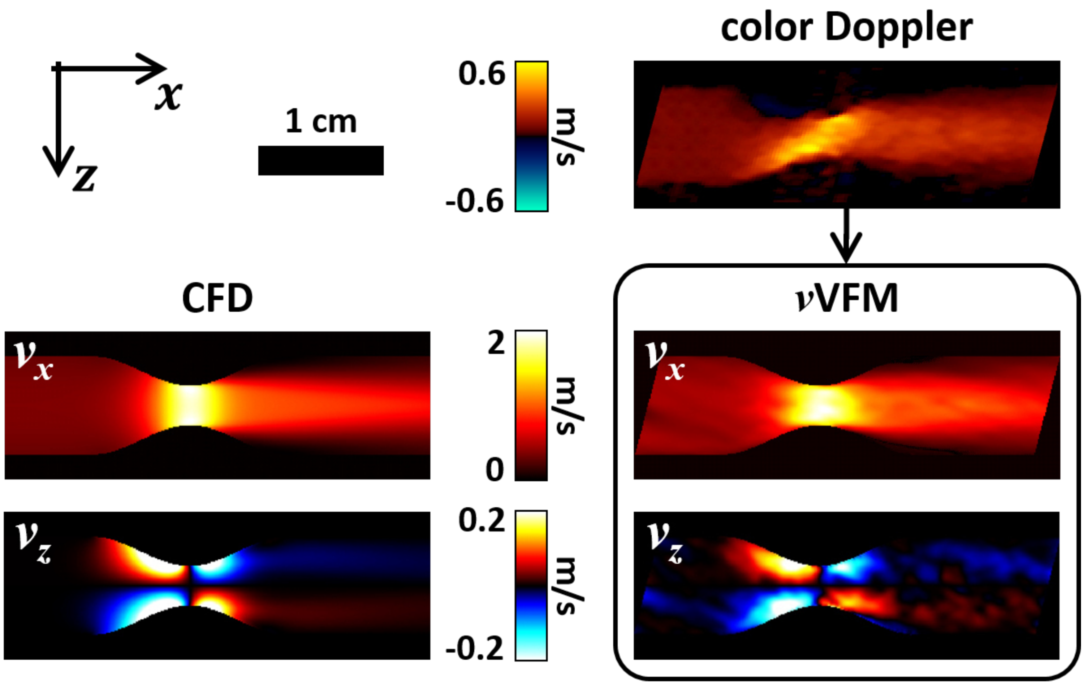

Figure 6.1: (left column) The original CFD components are given for a comparison. (right) Realistic simulation of color Doppler imaging in an axisymmetric stenosis. The vVFM method returns the vector components v_x, v_z .

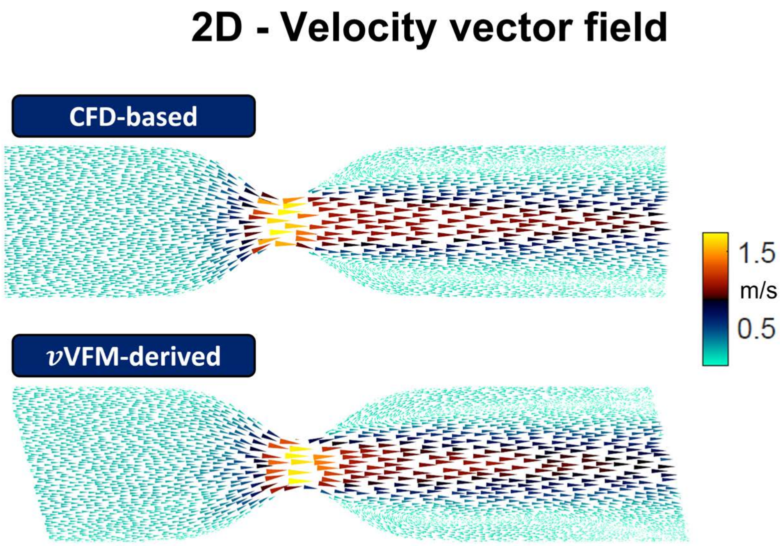

Figure 6.2: Comparison of 2D velocity vector fields in an axisymmetric Cosine-shaped, 60% stenosis common carotid model using CFD (ground-truth) and vVFM approaches in an *in silico* simulation. The top panel displays the CFD data, while the bottom panel shows the corresponding vVFM data.

Table 6.1: nRMSE (in %) between the *v*VFM and CFD in the *x* and *z* directions. Four simulated carotid stenosis models and three flow rates were proposed.

Shape / degree	Velocity component	Flow rate [$\mathrm{L \cdot min^{-1}}$]		
		0.3	**0.6**	**1**
Cosine 60%	$\mathbf{v_x}$	6.0	4.5	5.3
	$\mathbf{v_z}$	1.2	1.0	1.2
Cosine 70%	$\mathbf{v_x}$	4.6	4.7	4.8
	$\mathbf{v_z}$	1.0	1.0	1.0
Gaussian 60%	$\mathbf{v_x}$	4.7	6.1	5.0
	$\mathbf{v_z}$	1.5	1.5	1.3
Gaussian 70%	$\mathbf{v_x}$	3.8	4.8	4.1
	$\mathbf{v_z}$	1.1	1.2	1.0

the mean is normalized with respect to the maximum value of the CFD velocity magnitude. The nRMSE values in *x*- and *z*- directions for each model in different flow rates are listed in Table 6.1. These values are smaller than 6.1% and 1.5% in both directions, which tend to indicate that the *v*VFM technique can accurately estimate velocity vector field from Doppler velocities in arterial stenoses. To demonstrate the agreement between the velocities derived using *v*VFM and those calculated by CFD, a log-based regression analysis was performed. The analysis involved the data of maximum velocity magnitudes of the midline using *v*VFM, as well as the CFD results. This comparison was conducted across common carotid stenosis models, considering different stenosis shapes, degrees of occlusion, and flow rates, as outlined in Table 6.1. The log-based regression analysis revealed a strong agreement between these two datasets, as depicted by the regression line equation: $y = 1.02x - 0.03$. Furthermore, the coefficient of determination exhibited a high value of $r^2 = 0.99$, affirming that the estimated velocities are effectively replicated by the *v*VFM method. Figure 6.3 provides a visual representation of this comparison, illustrating the consistency and accuracy of the velocity measurements.

The next step involved an investigation into the validity of our proposed method for estimating pressure drops, which combines the Bernoulli and Navier-Stokes equations (refer to section 4.3). We aimed to assess whether this method could effectively estimate pressure losses using the velocity vector field obtained from *v*VFM. To accomplish this, we conducted a comparison between the estimated pressure drops using *v*VFM and those calculated by CFD, which served as the ground truth. Figure 6.4 illustrates the corresponding results. A log-based regression analysis of the data shows a strong linear relationship with an equation of $y = 1.01x - 0.02$ and a high coefficient of determination of $r^2 = 0.96$. It indicates a robust correlation between the two methods and confirms the validity and accuracy of the proposed non-invasive *v*VFM method along with the proposed method of pressure drop calculation.

In Figure 6.5, we presented two examples illustrating the *v*VFM-derived relative pressure along the midline of a common carotid stenosis model in comparison with the CFD results. The examples feature stenoses with Cosine-shaped and Gaussian-shaped profiles, with diameter reductions of 60% and 70%, respectively. The flow rate in these simulation was set at 1 $\mathrm{L \cdot min^{-1}}$. The results of these *in silico* simulations validate our established approach for reconstructing intravascular flow using color Doppler ultrasound and estimating post-stenotic pressure losses, and confirm the feasibility and accuracy of this technique. The next sections will further assess its reliability via *in vitro* experiments conducted on homemade common carotid stenosis phantoms.

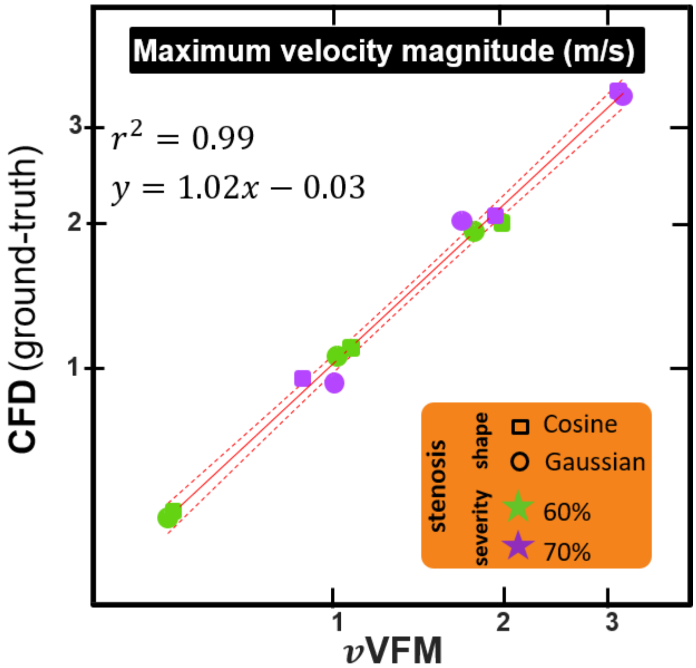

Figure 6.3: Comparison of the vVFM-derived maximum velocity magnitude along the midline with the actual CFD values (in a logarithmic scale to get a uniform distribution) based on 12 simulations: two stenosis shapes, two degrees of severity, three flow rates (refer to Table 6.1).

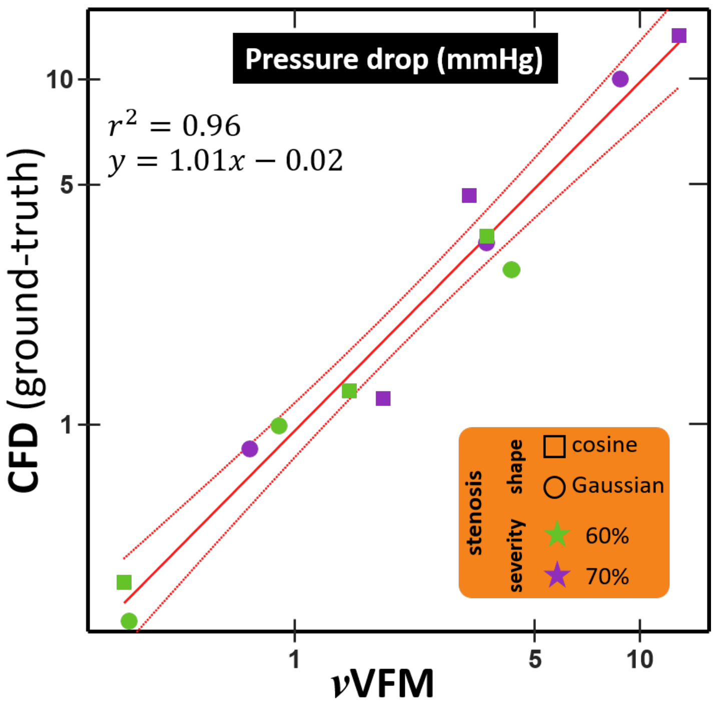

Figure 6.4: Comparison of the vVFM-derived pressure drops along the midline with the actual CFD values (in a logarithmic scale to get a uniform distribution) based on 12 simulations: two stenosis shapes, two degrees of severity, three flow rates (refer to Table 6.1).

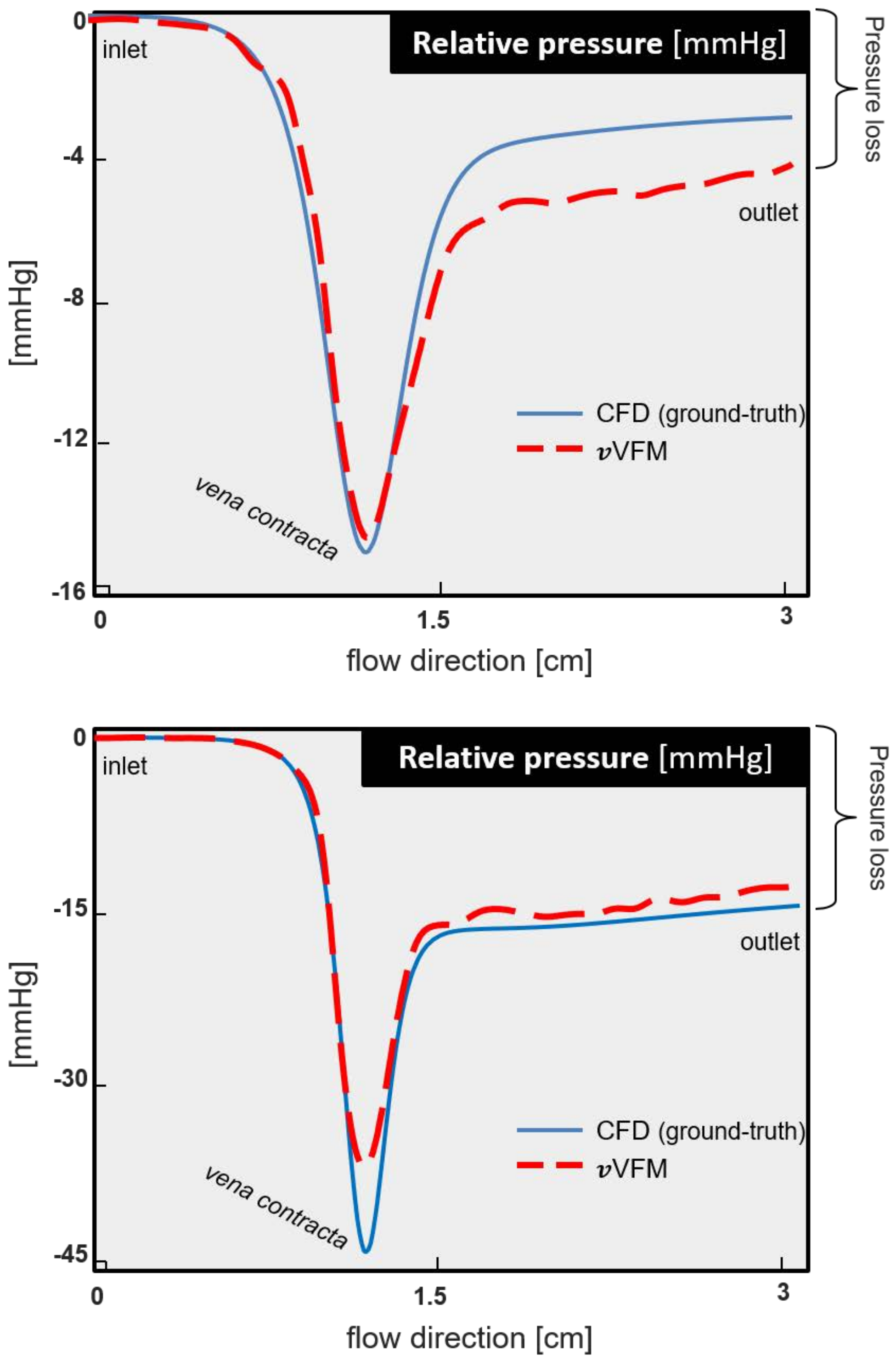

Figure 6.5: vVFM-derived estimated relative pressures in comparison with the CFD calculated results. (top) Cosine-shaped common carotid model with 60% of stenosis. (bottom) Gaussian-shaped common carotid stenosis model with 70% of constriction. In both cases, the flow rate is set to 1 $\text{L} \cdot \text{min}^{-1}$.

6.2 PIV *in vitro* experiments

To validate our non-invasive technique for estimating pressure drop in arterial stenosis, we conducted *in vitro* experiments on carotid artery stenosis phantoms using PIV method. The methodology and materials employed for the creation of these phantoms, as well as the specifics of our experimental setup, are detailed in section 5.2. In summary, a total of 44 experiments were conducted, utilizing both Cosine and Gaussian-shaped phantoms. These phantoms reflected a reduction in diameter of 50% and 60%, mirroring mild to moderate stenosis as per the NASCET criteria [9]. Flow rates investigated in this study spanned from 0.2 to 1.2 $\mathrm{L \cdot min^{-1}}$, thereby covering the physiological blood flow rates in peripheral vessels 5.2.2.1.

Given the capacity of PIV to yield instantaneous and accurate velocity vector fields of a flow, conducting these experiments enabled us to obtain the velocity data. This in turn facilitated the application of our proposed method for estimating post-stenotic pressure loss, allowing us to evaluate its accuracy and reliability. Figure 6.6 illustrates a comparison between the pressure losses derived from PIV and those obtained from our reference pressure sensors embedded within the carotid stenosis phantoms during the experiment. The logarithmic regression analysis of the data revealed a strong linear relationship, characterized by the equation $y = 0.93x + 0.14$ and a high coefficient of determination ($r^2 = 0.94$). This robust correlation confirms the validity and accuracy of our proposed method for estimating post-stenotic pressure drop.

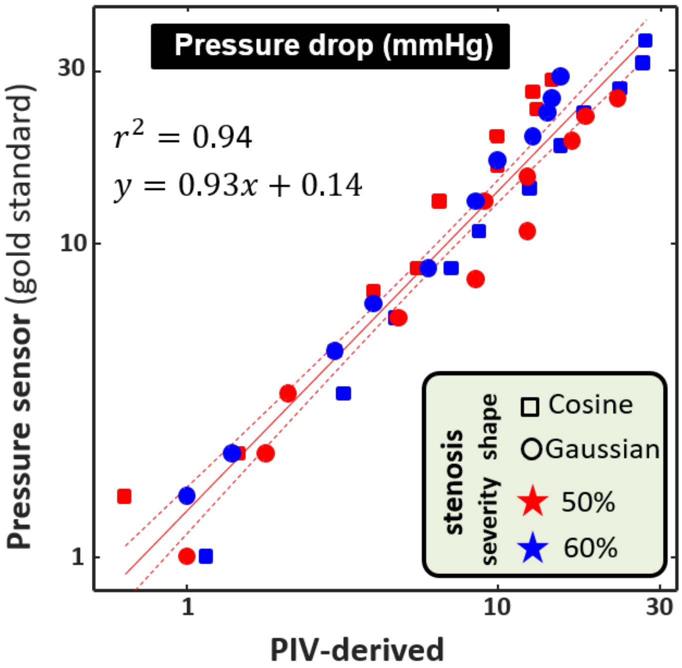

Figure 6.6: Logarithmic-scale comparison of PIV-derived pressure drops with actual pressure sensor values across 44 carotid stenosis phantoms in PIV experiments.

To evaluate the influence of flow rate on pressure drop values, we utilized the Bland-Altman plot for agreement analysis across all experimental results, as demonstrated in Figure 6.7. The findings indicate that as the flow rate increases, the discrepancy between PIV-derived estimated pressure drops and our gold standard measurements (the pressure sensor values) becomes more pronounced. This observed phenomenon aligns with anticipated outcomes, given that our method involves capturing a 2D axisymmetric data from a real 3D experiment, which inherently leads to information loss along one dimension. As the flow rate increases, the turbulence within

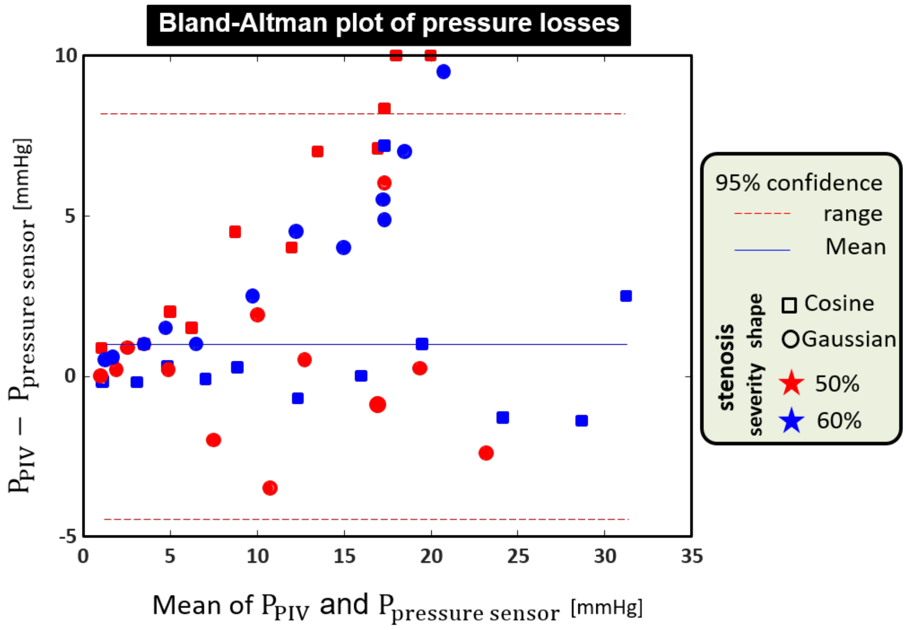

Figure 6.7: Bland-Altman plot illustrating the estimated pressure losses in 44 PIV *in vitro* experiments.

the post-stenosis divergent area intensifies. However, when we smooth the velocity, the spatial resolution decreases, which can lead to an underestimation of the spatial gradient.

Figures 6.8 to 6.11 depict the estimated velocity vector fields within the phantoms, illustrated for representative flow rates of 0.5 and 1 $L \cdot min^{-1}$. Correspondingly, each figure also presents the estimated pressure drop for each case alongside pressure sensor readings, which serve as our reference values. The range of the estimated maximum velocities for the jet created in the divergent area after stenosis varied from 0.56 to 2.8 $m \cdot s^{-1}$ and 0.7 to 3.94 $m \cdot s^{-1}$ for the lowest (0.2 $L \cdot min^{-1}$) and highest (1.2 $L \cdot min^{-1}$) flow rates, respectively, in the Cosine-shaped cases with 50% and 60% occlusion. In the Gaussian-shaped cases with 50% and 60% stenosis, the velocity range was between 0.6 to 2.7 $m \cdot s^{-1}$ and 0.6 to 3.5 $m \cdot s^{-1}$, respectively. These results demonstrate that the velocity ranges in both models closely align, with slightly higher values noted in Cosine-shaped models than in Gaussian-shaped ones for a fixed stenosis degree and flow rate. An increase in flow rate leads to higher jet velocities then greater post-stenotic turbulence due to the mixing of different flow layers, resulting in more pressure losses. In some of velocity vector field figures, an observable deviation from axisymmetry is evident in the jet flow, which tends towards one side. This deviation can be attributed to the phantom's geometry, particularly at the juncture where two sections of the core meet in the midst of the stenosis. This non-uniformity is somewhat inevitable given the tiny and delicate dimensions of the stenosis, which prevent absolute control over the fabrication process. Occasionally, residuals persist in situ, thereby contributing to the observed flow asymmetry.

The outcomes of these *in vitro* experiments validate our post-stenotic pressure loss approach and confirms the feasibility and precision of this proposed technique. Even with limitations that induced flow asymmetry, contrary to our initial axisymmetric assumption, the methodology remains effective and robust. It is noteworthy to highlight that, upon examination of velocity and pressure drop values across all tested models, the degree of stenosis appears to exert a more pronounced influence on increasing pressure drop values than the shape of the stenosis, assuming the model's axisymmetric configuration.

As explained in section 5.2.2, our intention was to construct a dual modality experimental

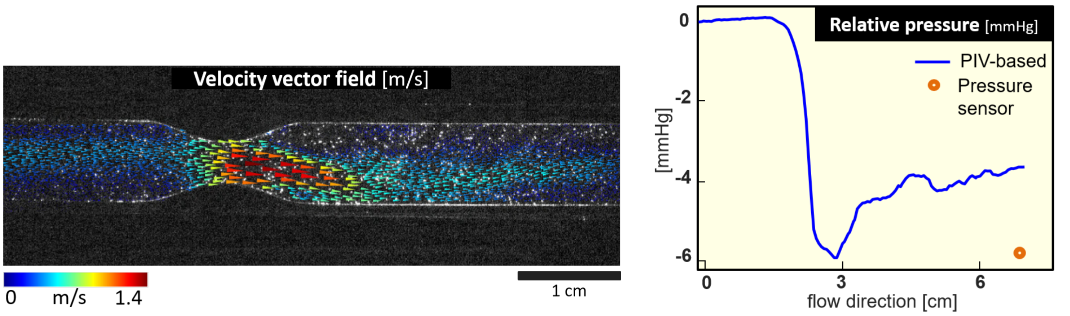

(a) (b)

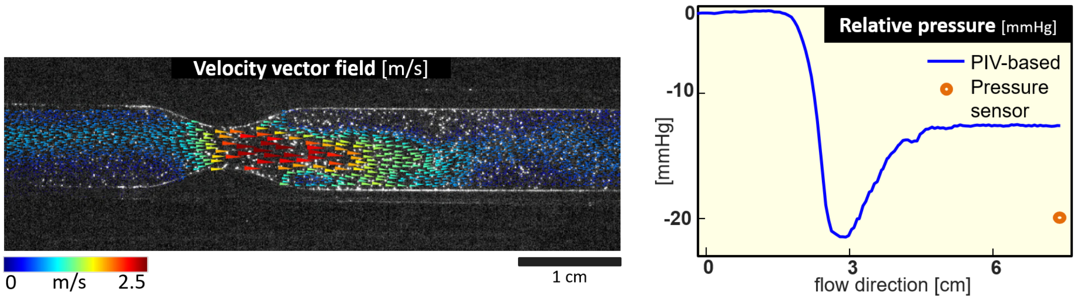

(c) (d)

Figure 6.8: (a,c) PIV-derived velocity fields and (b,d) associated relative pressures for a Cosine-shaped 50% carotid stenosis phantom at flow rates of (top) 0.5 and (bottom) 1 $L \cdot min^{-1}$.

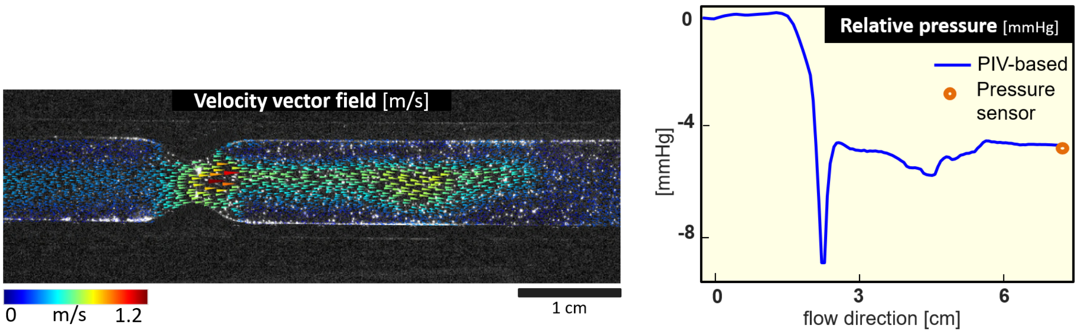

(a) (b)

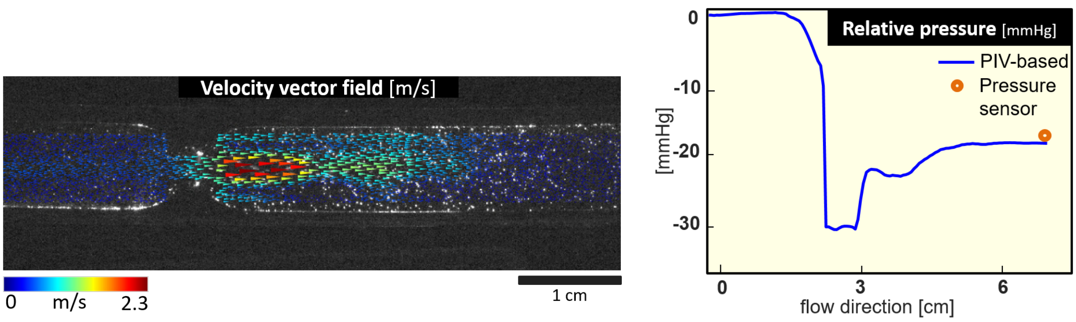

(c) (d)

Figure 6.9: (a,c) PIV-derived velocity fields and (b,d) associated relative pressures for a Gaussian-shaped 50% carotid stenosis phantom at flow rates of (top) 0.5 and (bottom) 1 $L \cdot min^{-1}$.

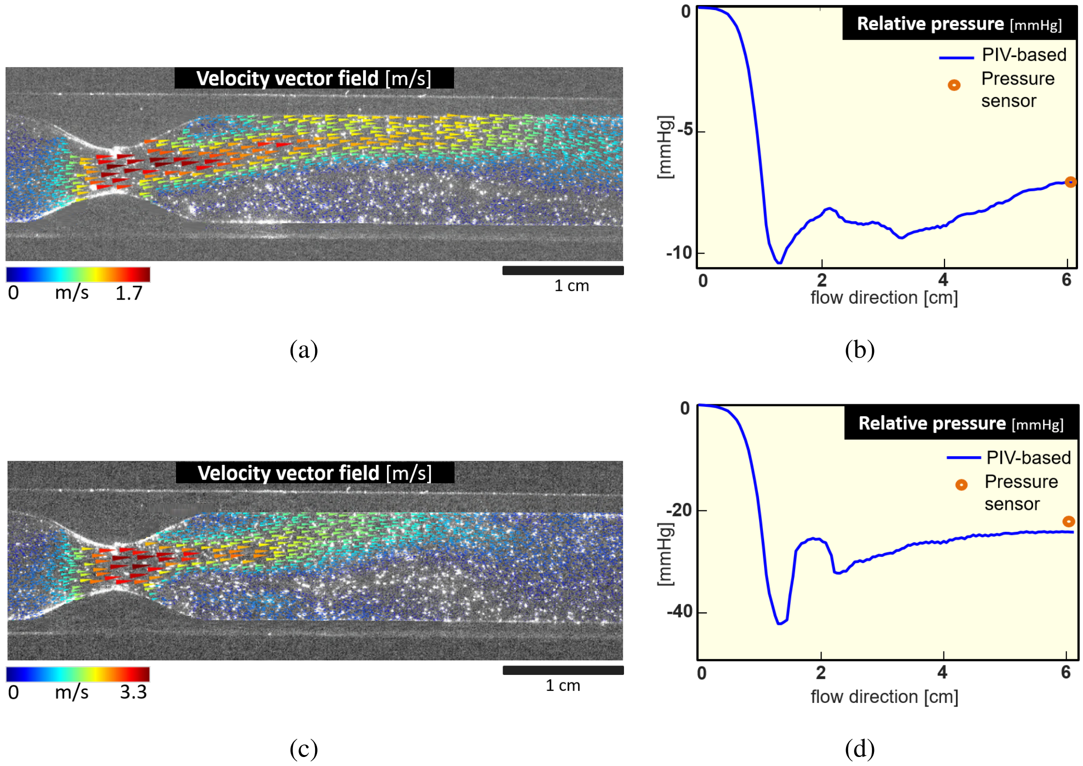

Figure 6.10: (a,c) PIV-derived velocity fields and (b,d) associated relative pressures for a Cosine-shaped 60% carotid stenosis phantom at flow rates of (top) 0.5 and (bottom) 1 $\mathrm{L \cdot min^{-1}}$.

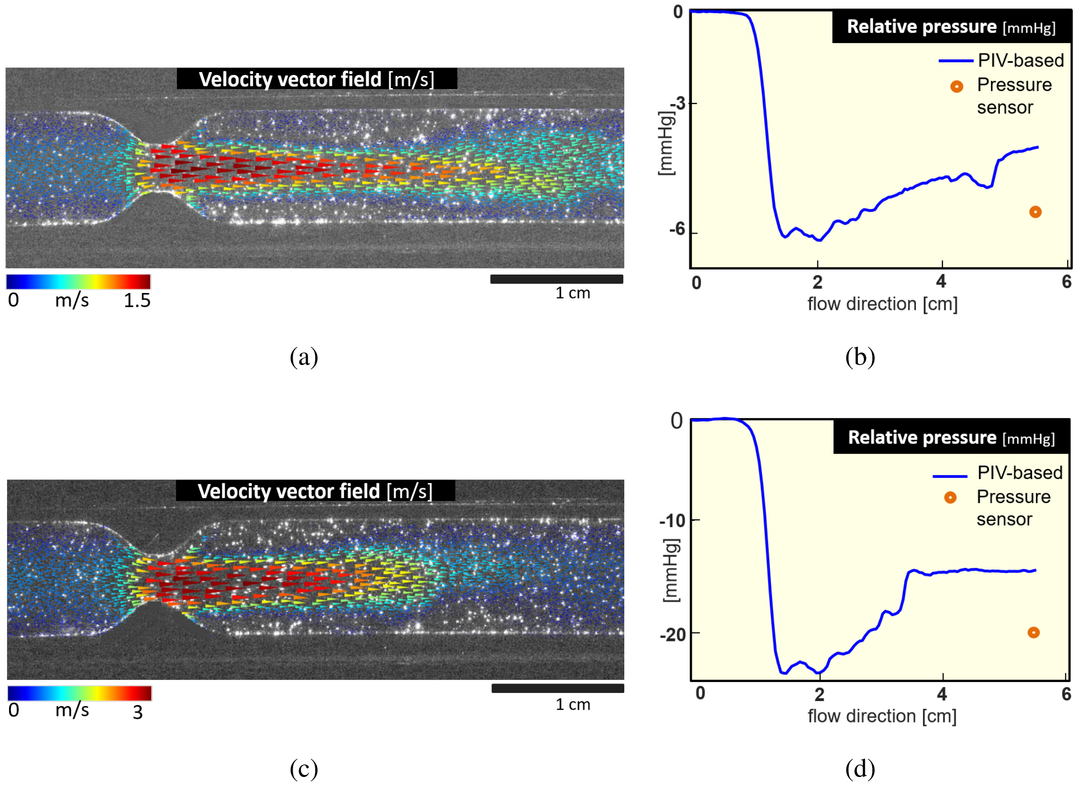

Figure 6.11: (a,c) PIV-derived velocity fields and (b,d) associated relative pressures for a Gaussian-shaped 60% carotid stenosis phantom at flow rates of (top) 0.5 and (bottom) 1 $\mathrm{L \cdot min^{-1}}$.

setup, facilitating simultaneous PIV experiments on transparent PDMS phantoms while concurrently acquiring color Doppler images of the same phantoms. This concurrent approach was intended to maintain uniformity in experimental conditions for both imaging modalities, thus promoting the accuracy of the estimated results for both *in vitro* experiments. However, due to the distinct ultrasonic properties of PDMS, as determined through our self-conducted speed of sound measurements in a PDMS sample (refer to section 5.2.1.3), we anticipated difficulties. Notably, the measured speed of sound was found to be lower than that in water and body tissue. Consequently, these measurements suggested that we might not attain our desired experimental results. Figure 6.12 confirms our initial predictions. In the B-Mode image, the walls of the stenotic phantom were not accurately detected (see yellow arrows), leading to inaccuracies in the subsequent Doppler field image of the flow in the phantom. This can be visible in the red curve shape that appears immediately after the stenosis, highlighted within a yellow circle. Furthermore, this shape expanded in response to an increase in flow rate, providing additional evidence of the experimental inconsistencies.

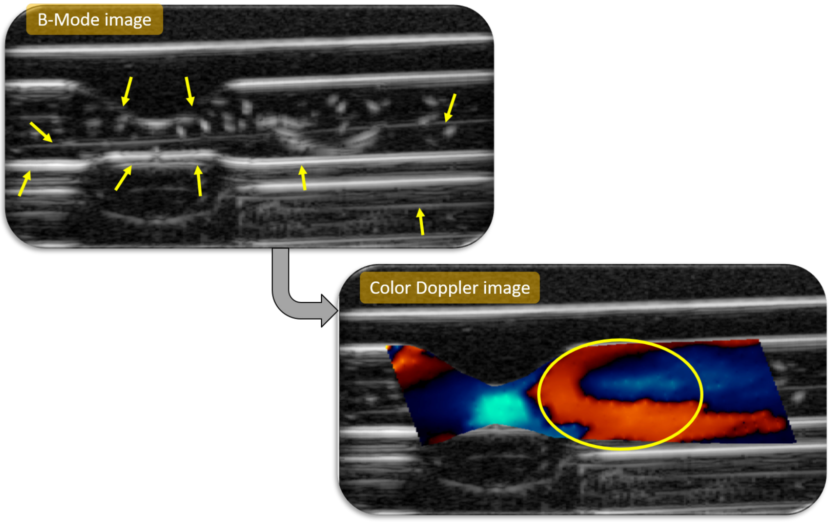

Figure 6.12: Ultrasound imaging of a transparent PDMS phantom. The top panel illustrates the B-Mode image with inaccurately identified vessel walls. The bottom panel displays the color Doppler velocity field within the same phantom, demonstrating an erroneous velocity field as evidenced by the formation of a red curve within the stenotic region (highlighted by a yellow circle).

In light of these constraints, we decided to establish a distinct experimental setup solely for *in vitro* color Doppler imaging, employing a wall-less agar carotid stenosis phantom (see section 5.3.1).

6.3 Color Doppler *in vitro* experiments

The final validation phase of the non-invasive technique for estimating trans-stenotic pressure loss utilizing clinical color Doppler was carried out through *in vitro* experiments. These were performed on carotid stenosis phantoms using a portable GE ultrasound device. The specifics of the method and materials employed in this process are detailed in section 5.3.2. During these experiments, color Doppler images were initially acquired. Subsequently, the *v*VFM method was applied to calculate the velocity vector field from the scalar color Doppler velocity data. With this information, the pressure loss downstream of the stenosis was estimated using our methodology, which integrates the Bernoulli and Navier-Stokes equations. As outlined in section 5.2.2, a total of 44 experiments were conducted, encompassing two types of stenosis profiles, Cosine and Gaussian, each at two degrees of occlusion (50% and 60% of diameter reduction). These profiles were evaluated at 11 different flow rates, ranging from 0.2 to 1.2 $L \cdot min^{-1}$. To compare the pressure drops estimated via the vVFM method with those directly measured by pressure sensors during the experiment within the carotid stenosis phantoms sensors, we generated a regression plot, as illustrated in Figure 6.13. The two data-sets demonstrated a strong correlation, characterized by the equation $y = 0.97x + 0.12$, with a coefficient of determination of $r^2 = 0.97$. This high degree of correlation further confirms the validity and accuracy of our proposed method for estimating pressure loss downstream of the stenosis.

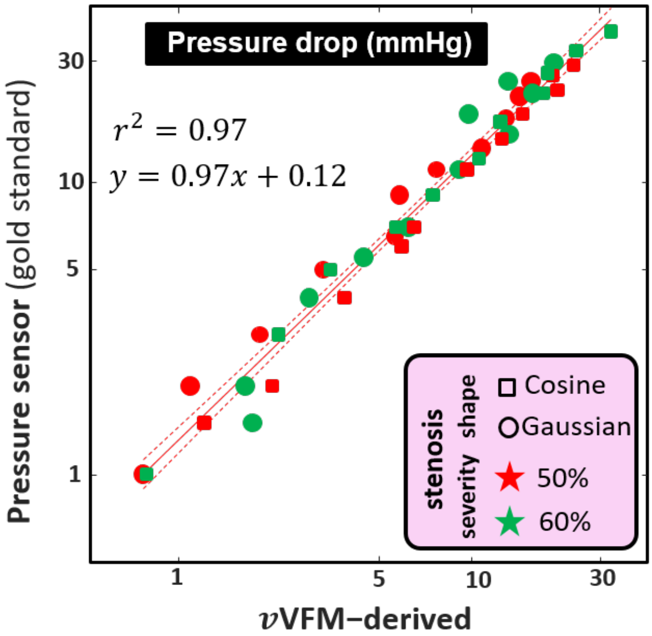

Figure 6.13: Logarithmic-scale comparison of vVFM-derived pressure drops with actual pressure sensor values across 44 carotid stenosis phantoms in color Doppler experiments.

We also conducted a Bland-Altman analysis, as shown in Figure 6.14, to assess the pressure losses across all experimental results. Similar to what we observed with the PIV method, our technique's accuracy in estimating pressure drops decreased as the flow rate increased. This is expected as we are capturing data of a 3D phenomenon within a 2D axisymmetric geometry. As the flow rate rises, the turbulence within the post-stenosis divergent region becomes more pronounced. Nevertheless, the smoothing of velocity results in a reduction in spatial resolution, potentially causing an underestimation of the spatial gradient.

Figures 6.15 to 6.18 provide examples of color Doppler images and their corresponding vVFM-derived velocity vector fields. Additionally, they display the estimated relative pressures along the midline for each phantom case in comparison with trans-stenotic pressure loss values measured by sensors (as gold standard), all evaluated at a flow rate of 0.7 $L \cdot min^{-1}$. In terms of maximum velocity comparison with PIV imaging, the two methods were performed in distinct experimental setups. However, the velocity ranges for each phantom, under the defined flow rates, were consistent across both methods. This convergence provides further validation for the vVFM method in retrieving velocity vector fields. For the Cosine-shaped phantoms with 50% and 60% occlusion, the maximum velocity within the stenotic region ranged between

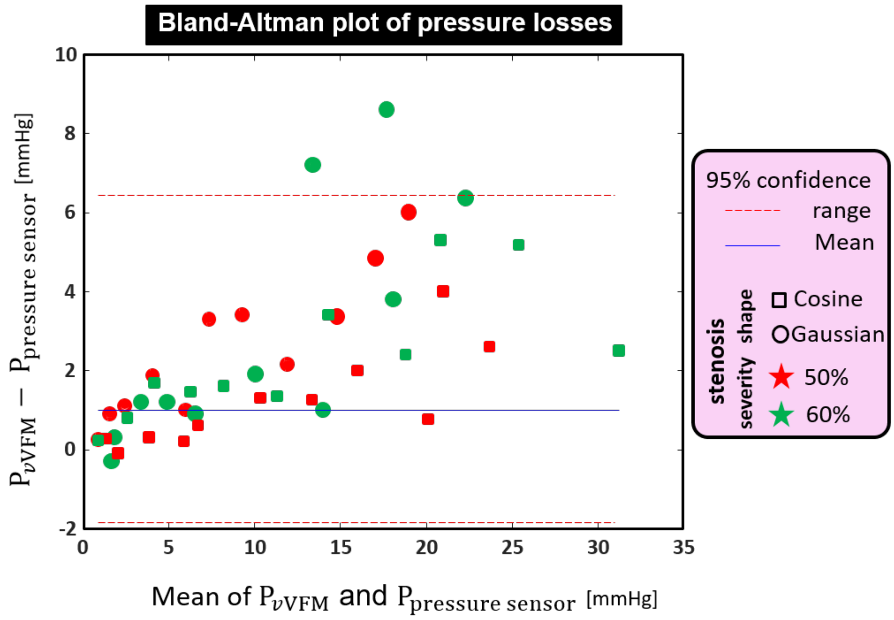

Figure 6.14: Bland-Altman plot illustrating the estimated pressure losses in 44 color Doppler *in vitro* experiments.

0.6 to 3 $m \cdot s^{-1}$ and 0.5 to 3.5 $m \cdot s^{-1}$, respectively. For Gaussian-shaped phantoms with the same degree of stenosis, the maximum velocity within the stenotic region ranged between 0.5 to 2.1 $m \cdot s^{-1}$ and 0.8 to 3.54 $m \cdot s^{-1}$. Upon examination of the velocity vector field images, it is evident that the flow was not perfectly axisymmetric. This lack of symmetry could arise due to small asymmetries in the fabricated phantoms, particularly within the stenotic area. Given the tiny size of the stenotic region, there is a risk of residual matter altering the flow pattern. It is noteworthy that certain experiments proved more challenging than others, largely due to increased flow rates and a greater degree of stenosis severity. For instance, cases with flow rates exceeding 0.5 posed greater challenges. This was particularly true in instances of 60% occlusion, where we observed more turbulence and backflows following the stenosis, especially within Gaussian-shaped geometries. We have summarized some of the less-challenging experiments in Figure 6.19. Conversely, Figure 6.20 provides examples from the experiments where we encountered more challenges during the acquisition and analysis stages.

6.4 Conclusion

In conclusion, our findings from both the CFD analysis and *in vitro* experiments conducted using PIV and color Doppler imaging, confirm the feasibility of estimating turbulent pressure losses in arterial stenoses using clinical color Doppler ultrasound. Despite the limitations arising from experimental uncertainties, such as imperfect straightness and symmetry of stenosis phantoms, wall roughness, turbulence-induced flow instability, and upstream flow not being fully developed, we were still able to obtain accurate and reliable results. The robustness of our methodology effectively mitigates the impact of environmental errors on the results. However, further research and refinement are necessary to enhance the generalizability and applicability of this technique. These aspects and potential directions for future work will be discussed in the ensuing chapter.

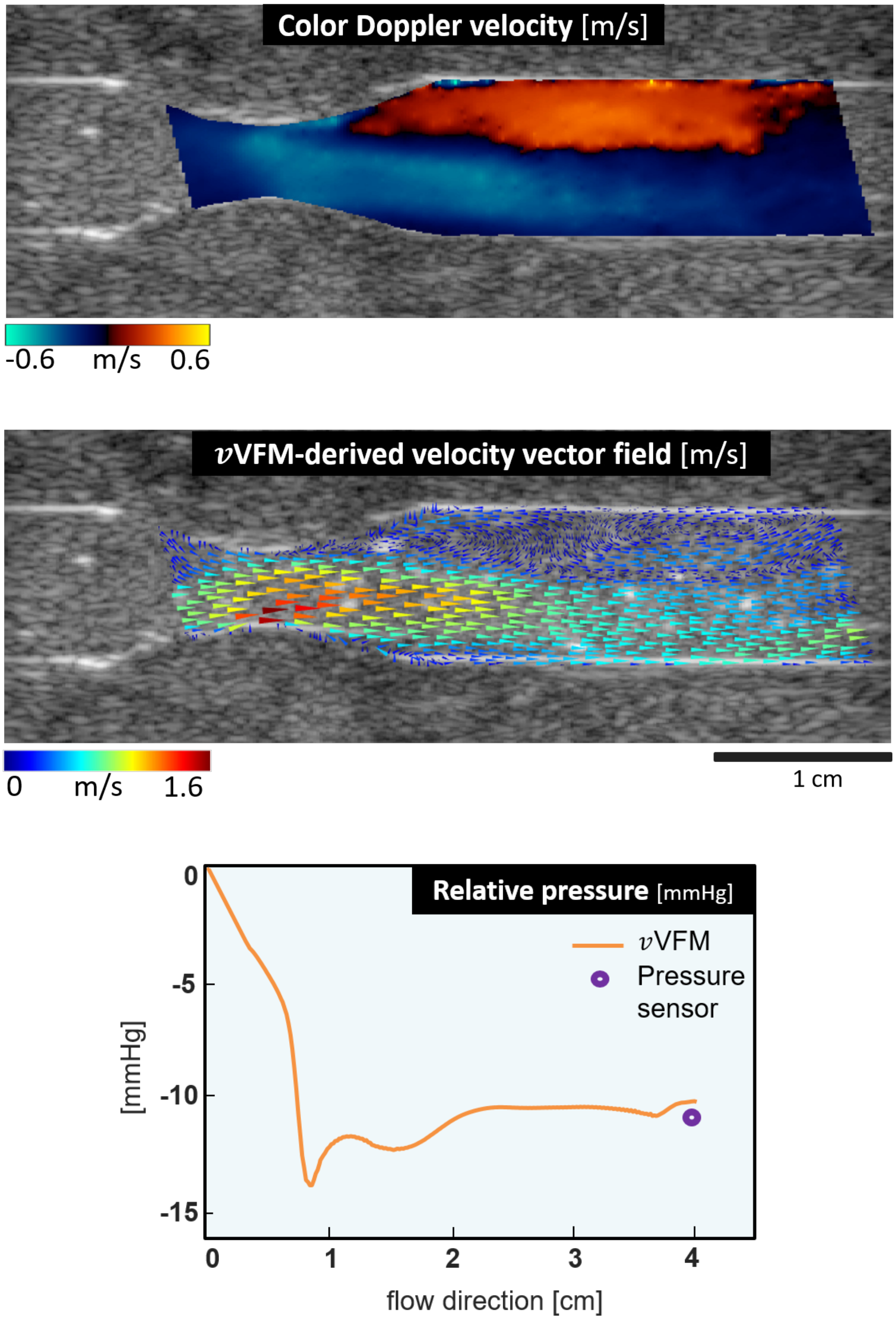

Figure 6.15: From top to bottom: Color Doppler image, *v*VFM-derived velocity vector field, and estimated pressure loss for a Cosine-shaped, 50% occluded carotid stenosis phantom, all obtained at a flow rate of 0.7 $\mathrm{L \cdot min^{-1}}$.

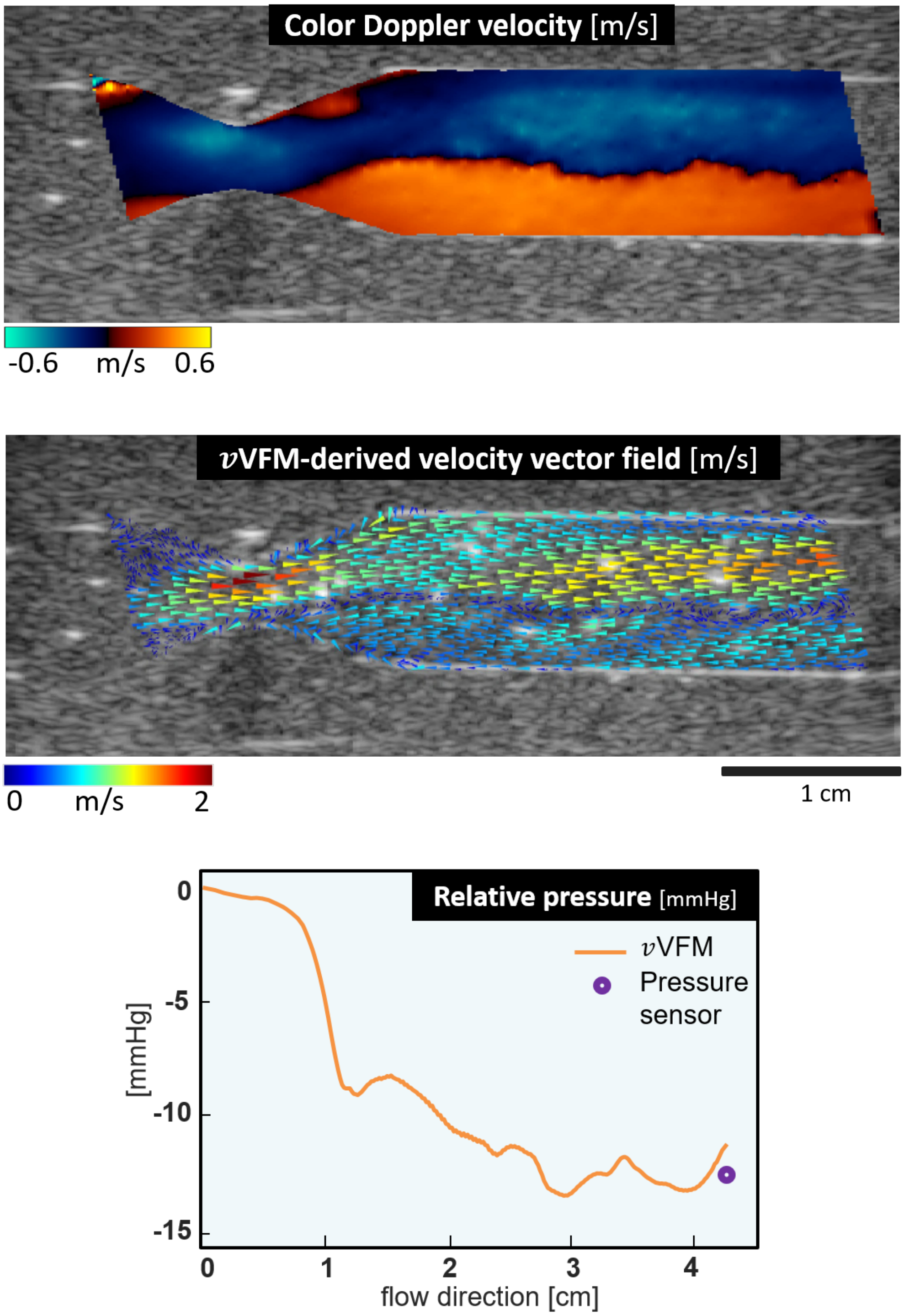

Figure 6.16: From top to bottom: Color Doppler image, vVFM-derived velocity vector field, and estimated pressure loss for a Cosine-shaped, 60% occluded carotid stenosis phantom, all obtained at a flow rate of 0.7 $\mathrm{L \cdot min^{-1}}$.

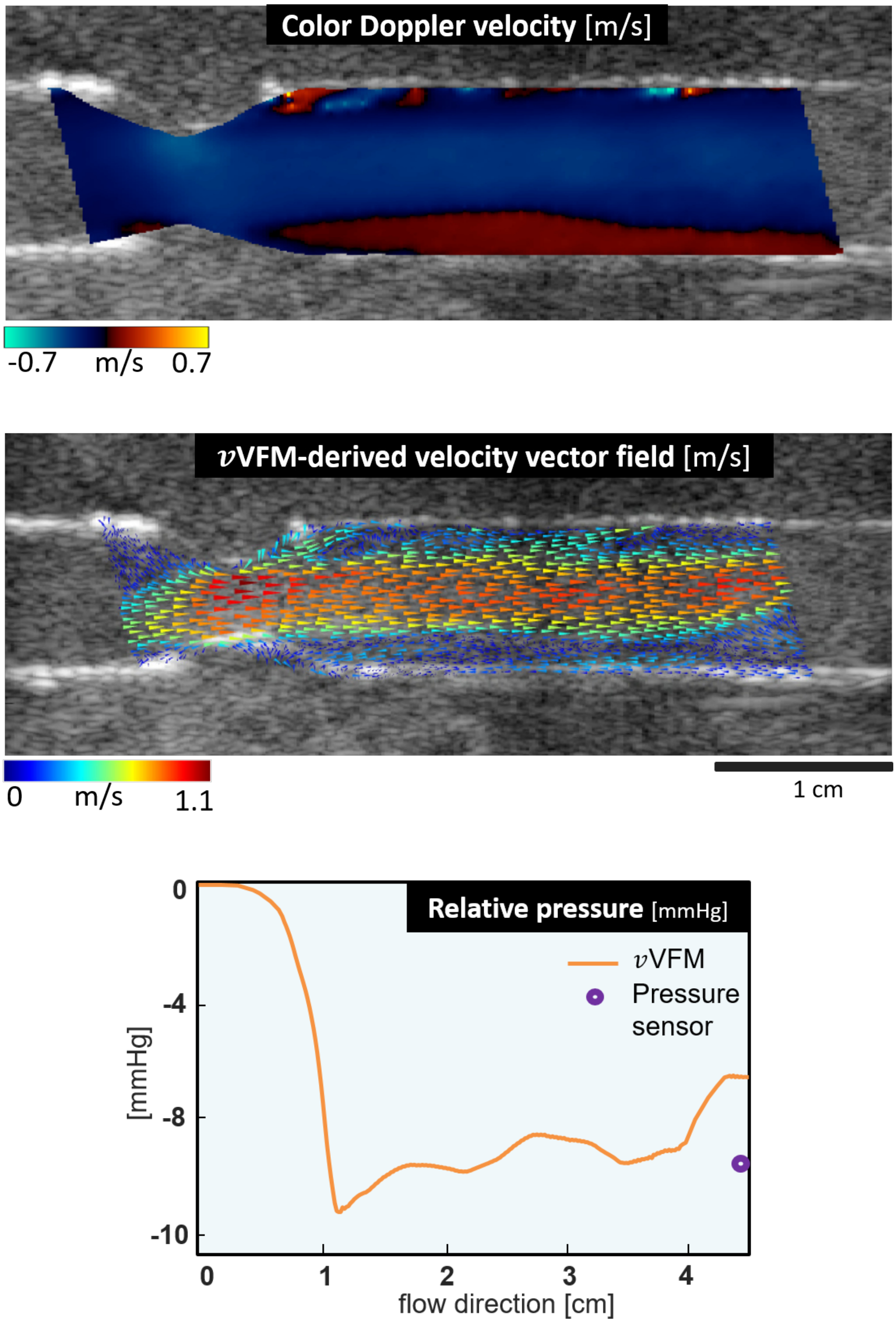

Figure 6.17: From top to bottom: Color Doppler image, vVFM-derived velocity vector field, and estimated pressure loss for a Gaussian-shaped, 50% occluded carotid stenosis phantom, all obtained at a flow rate of 0.7 $\mathrm{L \cdot min^{-1}}$.

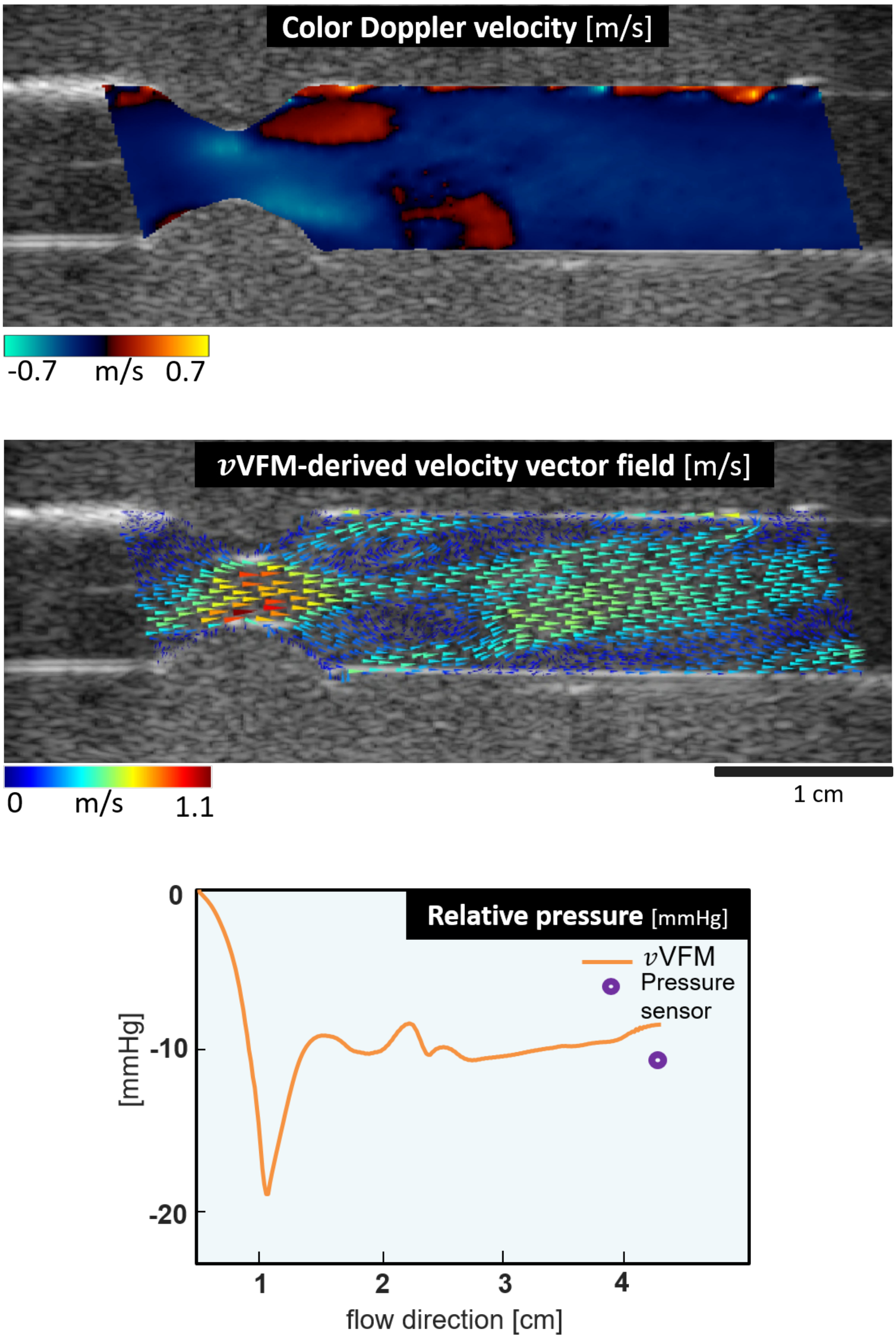

Figure 6.18: From top to bottom: Color Doppler image, vVFM-derived velocity vector field, and estimated pressure loss for a Gaussian-shaped, 60% occluded carotid stenosis phantom, all obtained at a flow rate of 0.7 $\mathrm{L \cdot min^{-1}}$.

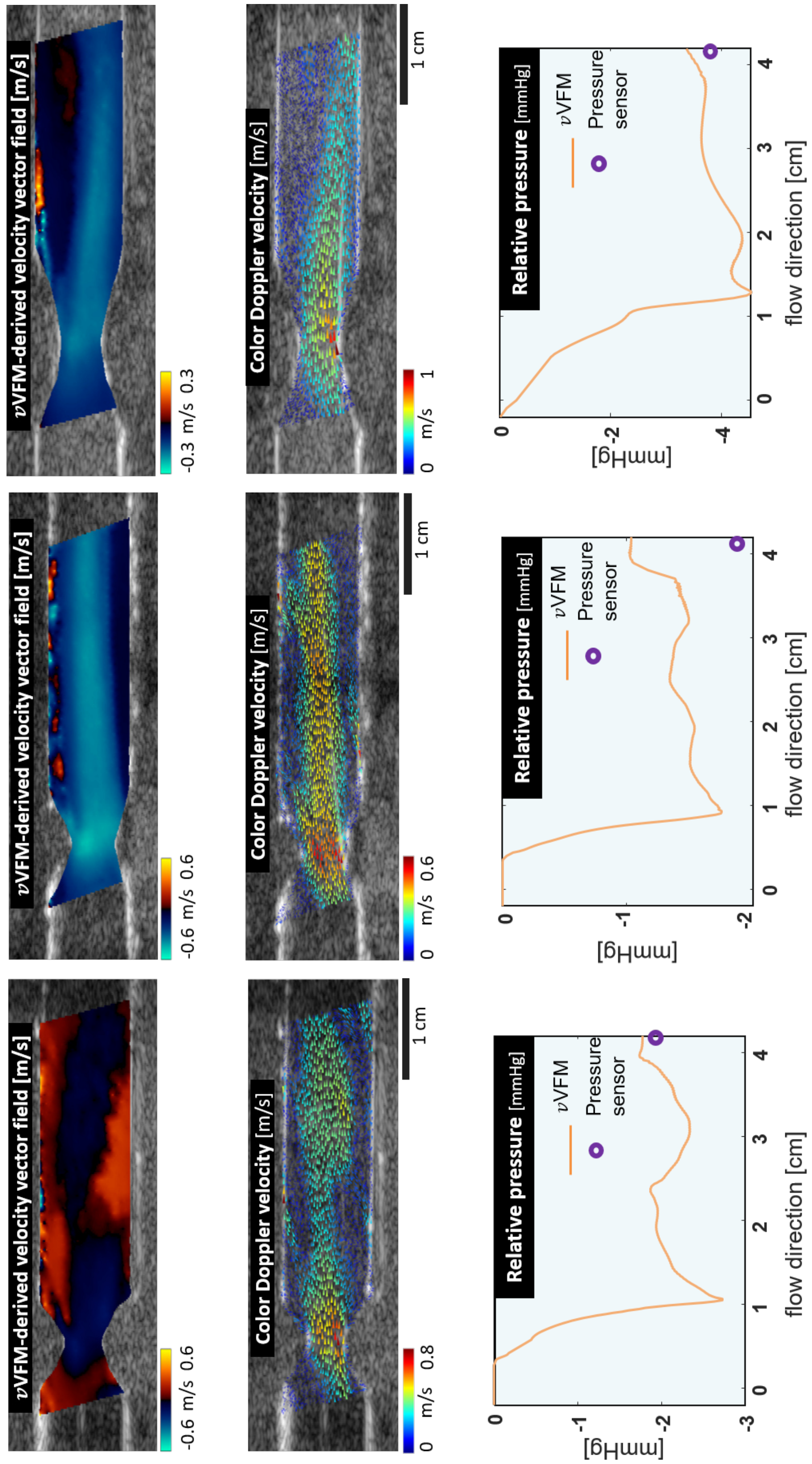

Figure 6.19: *In vitro* color Doppler imaging experiment results in less-challenging cases. The rows present, from top to bottom, Doppler velocity, vVFM-derived velocity vector field, and estimated relative pressure plots. The columns illustrate different stenosis geometries and degree of severity in various flow rates: Gaussian 60%, Gaussian %50, and Cosine %50, with flow rates of 0.2, 0.3, and 0.4 $L \cdot min^{-1}$ from left to right.

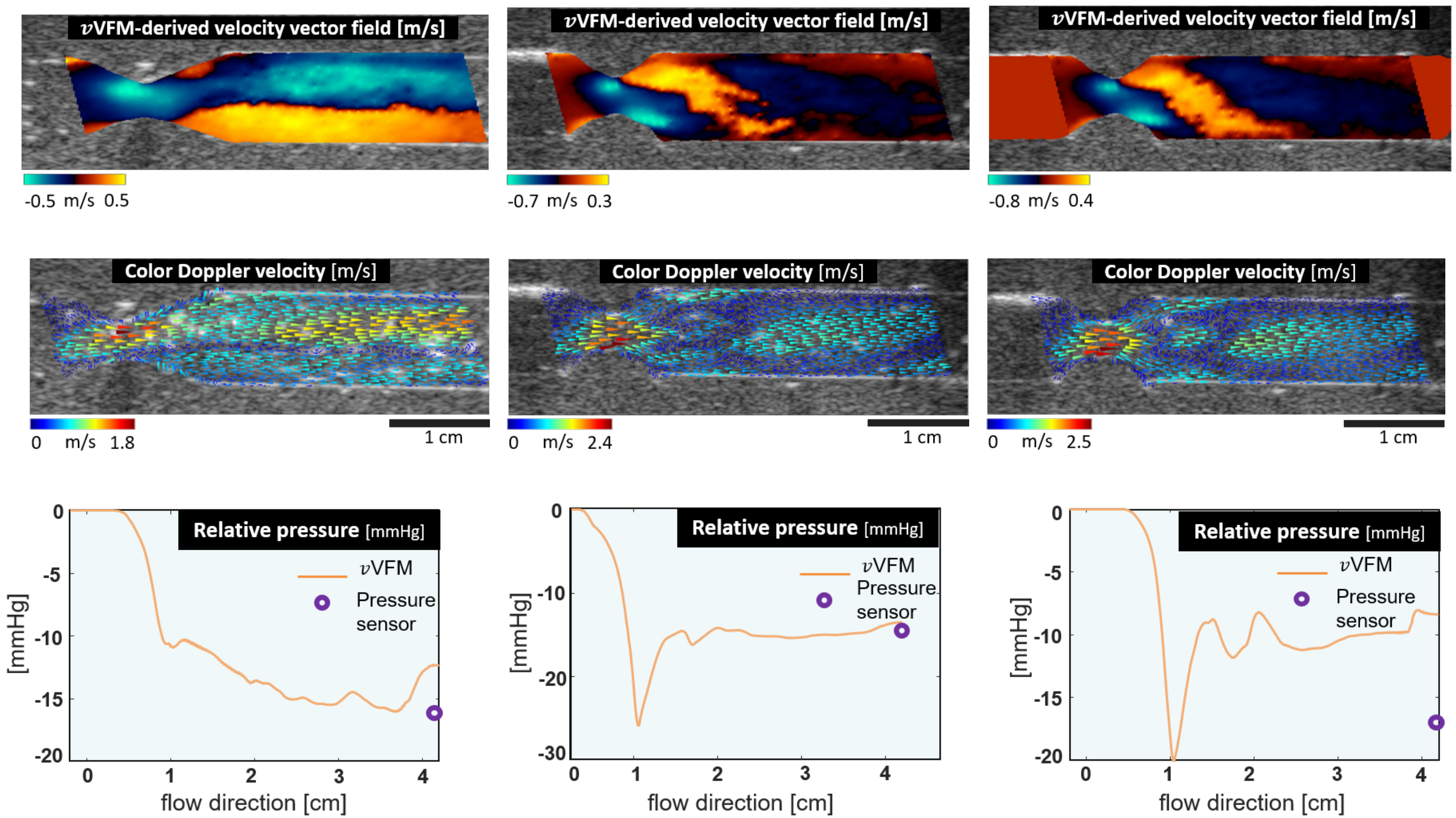

Figure 6.20: *In vitro* color Doppler imaging experiment results in challenging cases. The rows present, from top to bottom, Doppler velocity, vVFM-derived velocity vector field, and estimated relative pressure plots. The columns illustrate different stenosis geometries and degree of severity in various flow rates: Cosine 60%, Gaussian %60, and Gaussian %60, with flow rates of 0.8, 0.8, and 0.9 $\mathrm{L \cdot min^{-1}}$ from left to right.

7

Discussion and Conclusion

This chapter concludes the study's individual aspects, highlighting each contribution. It then presents a comprehensive conclusion covering the entirety of the PhD project. The results obtained for each developed method are discussed, along with their associated limitations. Furthermore, the chapter explores potential directions for future research to build upon this study.

Contents

7.1 Conclusion

In this section, we underscore our role in advancing various aspects of this thesis, resulting in progress within the relevant domain. Additionally, we explore the pertinent state of the art and the studies conducted, which have introduced a range of approaches.

7.1.1 Arterial stenosis assessment using non-invasive pressure loss estimation *(Chapter 1)*

The initial chapter outlines the clinical context of arterial stenosis in detail, highlighting the essential need for estimating pressure loss across mild to moderate arterial stenoses using non-invasive imaging. This approach contrasts with traditional methods that either fail to provide enough information from the impaired stenotic region or are invasive, carrying potential side effects. This estimation is crucial for accurately assessing the severity of arterial stenosis, enabling timely diagnosis and suitable treatment. Consequently, the significance of selecting an effective non-invasive imaging technique and a robust fluid dynamic approach for approximating trans-stenotic pressure loss becomes evident.

7.1.2 Development of 2D vascular vector flow mapping (*v*VFM) technique *(Chapter 2, 4, 5, 6)*

This study extensively reviews blood flow imaging modalities and velocity analysis techniques for estimating blood flow imaging. Between all of them, ultrasound Imaging is often preferred for its ability to provide real-time, instantaneous information on blood flow. Conversely, the chapter further delves into various ultrasound imaging methods such as Multi-beam Doppler, Multi-angle Doppler estimation for Plane-wave VFI, TO, and color-Doppler-based *i*VFM, all of which offer more detailed blood flow information. However, each method comes with its unique set of challenges and limitations. Inspired by *i*VFM, we proposed a *v*VFM to estimate the 2D vascular velocity vector field, under quasi-axisymmetric flow assumption. This method can be used with routine clinical color Doppler scanners. We validated the reliability of this method using *in silico* simulations, through CFD and SIMUS, coupled with color Doppler ultrasound *in vitro* experiments. There was a strong agreement between the estimated results and the provided references for each validity approach, proving that our proposed method is effective for the intended purpose.

7.1.3 Proposed method for estimating trans-stenotic pressure loss using fluid dynamics equations *(Chapter 3, 4, 5, 6)*

Fluid dynamics equations are required for non-invasive pressure estimation from the acquired velocity field. This study explored the application of non-invasive pressure estimation methods, focusing on estimating trans-stenotic pressure loss in stenotic arteries using color Doppler images. A cornerstone of this field is the Navier-Stokes equations, governing fluid flow and describing the conservation of mass and linear momentum. Despite their inherent complexity, these equations are the bedrock for other equations used in pressure estimation like the Poisson and Bernoulli equations. The Poisson pressure equation is often used for pressure drop estimation in arterial stenosis. However, its effectiveness is challenged by the necessity of accurate segmentation of the region of interest, which is not the case in color Doppler ultrasound. On the other hand, the Bernoulli equation has found extensive application in estimating cardiovascular pressure gradients, proving especially useful in investigating high-severity stenosis cases. However, it is criticized for its oversimplified model that overlooks energy dissipation caused by post-stenotic turbulence, a deficiency particularly highlighted when contrasted with results from the finite element model and catheter measurements. The study also delved into the energy loss index method, introduced to better evaluate the severity of aortic stenosis by adjusting for pressure recovery. Similarly, the work-energy equation, despite its limitations of requiring precise segmentation and potential numerical errors, has been utilized in estimating relative pressure differences in aortic vessels.

However, the complexity of fluid dynamics and the limitations of each method led to the pursuit of a combined approach. In conclusion, the quest for a more precise non-invasive pressure estimation method has conducted this study to propose a novel combined approach. Our proposed integrated method combines the Bernoulli and Navier-Stokes equations, offering robust coverage of the physical phenomena at play in intravascular flow. The Bernoulli equation is applied in the upstream section of the stenosis (inlet to *vena contracta*), and the Navier-Stokes equation, accounting for energy dissipation due to frictional forces, is used in the downstream section (*vena contracta* to outlet).

The results obtained from validating the proposed method, both *in silico* using CFD simulations and *in vitro* using PIV and color Doppler ultrasound experiments, confirmed the accurate estimation of trans-stenotic pressure loss. It demonstrates the reliability of the proposed method for estimating pressure loss. Furthermore, this method addresses the limitations of current techniques and potentially offers a more comprehensive understanding of pressure loss in intravascular stenosis.

7.1.4 General conclusion

This study aimed to develop a non-invasive technique to estimate trans-stenotic pressure loss using clinical color Doppler imaging. Its objective was to assess the severity of stenosis accurately for early diagnosis and suitable treatment. Our contribution to this PhD project was twofold:

1. We introduced *v*VFM dedicated to the intravascular flow.
2. Using the recovered velocity vector field, we introduced a method to estimate the pressure loss occurring during the turbulent mixing of diverging flow.

A review of blood flow imaging modalities was conducted, highlighting the advantages and constraints of different techniques. Particular attention was given to *i*VFM through color Doppler ultrasound. Inspired by *i*VFM, this study developed the 2D-*v*VFM technique. The potential of *v*VFM lies in its ability to derive a 2D intravascular vector velocity field from scalar color Doppler velocity. Additionally, the study introduced a method for reliable and non-invasive pressure loss estimation using fluid dynamics equations. Due to the complexity of fluid dynamics and limitations of existing pressure estimation methods, the study proposed an integrated approach, combining the Bernoulli and Navier-Stokes equations. This approach offered a more comprehensive understanding of pressure loss in intravascular stenosis. Our validation strategy comprised *in silico* simulations and *in vitro* experiments, using tools like CFD, SIMUS, PIV, and color Doppler imaging. The validation results confirmed the method's reliability, revealing a solid agreement between estimated and actual values. The technique showed robustness against minor environmental errors and highlighted how flow rate and stenosis severity impact pressure loss values. Therefore, we can conclude that the developed non-invasive method allows us to measure the trans-stenotic pressure loss caused by vascular stenosis. It provides a promising basis for early diagnosis and treatment decision-making.

7.2 Discussion

Obtaining accurate information about the hemodynamic functionality of blood flow presents challenges. This accuracy is essential for clinical interventions in treating arterial stenosis. As a result, research now focuses on non-invasive methods. These methods estimate fundamental fluid mechanics biomarkers using pressure. Our proposed non-invasive technique method aims to evaluate the irreversible pressure loss occurring post-stenosis due to turbulent mixing, leading to energy dissipation due to the frictional forces due to the fluid's viscosity. This approach is particularly pertinent for the mild to moderate stages of stenosis, which are often asymptomatic and challenging to grade in terms of severity (referred to Chapter 1). A non-invasive imaging modality capable of measuring blood velocity was required to facilitate this. Upon obtaining these measurements, we could then apply fluid dynamics equations to describe the relationship between pressure and velocity, thereby estimating the pressure loss in the post-stenotic flow region.

7.2.1 2D Vascular vector flow mapping (*v*VFM): estimating the velocity vector field

The study's most commonly used imaging modality, which estimates trans-stenotic pressure loss, is color Doppler echography. It provides real-time data and is widely available in clinical routine. We understand that both spectral and color Doppler imaging provide a scalar velocity field, representing the projection of the blood velocity components along the ultrasound beam. To estimate the 2D velocity vector field of blood flow from the scalar color Doppler velocity field, we developed a method based on optimization known as *v*VFM, detailed in Chapter 4, enabling the application of fluid dynamics equations to estimate post-stenotic pressure loss. This technique involves a constrained least-squares problem, which we solved using the method of Lagrange multipliers. We derived a full rank, sparse, symmetric linear system by applying a finite-difference discretization of the optimization problem. This system can be solved in a fraction of a second, eliminating the need for extensive computational resources.

The question arises: Why did we choose color Doppler imaging among the various ultrasound modalities available for estimating blood flow velocity? The primary reason is that this modality is the most commonly employed in routine clinical practice. Beyond its accessibility and safety, color Doppler imaging is user-friendly. Even though other vector flow imaging techniques can produce high-resolution blood flow data, they are not regularly implemented in daily clinical practice and are primarily limited to research purposes. This limitation exists because these techniques require the processing of raw ultrasound data (radiofrequency (RF) or inphase/quadrature (IQ) signal), which is not a feature available in standard clinical scanners routinely used in medical centers. Furthermore, scanners that provide raw data often do not meet the necessary health standards for patient application, such as the Verasonics research scanner (Chapter 2).

One **limitation** of our *v*VFM technique is that it differs from other vector flow imaging methods. In our case, we have just one projection of the blood velocity, and our optimization problem primarily estimates these velocities. In contrast, other methods have more comprehensive information due to their use of two velocity projections. Consequently, their 2D velocity field is more accurate and precise. Despite knowing that the resolution of color Doppler imaging is not as high as other techniques, and the provided velocity field is not as complete as other vector flow imaging methods, we opted to use it since our main objective was to ensure the scanner fits within the clinical framework, thus proving useful for healthcare professionals. By doing so, we aimed to provide a quick and reliable diagnostic tool for cases of mild to moderate arterial stenosis and the results obtained have confirmed the technique's reliability (Chapter 6).

On the other hand, transverse oscillation, among the vector flow imaging techniques (refer to section 2.2.4.1), has been implemented in a specialized scanner that meets the necessary standards for patient use. However, one limitation of this device is its limited accessibility in health centers, which we also encountered, as we did not have access to this specific equipment. Nonetheless, our ultimate goal remains integrating a method into routine clinical use.

7.2.2 Estimating post-stenotic pressure loss: Bernoulli & Navier-Stokes

When estimating pressure loss, various fluid dynamics equations can be used (Chapter 3). Most studies using ultrasound modalities for imaging blood flow velocity have employed the Bernoulli equation to calculate pressure loss post-stenosis. The Bernoulli equation, while simple, considers the static-to-dynamic pressure conversion but does not account for energy dissipation due to turbulent mixing post-stenosis. However, this equation suits high-severity stenosis cases, where no pressure recovery is expected post-stenosis. The problem is thus simplified to a 1D scenario, considering the maximum pressure drop in the *vena contracta* as the pressure loss. In such severe cases, the diagnosis is relatively straightforward due to the presence of symptoms and the highly constricted stenosis. It is essential to clarify that our primary focus is evaluating challenging stenoses. Our study aims to estimate the pressure loss in mild to moderate arterial stenosis using conventional clinical color Doppler, thus facilitating an earlier diagnosis.

Since the Bernoulli equation accounts for the static-to-dynamic pressure conversion, it is suitable for the upstream of the stenosis, where the flow can be considered non-dissipative and we do not experience any pressure loss due to turbulence mixing and frictional forces resulting from fluid viscosity. The simplicity and ease of this method encourage us to select it for estimating pressure from the upstream (inlet) to the *vena contracta*, where no energy dissipation occurs. Thus, we could estimate the maximum pressure drop, which theoretically occurs at the maximum jet velocity in the *vena contracta*. However, another equation considering this dissipation is necessary for the downstream of the stenosis, where we experience energy dissipation. We selected the Navier-Stokes equation for this purpose. With this combined method, we could fully account for the physical phenomena inside an arterial stenosis and estimate the pressure loss in the post-stenotic area (Chapter 4).

Conversely, other fluid dynamics equations, such as the Poisson and Work-energy equations, were not optimal for our objectives. These equations require precise segmentation of the studied arterial stenosis area to be solved accurately, which is not achievable with clinical color Doppler due to its limited resolution. Using the Navier-Stokes equation alone also posed numerical problems due to second-order derivatives, particularly in the stenosis region. It resulted in underestimations of the pressure losses when compared to reference values. Using the Bernoulli equation, combined with Navier-Stokes, compensated for these pressure losses. It was accomplished by initiating the Navier-Stokes equation from the maximum pressure drop occurring in the stenosis section, which led to the desired pressure loss results during the validation processes (Chapter 6). In addition, the combined proposed method was formulated using small-sized matrix systems through finite-difference discretization. As a result, the computation time for these operations was measured in fractions of a second, making the method well-suited for clinical practice.

Additionally, from the perspective of pressure loss results, we noted that the simulations seem to cap pressure losses around 13 or 14 mmHg, whereas the *in vitro* experiments yielded data up to 30 mmHg. We would need to conduct simulations at higher flow rates to align these results. However, we could not accomplish this due to time constraints during this PhD project. Despite the disparity in these results, we believe it does not diminish the value or intent of our findings.

Comparing our estimated post-stenotic pressure loss results with other studies in this context, we found that none of them estimated pressure loss values effectively. The study of Nguyen *et al.* [76] did not include stenosis in their phantom, and Haslund *et al*. [77] work only estimated the conversion from static to dynamic pressure upstream of the stenosis. Also, in the study of Olesen *et al*. [13], they employed the Bernoulli equation, which does not account for energy dissipation due to frictional forces, rendering it inadequate for estimating post-stenotic pressure losses. Even considering these methodologies, their results show minor pressure drops, approximately 1 mmHg.

7.2.3 Methodology and implementation

As detailed in Chapter 5, to validate this dual-purpose non-invasive method for estimating pressure loss from clinical color Doppler images, we conducted *in silico* simulations using CFD and SIMUS on carotid stenosis models. Additionally, we performed *in vitro* experiments using PIV and color Doppler imaging on carotid stenosis phantoms under constant flow conditions. We observed a substantial agreement between the estimated results and the reference data for each validation step. This validation endorsed our proposed non-invasive method. Our findings highlight that, in contrast to other ultrasound studies that evaluated static-to-dynamic pressure conversions only, it is possible to estimate turbulent pressure losses in arterial stenoses using conventional color Doppler ultrasound.

From the results of both PIV and 2D-*v*VFM-derived velocity vector fields, a **limitation** that we observed was that the flow was not axisymmetric in post-*vena contracta*. This observation originates from the fact that the phantoms we used were not ideally axisymmetric. The fabrication of stenotic phantoms, especially the smaller stenosis parts, is a delicate process. Sometimes, due to their small size, these areas are not easily accessible, making it challenging to control the fabrication process and possibly leaving some residues behind, leading to the observed asymmetry. Despite these **experimental challenges**, such as imperfectly straight stenosis phantoms, wall roughness, flow instability due to turbulence, and undeveloped upstream flow, our proposed method could accurately estimate pressure losses. It suggests that our approach can also work effectively in non-axisymmetric flows. We also noticed that changes in the degree of stenosis have a more significant impact on the pressure loss values than changes in its shape. As the flow rate increased, the accuracy of our method for pressure loss estimation decreased. It was evident as the discrepancies between the estimated pressure losses and the pressure sensor values (gold standard) increased. This observation was expected as we captured a 2D axisymmetric velocity field from a 3D phenomenon, thereby losing some data. As the flow rate increases, the turbulence in the post-stenosis divergent region intensifies. However, when velocity is smoothed, it decreases spatial resolution, potentially resulting in an underestimation of the spatial gradient.

Additional **limitations** surfaced during the *in vitro* validation experiments. We could not maintain a single experimental setup for both PIV and color Doppler tests, which meant we could not maintain identical conditions regarding flow rate and pattern. This discrepancy likely affected our results, leading to a larger variance between the two sets of findings. Furthermore, introducing a pressure wire into the flow stream within the phantoms could have altered the flow pattern, inducing turbulence or causing the flow within the phantom to become asymmetrical.

It is essential to clarify certain aspects of this study. When comparing the *in silico* and *in vitro* velocity results, we noticed that even though the experimental conditions were similar to those in the simulations, they did not match exactly. This resemblance is only qualitative. Our goal was not to validate our *in vitro* velocity fields against the simulation results or vice versa but to validate the pressure loss estimates. Each methodology (*in vitro* or *in silico*) provided its own reference (pressure guides for *in vitro*, and k-ε CFD model for *in silico*). As such, a direct comparison between two validation method results unnecessary. We must also note that achieving axisymmetric flow during the *in vitro* experiments was challenging, if not impossible, in contrast to *in silico* models. Furthermore, slight differences existed in the flow rates and geometry, attributable to **experimental uncertainties** (*in vitro* model adapted for PIV and ultrasound). Consequently, any alignment attempt between *in vitro* and *in silico* under our conditions was bound to be unsuccessful.

The other **limitation** of the *in vitro* experiments was that we did not exceed a 60% stenosis level due to the logistical challenges of working with more severe stenoses (potential for setup destabilization, etc.). To accomplish this, substantial enhancements would have been required in the design and fabrication of our setup. Furthermore, it is essential to mention that our methodology may not be necessary for diagnosing severe stenoses, which display prominent symptoms and necessitate treatment. However, our approach could apply to moderate stenoses, where we believe hemodynamic indices could offer clinical value over traditional geometric ones. As such, the primary aim of our study was to estimate the pressure loss in mild to moderate arterial stenosis using conventional clinical color Doppler imaging, thereby aiding earlier diagnosis.

7.3 Perspectives

7.3.1 Flow and geometry condition toward a physiological situation

This study only tested our non-invasive method for estimating trans-stenotic pressure losses in nearly axisymmetric, steady flow conditions. However, we know that blood circulation within the body occurs in a pulsatile manner, in sync with cardiac cycles, and the stenosis is asymmetric. The developed equations must first be adapted to this flow rate type to incorporate pulsatile flow into our system. One approach would be to conduct temporal averaging over one or more cardiac cycles. It would effectively remove the local acceleration term from each equation, representing the velocity change over time. As a result, the average velocity and average squared velocity could be inserted into the Bernoulli and Navier-Stokes equations, enabling us to estimate the average post-stenotic pressure losses, a suitable and sufficient biomarker for physicians in clinical decision-making. Therefore, As part of future perspectives for our study, we aim to extend the non-invasive method to accommodate both asymmetrical and pulsatile stenotic flow phantoms. Furthermore, the effect of misalignment between the ultrasound probe and the flow axis should be considered during *in vitro* experiments.

In addition, for the sake of simplicity, we focused only on the common carotid artery rather than considering the complete carotid bifurcation. We neglected factors such as branching, tortuosity, and the nature of the stenotic plaque itself, which we assumed to be symmetric when it is often asymmetric in reality. All these factors can significantly influence the flow structure within the phantom. Moreover, both the *in vitro* stenosis model used in experiments and its corresponding *in silico* model for CFD simulations featured rigid walls instead of compliant ones. Consequently, our results may not fully mirror the realistic physiological conditions during a cardiac cycle. However, unlike the systemic compliance of the circulatory system, which directly impacts the flow and, subsequently, post-stenotic pressure loss, the local effect of this parameter within the small region imaged by color Doppler is negligible. In future work, each of these conditions could be considered and integrated better to reflect the actual physiological geometry of the situation.

7.3.2 Adapting the method for 3D

Our method has been developed for 2D axisymmetric geometry, whereas arterial stenosis is a complex 3D phenomenon. Looking to the future, one potential solution would be to update the equations to 3D and use volume ultrasound imaging with a matrix array. The next step would be to adapt this method to handle asymmetric flows.

7.3.3 Clinical feasibility of the method through *in vivo* experiment

After expanding the method to accommodate pulsatile and asymmetric flow, and once the new conditions are validated both *in silico* and *in vitro*, the feasibility of this technique should be explored in a clinical setting through *in vivo* trials. It is important to note that the phantom datasets used in this study represent flow in idealized arterial stenosis under controlled conditions. In a real-world clinical setting, data acquisition errors may reduce the accuracy of the data, particularly with catheter-based measurements serving as reference pressure, which may highlight *in vivo* factors not previously considered. However, collecting such data would be challenging, mainly due to disturbances in the flow induced by the catheter.

Abstract

Arterial stenosis refers to the narrowing or constriction of the arteries in the blood circulatory system, which obstructs normal blood flow. Such narrowing can lead to diminished blood flow, jeopardized oxygen supply, and potential complications like ischemia, tissue damage, or even complete blockage in severe cases. Timely diagnosis and appropriate treatment are crucial to manage arterial stenosis, prevent further complications, and maintain optimal blood flow.

Traditional approaches to assess arterial stenosis severity involve scanning the impaired region via vascular ultrasound, utilizing specific geometric criteria to grade severity. However, these geometric criteria, which are tied to the geometrical parameters of the stenosis, do not provide comprehensive information about its hemodynamic functionality, that could offer more detailed insights into stenotic blood flow. One potential solution involves measuring intravascular blood pressure loss between the inlet and outlet of a stenosis caused by post-stenotic turbulence and energy dissipation due to frictional forces within the fluid. Conventionally, this assessment is performed by catheterization, an invasive procedure with a risk of complications. As such, non-invasive blood flow imaging methods are often preferred to mitigate costs and potential side effects. Color Doppler ultrasound imaging is a non-invasive imaging modality that facilitates the study of intravascular flow. Its affordability and portability, combined with its ability to deliver real-time information about blood flow, make it an ideal choice for studying intravascular flow. However, it is essential to remember that the Doppler mode of echography provides a projection of blood velocity components along the ultrasound beam axis. By obtaining the velocity vector field and employing fluid dynamics equations, trans-stenotic pressure loss can be measured.

The study presented in this thesis aims to develop and examine the feasibility and applicability of a non-invasive technique utilizing clinical color Doppler imaging to estimate trans-stenotic pressure loss in mild to moderate cases of carotid artery stenosis. Such estimation will aid in assessing stenosis severity, allowing for earlier diagnosis. Our two-fold contribution to this study includes developing a vascular vector flow mapping (vVFM) technique for estimating the two-dimensional velocity vector field from the color Doppler scalar field by solving a constrained least squares problem using the Lagrange multipliers method. These constraints are related to fluid dynamics' basic principles: mass conservation and free-slip boundary conditions. The second part of our contribution involves proposing a method for estimating trans-stenotic pressure losses based on fluid dynamics equations, where we suggest a combination of using the Bernoulli equation (upstream of the stenosis) and the Navier-Stokes equation (downstream of the stenosis). This non-invasive method was validated *in silico* via computational fluid dynamics and ultrasound simulations, and *in vitro* through particle image velocimetry and color Doppler ultrasound experiments on carotid stenosis models and phantoms in constant flows.

This thesis demonstrates the reliability and feasibility of the proposed non-invasive method for trans-stenotic pressure loss estimation using clinical color Doppler.

Keywords: Arterial stenosis, pressure loss, color Doppler, vector flow imaging, constrained optimization.

Résumé

La sténose artérielle désigne le rétrécissement des artères du système circulatoire, obstruant le flux sanguin normal. Un tel rétrécissement conduit généralement à une diminution de l'approvisionnement en oxygène, et à des complications potentielles pouvant aller jusqu'à l'ischémie dans les cas les plus graves. Un diagnostic précoce et un traitement approprié sont essentiels pour prendre en charge la sténose artérielle, prévenir d'autres complications potentielles et maintenir un flux sanguin optimal. Les approches traditionnelles pour évaluer la sévérité d'une sténose consistent à imager la région en question par échographie, afin d'évaluer sa gravité par des critères géométriques spécifiques issus de l'imagerie. Cependant, ces critères fournissent une information partielle et ignorent les aspects hémodynamiques du flux qui pourraient offrir des informations complémentaires sur la sténose. Une solution consiste à mesurer la chute de pression sanguine intravasculaire entre l'entrée et la sortie d'une sténose. Cette chute de pression est causée par la turbulence post-sténotique et la dissipation d'énergie due aux forces de friction au sein du fluide. Traditionnellement, cette mesure est effectuée par cathéter intravasculaire, une procédure invasive. Cependant, des méthodes non invasives utilisant l'imagerie du flux sanguin sont souvent préférées pour réduire les coûts et les effets secondaires potentiels. L'imagerie par échographie Doppler couleur est une modalité d'imagerie non invasive facilitant l'étude du flux intravasculaire. Sa portabilité combinée à sa capacité à fournir des informations en temps réel sur le flux sanguin, en fait un choix idéal pour l'étude du flux intravasculaire. Cependant, il est essentiel de rappeler que le mode Doppler couleur fournit uniquement une projection de la vitesse sanguine selon l'axe du faisceau ultrasonore. En obtenant le champ vectoriel de la vitesse et en utilisant les équations de la dynamique des fluides, la chute de pression trans-sténotique pourrait être mesurée. L'objectif de cette thèse est de développer et d'examiner la faisabilité d'une technique non invasive utilisant l'imagerie Doppler couleur clinique pour estimer la perte de pression trans-sténotique dans les cas de sténose de l'artère carotide de légère à modérée, en vue d'un diagnostic plus précoce de la gravité de la sténose. La contribution à cette étude est double. Premièrement, une technique du vascular vector flow mapping (*v*VFM) ou cartographie vectorielle du flux vasculaire en français, a été développée afin d'estimer le champ vectoriel des vitesses à partir du champ scalaire Doppler couleur. Ceci est réalisé en minimisant un problème au sens des moindres carrés, tout en utilisant la méthode des multiplicateurs de Lagrange. Deux contraintes liées aux principes de base de la dynamique des fluides sont utilisées: la conservation de la masse et les conditions aux limites de non-glissement. La deuxième contribution est une méthode d'estimation des pertes de pression basées sur les équations de la dynamique des fluides, où nous suggérons une combinaison de l'utilisation de l'équation de Bernoulli et de l'équation de Navier-Stokes. Cette méthode a été validée *in silico* via la dynamique des fluides computationnelle et des simulations d'ultrasons, et *in vitro* à travers la vélocimétrie par images de particules et des expériences d'échographie Doppler couleur sur des modèles de sténose carotide et des fantômes à débits constants. Ce travail de thèse démontre la fiabilité et la faisabilité d'une méthode complète non invasive pour l'estimation de la perte de pression trans-sténotique en utilisant le Doppler couleur clinique.

Mots-clés: Sténose artérielle, perte de pression, Doppler couleur, imagerie de flux vectoriel, optimisation contrainte.

Contexte Médical

Le système circulatoire humain est un réseau complexe d'organes, de vaisseaux et de fluides qui joue un rôle crucial dans le transport de l'oxygène, des nutriments vers les tissus et les organes du corps [1] et l'évacuation de leurs déchets. Au centre de ce système se trouve le cœur, qui pompe le sang à travers le corps par l'intermédiaire des artères, des veines et des capillaires. Les artères, les vaisseaux qui transportent le sang oxygéné depuis le cœur, se divisent en deux types principaux : systémiques et pulmonaires. Les artères systémiques fournissent du sang oxygéné aux tissus et organes du corps, tandis que les artères pulmonaires transportent le sang désoxygéné vers les poumons pour l'oxygénation [2].

La sténose artérielle fait référence au rétrécissement ou à la constriction des artères en raison de l'accumulation de plaque sur leurs parois internes. Cette condition restreint ou obstrue le flux sanguin normal et se produit dans diverses artères du corps. Lorsqu'une artère se rétrécit, cela entraîne une diminution du flux sanguin, un apport en oxygène compromis et des complications potentielles telles que des lésions tissulaires, une ischémie ou même l'occlusion complète dans les cas graves [3].

Une artère importante dans le corps est l'artère carotide. Elle fournit du sang oxygéné au cerveau. Les blocages ou perturbations du flux sanguin à travers cette artère ont de graves conséquences sur la santé, en particulier des accidents vasculaires cérébraux ou d'autres troubles neurologiques. La sténose carotidienne est caractérisée par le rétrécissement d'une ou des deux artères carotides, généralement causée par l'accumulation de plaques d'athérome à l'intérieur de la paroi du vaisseau. Cette maladie entraîne une diminution du flux sanguin vers le cerveau et un risque accru d'accident vasculaire cérébral. Il existe plusieurs méthodes de traitement de la sténose carotidienne, qui dépendent de la gravité de la blockage et du patient [6]. Les options de traitement comprennent les changements de mode de vie, les médicaments, la pose de stent sur la carotide et l'endarterectomie de la carotide. Pour déterminer le traitement optimal parmi ces différentes méthodes, un diagnostic précis est nécessaire pour évaluer la sévérité de la sténose. Cela implique généralement une combinaison d'examen physique, d'historique médicale et de techniques d'imagerie pour visualiser les carotides et déterminer le degré d'occlusion [8].

La méthode conventionnelle d'évaluation de la sténose artérielle nécessite de scanner la région affectée par l'échographie, puis d'utiliser des critères géométriques pour calculer la sévérité [9]. Cependant, ces informations géométriques fournissent une perception limitée de la fonctionnalité hémodynamique du flux sanguin. Un biomarqueur classique, utilisé à cette fin, est la mesure de la perte de pression entre l'entrée et la sortie de la sténose [13, 15]. Cette perte de pression est principalement causée par les turbulences qui se produisent après la sténose, entraînant une dissipation d'énergie due aux forces de frottement à l'intérieur du fluide [18]. La manière conventionnelle de mesurer la perte de pression intravasculaire est l'utilisation d'un cathéter intravasculaire [14]. C'est une procédure médicale invasive coûteux et qui a des effets secondaires [20]. Par conséquent, les méthodes non-invasives utilisant l'imagerie sont à privilégier.

Dans ce contexte, l'imagerie clinique Doppler couleur est un choix approprié parmi les modalités d'imagerie disponibles. Elle est largement accessible, compatible avec les pratiques cliniques courantes, et offre une facilité d'utilisation et une mise en œuvre rapide. De plus, elle fournit des informations en temps réel sur le flux.

L'objectif de cette étude est de développer et d'examiner la faisabilité d'une technique non-invasive basée sur l'imagerie clinique Doppler couleur, pour estimer la perte de pression trans-sténotique dans les cas légers à modérés de sténose carotidienne. Cette évaluation de la gravité de la sténose facilitera et permettra un diagnostic plus précoce en vue d'une prise en charge optimale.

État de l'Art des Techniques d'Imagerie de la Vitesse Sanguine

L'imagerie par résonance magnétique (IRM) est une technique d'imagerie médicale non-invasive qui utilise le principe de la résonance magnétique nucléaire (RMN) pour visualiser les structures internes du corps humain. Elle s'appuie sur le comportement des atomes d'hydrogène dans un champ magnétique [21]. Le processus consiste à aligner les moments magnétiques des protons d'hydrogène avec un fort champ magnétique externe, puis à appliquer une impulsion radiofréquence pour induire une résonance. Lorsque l'impulsion est désactivée, les protons émettent des signaux électromagnétiques qui sont détectés et traités pour créer des images détaillées du corps. L'IRM en contraste de phase (IRM-CP) est une application spécifique de l'IRM qui se concentre sur la mesure du mouvement et des fluides, en particulier celui sanguin. Elle utilise les déphasages induits par le flux sanguin pour déterminer la vitesse à l'intérieur des vaisseaux. L'IRM-CP applique un gradient au champ magnétique pendant l'acquisition du signal, ce qui provoque un déphasage proportionnel à la vitesse du sang. Ce déphasage est converti en mesures de vitesse, quantifiant le flux. L'IRM-CP est réalisée en utilisant des séquences 2D ou 3D pour capturer des images tout au long du cycle cardiaque. Elles sont ensuite post-traitées pour calculer la vitesse et le débit dans les vaisseaux. Bien que l'IRM-CP soit un outil de diagnostic précieux, elle a des limites. Les IRM sont coûteuses, moins accessibles et non portables, ce qui conduit à de longues listes d'attente pour les patients. Le temps d'examen prolongé, le bruit et l'espace confiné du scanner IRM sont aussi inconfortables et provoquent de l'anxiété ou de la claustrophobie. De plus, certains types d'implants ou de dispositifs médicaux peuvent provoquer des interférences dues au champ magnétique.

L'échographie, en revanche, est une modalité d'imagerie non-invasive utilisant les ondes sonores pour produire des images détaillées des structures internes. Les ondes ultrasonores sont émises par une sonde contenant une céramique piézoélectrique vibrante et sont détectées comme des échos après avoir interagi avec les tissus ou les organes du corps. Ces échos sont convertis en signaux électriques, et traités pour créer des images. L'échographie nécessite l'application d'un gel sur la peau du patient pour éliminer les poches d'air et améliorer la qualité de l'image. Différents types de sondes d'échographie, tels que les sondes linéaires, convexes et cardiaques, sont disponibles pour répondre aux divers besoins cliniques [23]. Les sondes linéaires sont généralement utilisées pour l'imagerie des vaisseaux superficiels, tandis que les sondes convexes offrent un champ de vision plus large pour les tissus et organes plus profonds. Les sondes cardiaques sont petites et de forme carrée, permettant l'imagerie des quatre chambres du cœur à travers les côtes. L'émission d'ultrasons implique l'activation d'éléments piézoélectriques avec des détails spécifiques afin de concentrer l'énergie dans une zone étroite. Les ondes émises convergent au point focal avant de diverger. La réception des échos implique la vibration des éléments piézoélectriques en réponse aux échos sonores. Ces vibrations sont converties en un signal électrique RF, qui est retardé et sommé pour obtenir une focalisation dynamique et une réception optimale. La formation d'images en échographie implique le traitement des signaux RF pour créer des images en mode B en niveaux de gris, qui représentent les structures internes du corps. Les signaux Doppler sont générés pour détecter le flux sanguin. Plusieurs acquisitions sont effectuées pour balayer la région d'intérêt, et les images partielles sont intégrées pour créer l'image complète. L'image résultante est affichée sur le système échographique et interprétée par les professionnels de la santé.

Les deux techniques utilisées pour l'imagerie du flux sanguin par ultrasons sont blood speckle tracking (BST) et echo particle image velocimetry (eco-PIV). La technique BST visualise et suit le mouvement du sang au cours de l'acquisition. Le speckle se réfère au motif granulaire observé dans les images en mode B non filtrées, causé par les interférences des ondes sonores provenant de diffuseurs tels que les tissus, les organes ou le sang. BST utilise les motifs de speckle pour analyser et suivre le flux sanguin [26]. Un filtre passe-haut est utilisé pour supprimer les signaux provenant de diffuseurs stationnaires [27]. Une fois le speckle du sang rehaussé, une technique de "block matching" est employée pour estimer le champ de vitesse vectoriel en analysant les images consécutives. Cette technique divise chaque image en petites régions et trouve la meilleure correspondance du trace de speckle dans les images suivantes [28]. Enfin, la vitesse moyenne est calculée. Le BST est principalement utilisé dans la recherche clinique en raison de sa dépendance à l'égard des données brutes ultrasonores, qui ne sont généralement pas disponibles à partir des scanners cliniques. L'echo-PIV est basée sur la technique de particle image velocimetry (PIV) utilisée en dynamique des fluides. Elle utilise des agents de contraste ultrasonores sous forme de microbulles injectées dans la circulation sanguine pour améliorer le contraste de l'image [26, 31]. De la même manière que le BST, l'echo-PIV applique une correspondance de blocs à l'aide de la corrélation croisée normalisée pour estimer le champ vectoriel de vitesse. Une régularisation ou un lissage peut être appliqué pour éliminer les valeurs aberrantes. L'echo-PIV est principalement utilisée dans la recherche pour étudier la dynamique du flux sanguin à l'intérieur du ventricule gauche du cœur.

Le mode Doppler en imagerie ultrasonore utilise l'effet Doppler pour détecter et analyser la vitesse et la direction du flux sanguin. Les ondes sonores émises sont rétrodiffusées par les globules rouges en mouvement et le système mesure la fréquence et le décalage de phase des échos. Le mode Doppler est utilisé de deux façons : Doppler pulsé et Doppler couleur. Le Doppler pulsé est une technique qui permet aux utilisateurs de sélectionner un volume d'échantillonnage en fonction de l'image en mode B. Il utilise des impulsions successives avec une fréquence de répétition d'impulsions (pulse repetition frequency (PRF) en anglais) pour éviter la confusion des échos. La transformée de Fourier est utilisée pour calculer la distribution de la vitesse à l'intérieur du volume d'échantillonnage sélectionné. Le Doppler pulsé est susceptible un repliement spectral (aliasing), qui se produit lorsque la fréquence Doppler dépasse la moitié de la PRF. L'aliasing conduit à une sous-estimation et à une inversion de la direction du flux. La vitesse de Nyquist spécifie la vitesse maximale qui peut être mesurée avec précision sans aliasing [23]. Le mode Doppler couleur permet la visualisation en temps réel des flux sanguins sous forme d'image couleur. Il fournit des informations relatives à la vitesse pour une région d'intérêt en superposant des informations de flux codées en couleur sur une image standard en niveaux de gris. Le bleu indique des flux s'éloignant de la sonde, tandis que le rouge indique des flux allant dans la direction opposée. L'intensité de la couleur correspond à la vitesse du flux sanguin, les couleurs claires représentant des vitesses plus élevées et les couleurs sombres des vitesses plus faibles [23]. Le mode Doppler couleur est couramment utilisé en pratique clinique pour évaluer les maladies vasculaires et cardiovasculaires en raison de son accessibilité et de ses capacités de visualisation en temps réel. Pour analyser de manière exhaustive le flux cardiovasculaire, il est nécessaire d'extraire le champ vectoriel des vitesses à partir des images Doppler couleur. Plusieurs techniques ont été proposées pour générer ces champs vectoriel, notamment en imagerie dite ultra-rapide. Les oscillations transverses (OT) est une techniques qui génère une nouvelle image qui introduit des informations de phase dans la direction latérale, permettant d'estimer la composante transverse de la vitesse [39]. Cependant, les OT nécessitent des scanners spécialisés qui ne sont pas utilisés en routine clinique. Les méthodes de cartographie du flux vectoriel basées sur le Doppler couleur impliquent un post-traitement des images Doppler couleur. Ces méthodes utilisent des contraintes physiques et des équations de continuité pour estimer les champs vectoriels des vitesses [40]. Ils ont été appliqués au ventricule gauche (intraventricular vector flow mapping (*i*VFM)) [41,42] et à l'aorte abdominale [43] pour construire des champs de vitesse résolus dans le temps. Ces techniques impliquent la résolution de problèmes d'optimisation avec l'application de contraintes pour minimiser une fonction coût en vue d'obtenir des champs de vitesse précis.

La PIV est une autre technique expérimentale utilisée en recherche sur la mécanique des fluides pour mesurer avec précision les vitesses d'écoulement des fluides. Des particules spécifiques sont introduites dans l'écoulement, et leur mouvement est capturé à l'aide de caméras à grande vitesse. Le déplacement des particules entre les images est estimé pour évaluer les vecteurs de vitesse du champ d'écoulement [44]. La PIV a été appliquée *in vitro* pour étudier les schémas d'écoulement dans divers scénarios cardiovasculaires, la voie d'éjection ventriculaire gauche, les bifurcations carotidiennes et les anévrismes de l'aorte abdominale. La PIV stéréoscopique, connue sous l'acronyme SPIV, est une technique avancée de PIV qui capture des vues hors axe d'une région d'intérêt, permettant la détermination du champ vectoriel de vitesse en trois dimensions [52]. Bien que la PIV ne soit pas directement applicable à l'imagerie clinique, elle est considérée comme un outil de référence en recherche en mécanique des fluides et est utilisée pour valider d'autres techniques de mesure de vitesse.

Dans le contexte de l'imagerie du flux sanguin, en s'inspirant de la méthode du *i*VFM ou cartographie vectorielle du flux intraventricular en français [41, 42], nous avons développé une technique du vasculaire vector flow mapping (*v*VFM) ou cartographie du flux vectoriel vasculaire en français pour estimer les champs vectoriels des vitesses vasculaires en 2D. La PIV est utilisé comme une méthode de validation *in vitro* pour le *v*VFM afin de confirmer sa précision et sa fiabilité.

État de l'Art des Méthodes Non-Invasives d'Estimation de la Pression

L'étude vise à estimer la perte de charge trans-sténotique de manière non-invasive en utilisant des images Doppler couleur. Pour cela, les équations de la dynamique des fluides sont utilisées pour comprendre la relation entre vitesse et pression [58]. Un aperçu détaillé de l'utilisation de ces équations est donné dans l'état de l'art de la technologie pour estimer les chutes de pression intravasculaires avant de discuter de leurs avantages et limitations.

Un élément clé de l'étude est l'introduction des équations de Navier-Stokes qui sont des équations différentielles partielles régissant le comportement de l'écoulement des fluides [59]. Elles définissent la conservation de la masse (l'équation de continuité) et la conservation de la quantité de mouvement linéaire dans un fluide. Ces équations servent de base fondamentale dans le domaine de la dynamique des fluides et sont utilisées dans diverses équations connexes, telles que les équations de Poisson et de Bernoulli.

Les équations de Navier-Stokes sont souvent résolues numériquement en utilisant des modèles de mécanique des fluides numérique (MFN) lors de l'estimation de la chute de pression. Cette technique permet aux chercheurs de comparer les estimations de chute de pression obtenues à partir d'autres modalités telles que l'IRM et l'échographie. De plus, elle offre la possibilité d'obtenir une compréhension plus approfondie des caractéristiques hémodynamiques de l'écoulement, même avec des modèles complexes. La méthode proposée dans ce travail de thèse se concentre sur la détermination des pertes de pression artérielle post-sténose sur la base des équations de dynamique des fluides.

Ensuite, le chapitre explore l'application de l'équation de pression de Poisson et de l'équation de Bernoulli, dérivées des équations de Navier-Stokes, pour l'estimation de la chute de pression dans les cas de sténose artérielle et aortique [60]. L'équation de pression de Poisson est utilisée dans plusieurs études pour estimer les chutes de pression [57, 64]. La précision de la solution dépend fortement d'une segmentation adéquate de la région d'intérêt. Il est donc essentiel d'établir des conditions aux limites pour le fluide, ce qui implique de définir les interactions entre la région d'intérêt et les surfaces environnantes. Cette approche est très efficace lorsqu'elle est appliquée à des modalités d'imagerie haute résolution, permettant de prendre en compte la géométrie complète du vaisseau. Cependant, la capture précise du segment de vaisseau autour du site rétréci peut présenter des défis [67].

L'équation de Bernoulli est utilisée pour les écoulements non visqueux, c'est-à-dire lorsque la viscosité du fluide est supposée être nulle. L'équation de conservation de la quantité de mouvement de Navier-Stokes est alors reformulée en équation d'Euler. L'équation d'Euler est souvent utilisée dans les études impliquant l'hypothèse d'un écoulement 1D, analysant les données Doppler en mode couleur M pour mesurer les gradients de pression intraventriculaires [68–70]. Lors de l'expression de l'équation d'Euler le long d'une ligne de courant, il est possible de dériver l'équation de Bernoulli. L'équation de Bernoulli est largement utilisée dans les études utilisant la technique d'imagerie de l'écoulement sanguin IRM-CP pour estimer les gradients de pression cardiovasculaire, en particulier dans les cas de sténose artérielle [63, 64] et aortique [72]. Elle a également été appliquée à l'échocardiographie Doppler pour estimer les gradients de pression instantanés à travers la valve aortique [73], et les gradients de pression intraventriculaires [13, 74–77]. Ce chapitre explore également l'utilisation de l'indice de perte d'énergie pour évaluer la gravité de la sténose aortique [81, 82] et fournit un examen détaillé de l'équation travail-énergie dans le contexte de l'estimation non-invasive de la pression à partir de l'imagerie par IRM-CP dans l'aorte [84, 85].

Finalement, l'estimation de la perte de pression intravasculaire dans les cas de vaisseaux sténotiques et non sténotiques est examinée en utilisant des méthodologies basées sur l'imagerie du flux sanguin et les équations de la dynamique des fluides. Contrairement aux études précédentes sur la perte de pression, qui se basaient sur une équation unique, nous proposons une méthode novatrice qui combine l'équation de Bernoulli et les équations de Navier-Stokes, visant à prendre en compte à la fois la conversion de la pression statique en pression dynamique et la dissipation d'énergie due aux forces de frottement. Ainsi, pour la partie en amont de la sténose, où l'écoulement est constant, sans turbulence ni dissipation d'énergie, nous utilisons l'équation de Bernoulli. Pour la partie en aval, nous utilisons l'équation de Navier-Stokes afin de tenir compte de la perte de pression due aux forces de frottement du fluide. Malgré plusieurs défis de calcul et la nécessité d'une imagerie haute résolution, notre approche présente une compréhension plus complète du processus physique de récupération et d'estimation de la perte de pression, particulièrement bénéfique pour le diagnostic précoce dans les cas de sténose légère à modérée.

Vascular Vector Flow Mapping et Estimation de la Perte de Charge

Ce chapitre présente une nouvelle technique de 2D vascular vector flow mapping (2D-vVFM), une technique spécialisée qui décrypte un champ vectoriel de vitesse intravasculaire 2D à partir de la vitesse scalaire Doppler obtenue en couleur. Cette technique s'inspire des travaux pionniers d'Assi *et al*. [41] et de Vixège *et al*. [42]. Leur technique facilite la récupération du champ vectoriel de vitesse intraventriculaire en résolvant ingénieusement un problème d'optimisation pour la vitesse Doppler scalaire dans le ventricule gauche. L'objectif principal de la vVFM est de récupérer efficacement le champ vectoriel de vitesse 2D à partir du champ Doppler scalaire dans des sténoses quasi-axiales en résolvant un problème de moindres carrés contraint. Il s'agit d'un aspect critique de l'étude de la dynamique vasculaire. Cela implique de connaître plusieurs paramètres, tels que l'angle d'imagerie Doppler, l'axe du vaisseau par rapport à la sonde échography et la distance entre l'axe du vaisseau et le centre de la sonde. Ce chapitre fournit un aperçu détaillé des relations mathématiques du problème formulé. Cela comprend la direction vectorielle Doppler, les composantes de vitesse, la vitesse Doppler et la relation entre la vitesse Doppler mesurée et la vraie valeur de vitesse. Il prend également en compte le bruit présent dans les données mesurées, mettant en évidence la complexité du processus et la nécessité de manipuler soigneusement ces éléments pour garantir une estimation précise.

La partie suivante présente une introduction à l'équation de continuité, un principe issu du domaine de la mécanique des fluides. Ce principe est largement utilisé dans la conservation de la masse pour l'écoulement des fluides. L'équation de continuité implique la densité de masse et le vecteur de vitesse du fluide. Elle est indispensable pour décrire l'écoulement dans des volumes de référence (pixels ou voxels) et cartographier les variations de la quantité de fluide à l'intérieur d'un volume donné au fil du temps. Dans le cas du sang, considéré comme un fluide incompressible, l'équation de continuité est simplifiée en coordonnées cylindriques. Pour garantir la stabilité numérique, elle est ensuite modifiée pour tenir compte du changement de coordonnées cylindriques en coordonnées cartésiennes. Cette équation constitue une contrainte physique fondamentale pour la reconstruction du flux intravasculaire.

La deuxième contrainte mentionnée dans ce texte est la condition sur l'écoulement du sang à la paroi, aussi appelée condition aux limites. Cette condition peut être la condition de glissement ou la condition de non-glissement à la paroi. Dans le travail actuel, la condition de glissement est utilisée. Cela signifie que la composante normale de la vitesse du fluide est nulle au niveau des parois, mais il n'y a aucune adhésion du sang à la paroi dans la direction tangentielle. Le problème en question est ensuite exprimé comme un problème de minimisation contraint. Il vise à minimiser une fonction de coût, tout en étant soumis aux contraintes mentionnées ci-dessus. La fonction de coût englobe ici la cohérence entre les vitesses Doppler scalaire et le champ de vitesse 2D reconstruit, tout en intégrant un terme de lissage. Pour résoudre ce probléme et obtenir le champ vectoriel de vitesse estimé, la méthode des multiplicateurs de Lagrange est utilisée. Les multiplicateurs correspondent à la contrainte de conservation de la masse et à la condition de bord sans glissement. La solution optimale nécessite que la fonction de coût ait un minimum, ce qui nécessite que la dérivée soit nulle. Finalement, le champ de vitesse 2D est reconstruit, première étape primordiale pour l'étude du flux intravasculaire.

La deuxième partie du chapitre décrit une approche novatrice pour estimer les pertes de charge dans le système cardiovasculaire, en se concentrant spécifiquement sur la zone suivant une sténose artérielle. Elle aborde différentes équations de dynamique des fluides utilisées à cette fin, notamment les équations de Navier-Stokes et de Poisson. Cependant, l'utilisation de ces équations individuellement s'est révélée insatisfaisante en raison des difficultés de calcul des dérivées d'ordre supérieur, de la faible détection de la frontière du modèle de sténose artérielle et des problèmes numériques lors du processus de résolution.

Pour surmonter ces limites, un modèle de turbulence algébrique a été introduit [87]. Ce modèle ajoute une viscosité turbulente à la viscosité dynamique du fluide. Cependant, même ce modèle n'était pas sans défaut, car il conduisait à une surestimation des valeurs de perte de charge. Il a également été constaté que l'équation de Bernoulli n'est pas adaptée car elle ne tenait pas compte de la viscosité du fluide et de la dissipation d'énergie causée par les forces de frottement à l'intérieur du fluide.

L'étude propose alors une nouvelle méthode qui combine les équations de Bernoulli et de Navier-Stokes. La géométrie est divisée en deux sections pour aborder les différents aspects physiques de l'écoulement dans la région sténosée. L'équation de Bernoulli est utilisée pour la région de l'entrée jusqu'à la *vena contracta* (milieu de la sténose), où l'écoulement du fluide présente un comportement cohérent sans dissipation d'énergie. L'équation de Navier-Stokes est utilisée dans la seconde région (de la *vena contracta* jusqu'à la sortie) où la majorité de la dissipation d'énergie se produit, en raison des forces de frottement résultant de la viscosité du fluide dans la zone divergente.

Enfin, il décrit un processus de validation en deux étapes pour la méthode proposée utilisant le Doppler couleur pour l'estimation des pertes de charge post-sténose. La première étape implique une validation *in silico* à l'aide de simulations MFN et d'imagerie par ultrasons. La deuxième étape comprend une validation *in vitro* à l'aide de PIV et d'imagerie Doppler couleur.

Stratégie de Validation

Dans le but de mesurer la perte de charge artérielle trans-sténotique à l'aide de l'imagerie Doppler couleur clinique, deux problèmes d'optimisation doivent être résolus. Le premier problème concerne l'estimation du champ vectoriel de vitesse 2D à partir d'une vitesse scalaire obtenue par imagerie Doppler couleur (vVFM). Le deuxième utilise une nouvelle méthode de dynamique des fluides pour estimer la perte de charge sur la base des données de vitesse 2D. Les solutions à ces deux problèmes ont été efficacement transformées en systèmes de matrices linéaires et en schéma de discrétisation finie.

Cette nouvelle méthode a été validée à la fois *in silico* (via la MFN et les simulations d'imagerie par ultrasons (SIMUS) [88, 89]) et *in vitro* (via la PIV et l'échographie Doppler couleur).

Dans les simulations de MNF et d'ultrasons, un flux sanguin dans des modèles axisymétriques de sténoses carotidiennes a été simulé à l'aide du logiciel COMSOL Multiphysics, avec des paramètres proches de ceux observés en clinique tels que le diamètre de l'artère carotide commune, les formes et degrés de sténose, ainsi que les débits. Ensuite, des simulations Doppler couleur à l'aide du logiciel SIMUS ont été réalisées.

Des expériences PIV ont également été réalisées. Cela a impliqué la création d'un fantôme PIV, une étape cruciale pour valider notre stratégie. Le fantôme devait être totalement transparent et posséder une consistance et une rigidité adéquate. L'étude a également fourni des étapes détaillées pour la fabrication de fantômes, en se concentrant sur la technique de lost-core casting [91–95] et permettant de personnalisation, telle que l'épaisseur de paroi. Ensuite, ce chapitre décrit l'approche utilisée pour fabriquer des fantômes pour les expériences d'imagerie PIV. Les fantômes sont généralement fabriqués en utilisant la technique de lost-core casting, mais cette méthode a des limites, notamment : des restes de matériel de noyau [95], un manque de lissage avec les noyaux imprimés en 3D [92], et des coûts et des temps de consommation élevés en raison de la nécessité de noyaux jetables.

Pour répondre à ces problèmes, un noyau de fantôme en aluminium a été conçu qui n'implique pas la perte du noyau à chaque création de nouveau fantôme, tout en ayant une surface suffisamment lisse pour l'imagerie PIV. Le noyau eprésente un modèle simplifié d'une artère carotide commune avec une sténose, et a été divisé en deux pièces pour son extraction du fantôme après fabrication.

Les dimensions du fantôme sont basées sur les dimensions physiologiques de l'artère carotide commune rapportées dans la littérature [13, 47], deux types de sténoses ont été fabriquées : les formes cosinus et gaussien, avec des réductions de diamètre de 50% et 60%. Ce niveau de sténose a été choisi pour éviter les complications avec les mesures expérimentales et pour s'aligner sur le but de l'étude, qui était d'estimer la perte de charge dans une sténose artérielle légère à modérée [96].

Les longueurs des sections d'entrée et de sortie du noyau ont été conçues pour assurer un profil de vitesse complètement développé à l'intérieur du fantôme et une récupération complète de la pression après avoir traversé la zone sténotique. La longueur de la sténose a été choisie en fonction de l'impact minimal qu'elle avait sur la perte de charge par rapport au diamètre de la sténose et son alignement avec les longueurs de plaques cliniquement observées [97–99].

Les noyaus ont été conçus à l'aide de SolidWorks et fabriqués en utilisant une technique d'usinage à commande numérique. Nous avons choisi d'utiliser le polydiméthylsiloxane (PDMS) [47, 50] en raison de ses propriétés de haute transparence, de non-toxicité, de durabilité et de stabilité thermique. Un moule à quatre pièces a été conçu et fabriqué à l'aide d'une imprimante 3D pour créer des fantômes avec des parois bien définies. L'épaisseur des parois des fantômes a été fixée à 2 mm pour assurer une rigidité et une transparence suffisante pour l'imagerie .

Par la suite, une attention particulière est portée au processus de fabrication du fantôme PDMS pour et aux expériences d'échographie Doppler couleur, ainsi que l'exploration de matériaux alternatifs au PDMS.

Au début, le chapitre détaille les étapes pour préparer le fantôme PDMS en utilisant une base et un agent de durcissement, mélangés dans un rapport de 10:1, et une chambre à vide pour éliminer les bulles. Le mélange est soigneusement versé dans un moule imprimé en 3D, dont les surfaces intérieures sont recouvertes de ruban adhésif afin d'assurer une surface extérieure lisse et transparente. Le moule rempli durcit ensuite à température ambiante pendant deux jours. Après durcissement, les pièces de noyau sont délicatement extraites du fantôme.

Nous avons cherché dans la littérature les propriétés acoustiques du PDMS. En particulier, la vitesse de propagation du son, qui est indiquée être environ 12% plus faible que dans l'eau ou les tissus mous. Nos estimations sur notre fantôme ont montré une baisse de 27%.

En raison de la vitesse de propagation du son plus faible dans le PDMS [101], l'étude explore des matériaux alternatifs, y compris le polyvinyl chloride plastisol (PVCP) [103, 104] et le polyvinyl alcohol hydrogel (PVA) [105, 106]. Le PVCP, bien qu'il possède des propriétés acoustiques similaires à l'eau, manque de rigidité, consistance nécessaire pour la construction de fantômes. Le PVA, en revanche, s'est avéré une meilleure alternative. En utilisant du dimethyl sulfoxide (DMSO) comme solvant, Hyon *et al.* [107] ont fabriqué un hydrogel PVA transparent correspondant aux propriétés acoustiques des tissus humains, et ont montré que la vitesse de propagation du son était conforme à d'autres études.

Les défis rencontrés lors de la fabrication d'un fantôme sténotique pour des expériences d'imagerie à double modalité utilisant l'échographie et la ont également été discutés. Les premières tentatives ont échoué en raison de problèmes tels qu'une rigidité insuffisante, une mauvaise consistance et des difficultés à éliminer les petites bulles. Pour résoudre ces problèmes, le matériau a été laissé à reposer avant d'initier le processus de congélation, mais des bulles sont restées emprisonnées dans le matériau. Il a ensuite été décidé de mener les deux techniques d'imagerie dans le même dispositif expérimental et d'utiliser des fantômes transparents construits avec du PDMS. Cependant, il y avait des difficultés à obtenir des images précises, en particulier dans la sténose, en raison de la déviation et de la réfraction des ondes sonores causées par différentes vitesses du son dans les différents milieux.

Pour les expériences de , des fantômes de sténose carotidienne à échelle réelle ont été fabriqués en utilisant du PDMS et testés dans un circuit fermé rempli d'un fluide imitant le sang (blood mimicking fluid (BMF)) [13, 54, 63]. Le BMF était composé de 60% d'eau filtrée et de 40% de glycérol pour imiter de près les caractéristiques d'écoulement du sang humain et maintenir la consistance des indices de réfraction [50, 91, 101]. Le fluide était mélangé avec des particules de polyamide, qui ont efficacement suivi le chemin de l'écoulement, facilitant un suivi précis et une caractérisation au sein du dispositif expérimental. Une pompe à engrenages à vitesse variable a été utilisée pour générer un écoulement constant, et les débits ont été mesurés avec un débitmètre électromagnétique. Pour assurer la précision du débitmètre, un niveau de conductivité minimum a été maintenu en dissolvant une quantité suffisante de sel dans le liquide. L'écoulement continu du fluide a été maintenu pendant une demi-heure pour le stabiliser et minimiser les perturbations ou fluctuations potentielles. Un transducteur de pression intégré à un cathéter a également été utilisé pour mesurer les pressions à l'intérieur des fantômes. À l'aide de ce capteur de pression qui était connecté à un appareil ComboMap et de débit, les pressions aux entrées et sorties du fantôme ont été soigneusement surveillées. Les valeurs de pression obtenues ont été considérées comme une référence [115, 116] par rapport à laquelle les résultats expérimentaux ont été comparés, garantissant une évaluation précise et une validation des résultats expérimentaux.

Pour l'expérience de , une source laser a été utilisée pour éclairer la région d'intérêt et une caméra numérique haute vitesse a été utilisée pour capturer le déplacement des particules dans l'écoulement et estimer le champ vectoriel de vitesse. Les images capturées ont été traitées à l'aide du logiciel lab [117], qui calcule la distribution de vitesse au sein de paire d'images de particules et fournit plusieurs paramètres liés à l'écoulement. Le logiciel évalue la corrélation croisée de nombreuses petites sous-images pour calculer le déplacement total des particules. Le logiciel se compose de trois étapes principales : pré-traitement, traitement, et post-traitement. Dans l'étape de pré-traitement, diverses techniques sont appliquées pour améliorer la qualité de l'image d'entrée. Pendant le traitement des image, deux approches sont utilisées pour déterminer les déplacements et les vitesses des particules. Ici, nous avons choisi d'utiliser l'approche de la transformée de Fourier rapide (TFR) en raison de son faible coût calculatoire. Enfin, dans l'étape de post-traitement, des techniques de validation sont incorporées pour évaluer la qualité et la fiabilité des vitesses mesurées. Le logiciel comprend également des outils pour analyser et interpréter les champs de vitesse obtenus.

Pour l'imagerie par ultrasons Doppler couleur, un scanner à ultrasons GE et une sonde linéaire GE 9L ont été utilisés pour acquérir les images en ajustant la fréquence de répétition du système en fonction du débit. Pour améliorer la qualité de l'image, la sonde a été immergée dans un réservoir d'eau contenant notre sténose. Après l'acquisition des séquences, les données brutes ont été extraites à l'aide du logiciel EchoPAC, consolidées dans un fichier HDF, et traitées avec la boîte à outils MUST.

Comme des résultats précis n'ont pas été obtenus à partir du fantôme PDMS lors de l'imagerie par ultrasons, nous avons décidé de mener des expériences de Doppler couleur séparées avec un fantôme plus adapté. Nous avons examiné deux matériaux : l'hydrogel PVA et l'agar. Ils sont tous les deux reconnus pour leurs caractéristiques favorables pour l'imagerie par ultrasons. Malgré les tentatives d'amélioration de la rigidité du PVA par des cycles de congélation et de décongélation, les conditions expérimentales n'ont pas été acceptables car le PVA gonflait sous le flux. Par conséquent, nous avons utilisé un fantôme sans paroi en utilisant de l'agar [94, 119], qui avait un temps de préparation plus court et un processus de fabrication plus simple. Cependant, retirer les deux pièces métalliques de l'agar solidifié a présenté des défis. Cette opération a endommagé le fantôme, ce qui a nécessité la création de plusieurs autres fantômes. Pour assurer l'intégrité du fantôme, l'imagerie par ultrasons en mode B a été utilisée.

Pour l'expérience d'échographie Doppler couleur *in vitro*, le même dispositif d'écoulement a été employé que pour les expériences de , mais des particules d'amidon de maïs ont été utilisées à la place des particules de polyamide pour simuler le comportement des globules rouges dans l'écoulement sanguin. La même méthode que celle décrite pour l'acquisition et l'analyse des images d'échographie Doppler couleur dans le dispositif à double modalité a été suivie.

Résultats de l’Estimation Non-Invasive de la Perte de Charge

Ce chapitre s’est concentrée sur l’estimation non-invasive de la perte de charge trans-sténosique à partir d’images cliniques de Doppler couleur dans la sténose carotidienne. La validation *in silico* a impliqué la MFN et la SIMUS pour des modèles de sténose carotidienne en forme de cosinus et de gaussien ayant un degré d’occlusion de 60% et 70% de réduction du diamètre. Les conditions d’écoulement dans les modèles de sténose carotidienne ont été simulées en utilisant la MFN, reproduisant les vitesses de Doppler à partir des résultats de la MFN en utilisant SIMUS, et en comparant les estimations de perte de charge à la référence obtenue en MFN. Les résultats ont montré que la technique *v*VFM estime avec précision le champ vectoriel de vitesse à partir du Doppler couleur dans les sténoses artérielles. Les champs de vitesse ont été analysés et comparés, montrant un fort accord entre *v*VFM et le MFN et démontrant la précision de la méthode *v*VFM. De même, les pertes de charge estimées en utilisant la *v*VFM et celles calculées par la MFN ont une forte corrélation ($r^2 = 0.96$), validant en simulation la méthode proposée pour estimer les pertes de charge à partir du Doppler couleur.

La validation *in vitro* a été réalisée en utilisant la PIV et des expériences d’imagerie par échographie Doppler couleur sur des fantômes de sténose carotidienne. Les résultats des expériences *in vitro* conçues pour valider une technique non-invasive pour estimer la perte de charge dans la sténose artérielle en utilisant la PIV ont été présentés. Un total de 44 expériences ont été menées en utilisant des fantômes en forme de cosinus et de Gaussienne, reflétant une réduction du diamètre de l’artère de 50% et 60%. Les débits variaient entre 0,2 et 1,2 $\mathrm{L \cdot min^{-1}}$, reproduisant les débits sanguins physiologiques dans les vaisseaux périphériques.

La méthode PIV a fourni des champs vectoriel de vitesse précis, ce qui a facilité l’estimation de la perte de charge post-sténosique. Une forte relation linéaire a été observée entre les pertes de charge dérivées de la PIV et celles mesurées par les capteurs de pression intégrés dans les fantômes ($r^2 = 0.94$), validant le deuxième problème inverse sur des arguments expérimentaux.

Un diagramme de Bland-Altman a été utilisé pour évaluer l’influence du débit sur les valeurs de perte de charge. Les résultats ont indiqué que l’écart entre les pertes de charge estimées à partir de la PIV et les lectures des capteurs devenait plus prononcé avec l’augmentation des débits, en accord avec les résultats attendus. Cet écart a été attribué à la perte d’information inhérente à la capture d’un plan 2D à partir d’une expérience 3D.

Les expériences ont montré que pour les modèles en forme de cosinus et de Gaussienne, une augmentation du débit a conduit à des vitesses de jet plus élevées et donc à une plus grande turbulence post-sténosique et perte de charge. Une observation notable était un écart par rapport à l’axisymétrie dans l’écoulement du jet en raison de la géométrie expérimentale du fantôme. Malgré cela, la méthodologie reste efficace et robuste. Lors de l’examen des valeurs de perte de charge, il a été observé que le degré de sténose avait une influence plus prononcée sur l’augmentation des valeurs de perte de charge que la forme de la sténose.

En raison des difficultés à obtenir les résultats souhaités en utilisant des fantômes en PDMS transparents dans une configuration expérimentale à double modalité pour des expériences simultanées de PIV et d’imagerie Doppler, il a été décidé d’établir une configuration expérimentale distincte pour l’imagerie *in vitro* Doppler couleur. La technique a été validée par des expériences *in vitro* menées sur des fantômes de sténose carotidienne en utilisant un appareil à ultrasons portable GE. L'étude a appliqué la méthode *v*VFM pour calculer le champ de vecteurs de vitesse à partir des images Doppler couleur, qui a ensuite été utilisé pour estimer la perte de charge en aval de la sténose. Un total de 44 expériences ont été menées (comme pour la PIV), explorant différents profils de sténose et degrés d'occlusion, et testées à différents débits. Les pertes de charge estimées en utilisant la méthode *v*VFM ont été comparées aux données directement mesurées à partir de capteurs de pression, montrant une forte corrélation ($r^2 = 0.97$), ce qui a confirmé l'exactitude et la validité de la méthode proposée. Une analyse de Bland-Altman a révélé que la précision des pertes de charge estimées diminuait à mesure que le débit augmentait, à nouveau attribué à la complexité de la capture d'un phénomène 3D au sein d'une géométrie 2D.

En conclusion, la faisabilité de la technique pour estimer les pertes de charge turbulentes dans les sténoses artérielles en utilisant l'échographie Doppler couleur clinique a été démontrée. Malgré les limitations et les incertitudes liées aux conditions expérimentales, les résultats sont fiables et précis. Il reste cependant encore du travail de recherche à réaliser en vue d'augmenter l'applicabilité et la généralisabilité de cette technique.

Discussion et Conclusion

L'objectif de ce travail de thèse visait à estimer de manière non-invasive la chute de pression trans-sténotique dans une sténose artérielle légère à modérée. Ceci est essentiel pour une détection précoce et une intervention clinique appropriée, car ces stades ne présentent souvent aucun symptôme et sont difficiles à évaluer.

L'échographie Doppler couleur a été utilisée, une technique d'imagerie en temps réel, largement disponible et facile à utiliser, qui mesure la vitesse du sang. Bien que d'autres techniques d'imagerie fournissent des données de résolution plus élevée, elles sont moins pratiques en raison de la nécessité de traiter les données brutes d'ultrasons, souvent indisponibles dans les scanners cliniques standard.

Une méthode basée sur l'optimisation a été développée, appelée vVFM, pour estimer la carte vectorielle de vitesse 2D du flux sanguin à partir du champ de vitesse Doppler couleur scalaire. Cette approche résout efficacement et rapidement un problème des moindres carrés contraint, ce qui la rend compatible avec la pratique clinique.

L'estimation de la chute de pression a été réalisée grâce à une combinaison des équations de Bernoulli et de Navier-Stokes. L'équation de Bernoulli a été utilisée pour la zone en amont de la sténose, et l'équation de Navier-Stokes a été appliquée à la zone en aval pour tenir compte de la dissipation d'énergie.

La méthode a été validée par des simulations *in silico* et des expériences *in vitro* sur des modèles de sténose carotidienne, donnant des résultats prometteurs. Malgré certaines limitations expérimentales, telles que des fantômes de sténose parfaitement droits et une instabilité de flux due à la turbulence, la méthode a estimé les chutes de pression avec une grande précision.

L'étude vise à offrir un outil de diagnostic rapide et fiable pour les sténoses artérielles légères à modérées. Il a été précisé que cette méthode peut ne pas être nécessaire pour le diagnostic de sténoses clairement sévères, qui présentent des symptômes prononcés et nécessitent un traitement immédiat. Cependant, l'approche proposée pourrait être bénéfique pour les sténoses modérées, aidant à un diagnostic plus précoce.

Cette étude présente cependant certaines limitations. Elle n'a testé que des conditions avec un flux quasi-axisymétrique et stable, alors la circulation sanguine dans le corps est pulsatile (en phase avec les cycles cardiaques), et que la sténose est asymétrique. De plus, la méthode utilisée a été développée pour une géométrie axisymétrique 2D, alors que la sténose artérielle est 3D. L'étude s'est également concentrée uniquement sur l'artère carotide commune et a négligé d'autres facteurs tels que la ramification, la tortuosité et la nature de la plaque sténotique. Les modèles de sténose physiques et simulés avaient des parois rigides, ce qui ne reflète pas les conditions physiologiques réelles. Expérimentalement, des conditions identiques ne pouvaient pas être maintenues pour les tests PIV et Doppler couleur, ce qui a probablement conduit à une variance dans les résultats. L'introduction d'un combowire pourrait aussi avoir modifié le modèle de flux, bien que sa dimension soit très fine.

Le travail futur vise à étendre la méthode non-invasive pour accommoder à la fois les fantômes de flux sténotiques asymétriques et pulsatile et tout en prenant en compte l'effet du désalignement de la sonde à ultrasons. La faisabilité de la technique en milieu clinique doit être explorée par des essais *in vivo*, même si les erreurs d'acquisition de données réduiraient la précision, en particulier avec les mesures basées sur les cathéters servant de référence.

En conclusion, la sténose artérielle peut entraîner des complications significatives sans un diagnostic rapide aux stades précoces et un traitement approprié. La capacité à évaluer avec précision la gravité de la sténose de manière non-invasive est essentielle, et ce travail vise à développer une méthode non-invasive pour estimer la chute de pression trans-sténotique par imagerie Doppler couleur clinique. La revue des modalités d'imagerie du flux sanguin a souligné les avantages et les limites de diverses techniques telles que la IRM-CP et l'imagerie par ultrasons, avec un focus spécifique sur la méthode *i*VFM par Doppler couleur comme méthode de défaut. Ensuite, la technique *v*VFM a été explorée, en mettant l'accent sur son potentiel pour dériver un champ vectoriel de vitesse intravasculaire 2D à partir de la vitesse Doppler couleur scalaire et pour offrir une méthode d'estimation de pression non-invasive fiable à travers les équations de la dynamique des fluides. La complexité de la dynamique des fluides et les limites des méthodes actuelles d'estimation de la pression nécessitent une approche combinée, intégrant les équations de Bernoulli et de Navier-Stokes, pour fournir une compréhension plus complète de la chute de pression dans la sténose intravasculaire. Les méthodes de validation pour cette approche non-invasive proposée ont consisté en des simulations *in silico* et des expériences *in vitro*, en utilisant une variété d'outils incluant la MFN, SIMUS, la PIV et l'imagerie Doppler couleur clinique. Ces efforts de validation rigoureux ont démontré la fiabilité de la méthode proposée, révélant un fort accord entre les valeurs estimées et mesurées. La méthode a montré sa résilience face à de petites erreurs environnementales et a souligné l'influence du débit et du degré de sténose sur les valeurs de chute de pression. En somme, ce travail, malgré ses limites, souligne le potentiel de cette technique non-invasive pour estimer avec précision la chute de pression trans-sténotique dans la sténose carotidienne, offrant une base prometteuse pour le diagnostic précoce et la prise de décision thérapeutique. Cependant, des recherches et des améliorations supplémentaires sont nécessaires pour améliorer la capacité de la technique à représenter des phénomènes de flux pulsatile tridimensionnel et son applicabilité aux flux sténotiques pulsatiles asymétriques. Les futures travaux se concentreront probablement sur l'amélioration de ces aspects et sur l'évaluation de la faisabilité clinique de cette technique par des expériences *in vivo*.

Academic portfolio

International and national conferences with peer review

- **S. Choupani**, F. Varray, B., J. C. Béra, and D. Garcia, "Arterial Pressure Loss from Vascular Vector Flow Mapping with Conventional Color Doppler", *2023 IEEE 20th International Symposium on Biomedical Imaging (ISBI)*, Cartagena, Colombia, 2023, pp. 1-5, doi: 10.1109/ISBI53787.2023.10230728.
- **S. Choupani**, F. Varray, B., J. C. Béra, and D. Garcia, "Measurement of Pressure Drop in Arterial Stenosis with Color Doppler Imaging", in *28th Congress of the European Society of Biomechanics (ESB)*, Jul. 2023. Oral presentation.
- **S. Choupani**, F. Varray, B., J. C. Béra, and D. Garcia, "Estimation of Arterial Transstenotic Pressure Loss using Color Doppler Imaging", in *IEEE International Ultrasonics Symposium (IUS)*, Sep. 2023. Oral presentation.
- **S. Choupani**, F. Varray, B., J. C. Béra, and D. Garcia, "Noninvasive estimation of pressure drop in arterial stenoses with color Doppler ultrasound", in *44ème congrès de la Société de Biomécanique*, Oct. 2023. Oral presentation.

Other presentations without proceedings

- **S. Choupani**, F. Varray, B., J. C. Béra, and D. Garcia, "Intravascular manometry by color Doppler", in *8th SLEIGHT Science Event: the present and future of photonic technologies for health and space*, Jul. 2022. Oral presentation.
- **S. Choupani**, F. Varray, B., J. C. Béra, and D. Garcia, "Arterial Pressure Loss from Vascular Vector Flow Mapping with Conventional Color Doppler", in *8th La réunion de l'Advisory Board de l'EUR Manutech-SLEIGHT*, Jun. 2023. Poster presentation.

References

[1] J. W. Kimball, *Kimball's biology pages*. Kimball, John W., 1999.

[2] M. G. Suzanne Wakim, *Human Biology*. Butte College, 2023.

[3] M. Thiriet, M. Delfour, and A. Garon, "Vascular stenosis," 2015.

[4] M. Charlick and J. M. Das, "Anatomy, head and neck, internal carotid arteries," in *StatPearls [Internet]*, StatPearls Publishing, 2021.

[5] S. Chaturvedi and P. M. Rothwell, *Carotid artery stenosis: current and emerging treatments*. CRC Press, 2005.

[6] E. Messas, G. Goudot, A. Halliday, J. Sitruk, T. Mirault, L. Khider, F. Saldmann, L. Mazzolai, and V. Aboyans, "Management of carotid stenosis for primary and secondary prevention of stroke: state-of-the-art 2020: a critical review," *European Heart Journal Supplements*, vol. 22, no. Supplement_M, pp. M35–M42, 2020.

[7] I. Fernández-Ruiz, "Carotid artery stenosis—stenting or endarterectomy?," *Nature Reviews Cardiology*, vol. 13, no. 4, pp. 181–181, 2016.

[8] A. Saxena, E. Y. K. Ng, and S. T. Lim, "Imaging modalities to diagnose carotid artery stenosis: progress and prospect," *Biomedical engineering online*, vol. 18, pp. 1–23, 2019.

[9] G. A. Donnan, S. M. Davis, B. R. Chambers, P. C. Gates, G. J. Hankey, J. J. McNeil, D. Rosen, E. G. Stewart-Wynne, and R. R. Tuck, "Streptokinase for acute ischemic stroke with relationship to time of administration," *Jama*, vol. 276, no. 12, pp. 961–966, 1996.

[10] B. Sui, P. Gao, Y. Lin, L. Jing, S. Sun, and H. Qin, "Hemodynamic parameters distribution of upstream, stenosis center, and downstream sides of plaques in carotid artery with different stenosis: a MRI and CFD study," *Acta Radiologica*, vol. 56, no. 3, pp. 347–354, 2015.

[11] S. Ko, J. Lee, S. Song, D. Kim, S. H. Lee, and J.-H. Cho, "Patient-specific hemodynamics of severe carotid artery stenosis before and after endarterectomy examined by 4D flow MRI," *Scientific Reports*, vol. 9, p. 18554, 2019.

[12] C.-H. Li, B.-L. Gao, J.-W. Wang, J.-F. Liu, H. Li, and S.-T. Yang, "Hemodynamic factors affecting carotid sinus atherosclerotic stenosis," *World Neurosurgery*, vol. 121, pp. e262–e276, 2019.

[13] J. B. Olesen, C. A. Villagómez-Hoyos, N. D. Møller, C. Ewertsen, K. L. Hansen, M. B. Nielsen, B. Bech, L. Lönn, M. S. Traberg, and J. A. Jensen, "Noninvasive estimation

of pressure changes using 2-D vector velocity ultrasound: an experimental study with in vivo examples," *IEEE Transactions on Ultrasonics, Ferroelectrics, and Frequency Control*, vol. 65, no. 5, pp. 709–719, 2018.

[14] W. Grossman, *Grossman's cardiac catheterization, angiography, and intervention*. Lippincott Williams & Wilkins, 2006.

[15] M. Meusel, P. Wegerich, B. Bode, E. Stawschenko, K. Kusche-Vihrog, H. Hellbrück, and H. Gehring, "Measurement of blood pressure by ultrasound—the applicability of devices, algorithms and a view in local hemodynamics," *Diagnostics*, vol. 11, no. 12, p. 2255, 2021.

[16] K. Iwasaki and S. Kusachi, "Coronary pressure measurement based decision making for percutaneous coronary intervention," *Current cardiology reviews*, vol. 5, no. 4, pp. 323–333, 2009.

[17] N. H. Pijls, B. De Bruyne, G. J. W. Bech, F. Liistro, G. R. Heyndrickx, H. J. Bonnier, and J. J. Koolen, "Coronary pressure measurement to assess the hemodynamic significance of serial stenoses within one coronary artery: validation in humans," *Circulation*, vol. 102, no. 19, pp. 2371–2377, 2000.

[18] H. Ha, J. Lantz, M. Ziegler, B. Casas, M. Karlsson, P. Dyverfeldt, and T. Ebbers, "Estimating the irreversible pressure drop across a stenosis by quantifying turbulence production using 4D flow MRI," *Scientific reports*, vol. 7, no. 1, pp. 1–14, 2017.

[19] R. Fitridge and M. Thompson, *Mechanisms of vascular disease: a reference book for vascular specialists*. University of Adelaide Press, 2011.

[20] S. Ivar Seldinger, "Catheter replacement of the needle in percutaneous arteriography: a new technique," *Acta radiologica*, vol. 49, no. sup434, pp. 47–52, 2008.

[21] A.-J. Fordham, C.-C. Hacherl, N. Patel, K. Jones, B. Myers, M. Abraham, and J. Gendreau, "Differentiating glioblastomas from solitary brain metastases: an update on the current literature of advanced imaging modalities," *Cancers*, vol. 13, no. 12, p. 2960, 2021.

[22] D. T. Wymer, K. P. Patel, W. F. Burke III, and V. K. Bhatia, "Phase-contrast MRI: physics, techniques, and clinical applications," *Radiographics*, vol. 40, no. 1, pp. 122–140, 2020.

[23] D. Vray, E. Brusseau, V. Detti, F. Varray, A. Basarab, O. Beuf, O. Basset, C. Cachard, H. Liebgott, and P. Delachartre, "Ultrasound medical imaging," *Medical Imaging Based on Magnetic Fields and Ultrasounds*, pp. 1–72, 2014.

[24] V. Perrot, M. Polichetti, F. Varray, and D. Garcia, "So you think you can DAS? a viewpoint on delay-and-sum beamforming," *Ultrasonics*, vol. 111, p. 106309, 2021.

[25] M. Couade, "The advent of ultrafast ultrasound in vascular imaging: a review," *J Vasc Diagn Intervent*, vol. 4, pp. 9–22, 2016.

[26] D. Garcia, P. Lantelme, and E. Saloux, "Introduction to speckle tracking in cardiac ultrasound imaging," *Handbook of speckle filtering and tracking in cardiovascular ultrasound imaging and video. Institution of Engineering and Technology*, pp. 571–598, 2018.

[27] S. Fadnes, S. Bjærum, H. Torp, and L. Lovstakken, "Clutter filtering influence on blood velocity estimation using speckle tracking," *IEEE transactions on ultrasonics, ferroelectrics, and frequency control*, vol. 62, no. 12, pp. 2079–2091, 2015.

[28] S. A. Nyrnes, S. Fadnes, M. S. Wigen, L. Mertens, and L. Lovstakken, "Blood speckle-tracking based on high–frame rate ultrasound imaging in pediatric cardiology," *Journal of the American Society of Echocardiography*, vol. 33, no. 4, pp. 493–503, 2020.

[29] V. Perrot and D. Garcia, "Back to basics in ultrasound velocimetry: tracking speckles by using a standard PIV algorithm," in *2018 IEEE International Ultrasonics Symposium (IUS)*, pp. 206–212, IEEE, 2018.

[30] A. S. Daae, M. S. Wigen, S. Fadnes, L. Løvstakken, and A. Støylen, "Intraventricular vector flow imaging with blood speckle tracking in adults: feasibility, normal physiology and mechanisms in healthy volunteers," *Ultrasound in medicine & biology*, vol. 47, no. 12, pp. 3501–3513, 2021.

[31] J. A. Jensen, S. I. Nikolov, C. Alfred, and D. Garcia, "Ultrasound vector flow imaging—part I: Sequential systems," *IEEE transactions on ultrasonics, ferroelectrics, and frequency control*, vol. 63, no. 11, pp. 1704–1721, 2016.

[32] M. Strachinaru, J. Voorneveld, L. B. Keijzer, D. J. Bowen, F. O. Mutluer, F. t. Cate, N. de Jong, H. J. Vos, J. G. Bosch, and A. E. van den Bosch, "Left ventricular high frame rate echo-particle image velocimetry: clinical application and comparison with conventional imaging," *Cardiovascular Ultrasound*, vol. 20, no. 1, p. 11, 2022.

[33] J. Voorneveld, H. Saaid, C. Schinkel, N. Radeljic, B. Lippe, F. J. Gijsen, A. F. Van Der Steen, N. De Jong, T. Claessens, H. J. Vos, *et al.*, "4-D echo-particle image velocimetry in a left ventricular phantom," *Ultrasound in medicine & biology*, vol. 46, no. 3, pp. 805–817, 2020.

[34] P. Hansen, G. Cross, and L. Light, "Beam-angle independent doppler velocity measurement in superficial vessels," *Clinical blood flow measurement*, pp. 28–32, 1974.

[35] B. Dunmire, K. Beach, K. Labs, M. Plett, and D. Strandness Jr, "Cross-beam vector doppler ultrasound for angle-independent velocity measurements," *Ultrasound in medicine & biology*, vol. 26, no. 8, pp. 1213–1235, 2000.

[36] B. Y. Yiu and C. Alfred, "Least-squares multi-angle doppler estimators for plane-wave vector flow imaging," *IEEE transactions on ultrasonics, ferroelectrics, and frequency control*, vol. 63, no. 11, pp. 1733–1744, 2016.

[37] J. A. Jensen, S. I. Nikolov, C. Alfred, and D. Garcia, "Ultrasound vector flow imaging—part II: Parallel systems," *IEEE transactions on ultrasonics, ferroelectrics, and frequency control*, vol. 63, no. 11, pp. 1722–1732, 2016.

[38] C. Madiena, J. Faurie, J. Porée, and D. Garcia, "Color and vector flow imaging in parallel ultrasound with sub-nyquist sampling," *IEEE transactions on ultrasonics, ferroelectrics, and frequency control*, vol. 65, no. 11, pp. 795–802, 2018.

[39] J. Udesen and J. Jensen, “Investigation of transverse oscillation method,” *IEEE transactions on ultrasonics, ferroelectrics, and frequency control*, vol. 53, no. 5, pp. 959–971, 2006.

[40] D. Garcia, J. C. Del Alamo, D. Tanne, R. Yotti, C. Cortina, É. Bertrand, J. Antoranz, E. Pérez-David, R. Rieu, F. Fernandez-Aviles, and J. Bermejo, “Two-dimensional intraventricular flow mapping by digital processing conventional color-doppler echocardiography images,” *IEEE transactions on medical imaging*, vol. 29, no. 5, pp. 1701–13, 2010.

[41] K. Assi, E. Gay, C. Chnafa, S. Mendez, N. Franck, J. Abascal, P. Lantelme, F. Tournoux, and D. Garcia, “Intraventricular vector flow mapping - a doppler-based regularized problem with automatic model selection,” *Physics in Medicine & Biology*, vol. 62, no. 3, pp. 7131–7147, 2017.

[42] F. Vixége, A. Berod, Y. Sun, S. Mendez, O. Bernard, N. Ducros, P.-y. Courand, N. Franck, and D. Garcia, “Physics-constrained intraventricular vector flow mapping by color doppler,” *Physics in Medicine & Biology*, vol. 66, no. 24, p. 245019, 2021.

[43] M. N. Antonuccio, H. Morales, A. This, K. Capellini, S. Avril, S. Celi, and L. Rouet, “Towards the 2D velocity reconstruction in abdominal aorta from color-doppler ultrasound,” *Medical Engineering & Physics*, vol. 107, p. 103873, 2022.

[44] R. J. Adrian, “Twenty years of particle image velocimetry,” *Experiments in Fluids*, vol. 39, pp. 159–169, 2005.

[45] A. Goharzadeh, A. Molki, and M. Ohadi, “A proposed particle image velocimetry (PIV) system for instructional purposes in a modern mechanical engineering undergraduate laboratory program,” *ASEE Annual Conference and Exposition, Conference Proceedings*, pp. 11–103, 2006.

[46] P. R. Leinan and et al., “Comparison of ultrasound vector flow imaging and CFD simulations with PIV measurements of flow in a left ventricular outflow trackt phantom - implications for clinical use and in silico studies,” *Computers in biology and medicine*, vol. 146, p. 105358, 2022.

[47] A. DiCarlo, D. Holdsworth, and T. Poepping, “Study of the effect of stenosis severity and non-newtonian viscosity on multidirectional wall shear stress and flow disturbances in the carotid artery using particle image velocimetry,” *Medical Engineering & Physics*, vol. 65, 2019.

[48] N. Buchmann, C. Nguyen, J. Wells, and M. Jermy, “In-vitro wall shear stress measurements using interfacial particle image velocimetry (IPIV),” *In 14th International Symposium on Applications of Laser Techniques to Fluid Mechanics*, pp. 7–10, 2008.

[49] N. Buchmann, C. Atkinson, M. Jeremy, and J. Soria, “Tomographic particle image velocimetry investigation of the flow in a modeled human carotid artery bifurcation,” *Experiments in Fluids*, vol. 50, pp. 1131–1151, 2011.

[50] N. Johari, N. Wood, Z. Cheng, R. Torii, M. Oishi, M. Oshima, and X. Xu, “Disturbed flow in a stenosed carotid artery bifurcation: Comparison of rans-based transitional model and les with experimental measurements,” *International Journal of Applied Mechanics*, vol. 11, no. 4, p. 1950032, 2019.

[51] J. Bale-Glickman, K. Selby, D. Saloner, and ö. Savas, "Experimental flow studies in exact-replica phantoms of atherosclerotic carotid bifurcations under steady input conditions," *Journal of biomechanical engineering*, vol. 125, no. 1, pp. 38–48, 2003.

[52] . A. K. Prasad and C. Greated, "Stereoscopic particle image velocimetry," *Experiments in fluids*, vol. 29, no. 2, pp. 1181–1186, 2000.

[53] S. Kefayati, J. Milner, D. Holdsworth, and T. Poepping, "In vitro shear stress measurements using particle image velocimetry in a family of carotid artery models: effect of stenosis severity, plaque eccentricity, and ulceration," *PloS one*, vol. 9, no. 7, p. e98209, 2014.

[54] P. Geoghegan, P. Docherty, M. Sellier, and M. Jermy, "Understanding arterial pressure from PIV data," *18th international symposium on the application of laser and imaging techniques to fluid mechanics*, no. 7, 2016.

[55] V. Deplano, C. Guivier-Curien, and É. Bertrand, "3D analysis of vortical structures in an abdominal aortic aneurysm by stereoscopic PIV," *Experiments in Fluids*, vol. 57, pp. 1–11, 2016.

[56] R. Medero, C. Hoffman, and A. Roldaán-Alzate, "Comparison of 4D flow MRI and particle image velocimetry using an in vitro carotid bifurcation model," *Annals of Biomedical Engineering*, vol. 46, pp. 2112–2122, 2018.

[57] I. Khodarahmi, M. Shakeri, M. Kotys-Traughber, M. Sharp, and A. Amini, "Comparison of relative pressures calculated from PC-MRI and SPIV with catheter-based pressure measurements in a stenotic phantom model," *Progress in Biomedical Optics and Imaging - Proceedings of SPIE*, vol. 8317, pp. 133–139, 2012.

[58] L. D. Landau and E. M. Lifshitz, *Fluid Mechanics*. Institute of Physical Problems, U.S.S.R. Academy of Science, 1959.

[59] G. K. Batchelor, *An Introduction to Fluid Dynamics*. Cambridge University Press, 1967.

[60] F. A. Morrison, *An Introduction to Fluid Mechanics*. Cambridge University Press, 2013.

[61] J. B. Olesen, M. S. Traberg, M. J. Pihl, and J. A. Jensen, "Noninvasive estimation of 2-D pressure gradients in steady flow using ultrasound," *IEEE Transactions on Ultrasonics, Ferroelectrics, and Frequency Control*, vol. 61, no. 8, pp. 1409–1418, 2014.

[62] S. Skopalik, P. Hall Barrientos, J. Matthews, A. Radjenovic, P. Mark, G. Roditi, and M. C. Paul, "Image-based computational fluid dynamics for estimating pressure drop and fractional flow reserve across iliac artery stenosis: A comparison with in-vivo measurements," *International journal for numerical methods in biomedical engineering*, vol. 37, no. 12, p. e3437, 2021.

[63] A. Kazemi, D. Padgett, S. Callahan, M. Stoddard, and A. Amini, "Relative pressure estimation from 4D flow MRI using generalized bernoulli equation in a phantom model of arterial stenosis," *Magnetic Resonance Materials in Physics, Biology and Medicine*, vol. 35, no. 5, pp. 733–748, 2022.

[64] B. Casas, J. Lantz, P. Dyverfeldt, and T. Ebbers, "4D flow MRI-based pressure loss estimation in stenotic flows: Evaluation using numerical simulations: Pressure loss estimation in stenotic flows using 4D flow MRI," *Magnetic Resonance in Medicine*, vol. 75, no. 4, pp. 1808–1821, 2015.

[65] D. Nolte, J. Urbina, J. Sotelo, L. Sok, C. Montalba, I. Valverde, A. Osses, S. Uribe, and C. Bertoglio, "Validation of 4D flow based relative pressure maps in aortic flows," *Medical Image Analysis*, vol. 74, p. 102195, 2021.

[66] R. Sani, J. Shen, O. Pironneau, and P. Gresho, "Pressure boundary condition for the time-dependent incompressible Navier–Stokes equations," *International Journal for Numerical Methods in Fluids*, vol. 50, pp. 673 – 682, 2006.

[67] A. Moghaddam, G. Behrens, N. Fatouraee, R. Agarwal, E. Choi, and A. Amini, "Factors affecting the accuracy of pressure measurements in vascular stenoses from phase-contrast MRI," *Magnetic resonance in medicine : Society of Magnetic Resonance in Medicine*, vol. 52, pp. 300–309, 2004.

[68] C. Cortina, J. Bermejo, R. Yotti, M. Desco, D. Rodríguez-Pérez, J. Antoranz, J. L. Rojo-Álvarez, D. Garcia, M. García-Fernandez, and F. Fernández-Avilés, "Noninvasive assessment of the right ventricular filling pressure gradient," *Circulation*, vol. 116, pp. 1015–23, 2007.

[69] R. Yotti, J. Bermejo, C. Antoranz, J. L. Rojo-Álvarez, C. Allue, J. Silva, M. Desco, M. Moreno, and M. L. García-Fernández, "Noninvasive assessment of ejection intraventricular pressure gradients," *Journal of the American College of Cardiology*, vol. 43, no. 9, pp. 1654–1662, 2004.

[70] J. Bermejo, J. Antoranz, R. Yotti, M. Moreno, and M. García-Fernandez, "Spatio-temporal mapping of intracardiac pressure gradients. a solution to Euler's equation from digital postprocessing of color doppler M-mode echocardiograms," *Ultrasound in medicine and biology*, vol. 27, pp. 621–30, 2001.

[71] S. Fadnes, K. Sorensen, S. Nyrnes, M. Wigen, and L. Løvstakken, "Intraventricular Pressure Gradients - Vector Flow Imaging versus Color M-Mode," pp. 1–4, 2020.

[72] H. Ha, J.-P. Kvitting, P. Dyverfeldt, and T. Ebbers, "Validation of pressure drop assessment using 4D flow MRI-based turbulence production in various shapes of aortic stenoses," *Magnetic Resonance in Medicine*, vol. 81, no. 2, pp. 893–906, 2018.

[73] D. Garcia, P. Pibarot, and L.-G. Durand, "Analytical modeling of the instantaneous pressure gradient across the aortic valve," *Journal of biomechanics*, vol. 38, pp. 1303–11, 2005.

[74] A. Hodzic, D. Garcia, E. Saloux, P. Ribeiro, A. Ethier, J. Thomas, P. Milliez, H. Normand, and F. Tournoux, "Echocardiographic evidence of left ventricular untwisting-filling interplay," *Cardiovascular Ultrasound*, vol. 18, no. 1, pp. 1–12, 2020.

[75] R. Yotti, J. Bermejo, Y. Benito, J. C. Antoranz, M. M. Desco, D. Rodríguez-Pérez, and C. Cortina, "Noninvasive estimation of the rate of relaxation by the analysis of intraventricular pressure gradients," *Circulation. Cardiovascular imaging*, vol. 4, no. 2, pp. 94–104, 2011.

[76] T.-Q. Nguyen, M. Traberg, J. Olesen, R. Moshavegh, H. Møller-Sørensen, L. Lönn, J. Jensen, M. B. Nielsen, and K. Hansen, "Pressure Difference Estimation in Non-stenotic Carotid Bifurcation Phantoms Using Vector Flow Imaging," *Ultrasound in Medicine and Biology*, vol. 48, no. 2, pp. 346–357, 2022.

[77] L. E. Haslund, L. T. Jørgensen, M. Bo Stuart, M. S. Traberg, and J. A. Jensen, "Precise Estimation of Intravascular Pressure Gradients," *IEEE Transactions on Ultrasonics, Ferroelectrics, and Frequency Control*, vol. 70, no. 5, pp. 393–405, 2023.

[78] J. Kindere, A. Laskari, B. Ganapathisubramani, and R. Kat, "Pressure from 2D snapshot PIV," *Experiments in Fluids*, vol. 60, pp. 1–18, 2019.

[79] J. Charonko, C. King, B. Smith, and P. Vlachos, "Assessment of pressure field calculations from particle image velocimetry measurements," *Measurement Science and Technology*, vol. 21, p. 105401, 2010.

[80] B. W. Van Oudheusden, "PIV-based pressure measurement," *Measurement Science and Technology*, vol. 24, no. 3, p. 032001, 2013.

[81] D. Garcia, J. Dumesnil, L.-G. Durand, L. Kadem, and P. Pibarot, "Discrepancies between catheter and Doppler estimates of valve effective orifice area can be predicted from the pressure recovery phenomenon. Practical implications with regards to quantification of aortic stenosis severity," *Journal of the American College of Cardiology*, vol. 41, pp. 435–442, 2003.

[82] D. Garcia, P. Pibarot, J. Dumesnil, F. Sakr, and L.-G. Durand, "Assessment of Aortic Valve Stenosis Severity: A New Index Based on the Energy Loss Concept," *Circulation*, vol. 101, pp. 765–71, 2000.

[83] P. Pibarot, D. Garcia, and J. Dumesnil, "Energy Loss Index in Aortic Stenosis From Fluid Mechanics Concept to Clinical Application," *Circulation*, vol. 127, pp. 1101–4, 2013.

[84] F. Donati, C. Figueroa, N. Smith, P. Lamata, and D. Nordsletten, "Non-Invasive Pressure Difference Estimation from PC-MRI using the Work-Energy Equation," *Medical Image Analysis*, vol. 26, no. 1, pp. 159–172, 2015.

[85] D. Marlevi, B. Ruijsink, M. Balmus, D. Dillon-Murphy, D. Fovargue, K. Pushparajah, C. Bertoglio, M. Colarieti-Tosti, M. Larsson, P. Lamata, C. Figueroa, R. Razavi, and D. Nordsletten, "Estimation of Cardiovascular Relative Pressure Using Virtual Work-Energy," *Scientific Reports*, vol. 9, no. 1, pp. 1–16, 2019.

[86] C. Bertoglio, R. N 'unez, F. Galarce, D. Nordsletten, and A. Osses, "Relative pressure estimation from velocity measurements in blood flows: State-of-the-art and new approaches," *International journal for numerical methods in biomedical engineering*, vol. 34, no. 2, p. e2925, 2017.

[87] W. Rodi, *Turbulence models and their application in hydraulics*. CRC Press, 1993.

[88] D. Garcia, "an open-source simulator for medical ultrasound imaging. Part I: theory & examples," *Computer Methods and Programs in Biomedicine*, p. 106726, 2022.

[89] A. Cigier, F. Varray, and D. Garcia, "SIMUS: An open-source simulator for medical ultrasound imaging. part II: Comparison with four simulators," *Computer Methods and Programs in Biomedicine*, vol. 220, p. 106774, 2022.

[90] D. Garcia, "Make the most of MUST, an open-source Matlab Ultrasound Toolbox.," *In 2021 IEEE International Ultrasonics Symposium (IUS)*, vol. 220, pp. 1–4, 2021.

[91] M. Y. Yousif, D. W. Holdsworth, and T. L. Poepping, "A blood-mimicking fluid for particle image velocimetry with silicone vascular models," *Experiments in fluids*, vol. 50, pp. 769–774, 2011.

[92] P. H. Geoghegan, N. A. Buchmann, C. J. Spence, S. Moore, and M. Jermy, "Fabrication of rigid and flexible refractive-index-matched flow phantoms for flow visualisation and optical flow measurements," *Experiments in fluids*, vol. 52, pp. 1331–1347, 2012.

[93] N. A. Buchmann, M. C. Jermy, and C. V. Nguyen, "Experimental investigation of carotid artery haemodynamics in an anatomically realistic model," *International Journal of Experimental and Computational Biomechanics*, vol. 1, no. 2, pp. 172–192, 2009.

[94] R. F. Smith, B. K. Rutt, and D. W. Holdsworth, "Anthropomorphic carotid bifurcation phantom for MRI applications," *Journal of Magnetic Resonance Imaging*, vol. 10, no. 4, pp. 533–544, 1999.

[95] S. Kefayati, D. W. Holdsworth, and T. L. Poepping, "Turbulence intensity measurements using particle image velocimetry in diseased carotid artery models: Effect of stenosis severity, plaque eccentricity, and ulceration," *Journal of biomechanics*, vol. 47, no. 1, pp. 253–263, 2014.

[96] I. N. Staikov, M. Arnold, H. Mattle, L. Remonda, M. Sturzenegger, R. W. Baumgartner, and G. Schroth, "Comparison of the ECST, CC, and NASCET grading methods and ultrasound for assessing carotid stenosis," *Journal of neurology*, vol. 247, pp. 681–686, 2000.

[97] H. V. Anderson, G. S. Roubin, P. P. Leimgruber, W. Cox, J. Douglas Jr, S. King 3rd, and A. Gruentzig, "Measurement of transstenotic pressure gradient during percutaneous transluminal coronary angioplasty.," *Circulation*, vol. 73, no. 6, pp. 1223–1230, 1986.

[98] O. Veselỳ, L. Nováková, and J. Adamec, "Experimental study of effect of stenosis geometry on flow parameters," in *EPJ Web of Conferences*, vol. 92, p. 02105, EDP Sciences, 2015.

[99] N. Freidoonimehr, R. Chin, A. Zander, and M. Arjomandi, "An experimental model for pressure drop evaluation in a stenosed coronary artery," *Physics of Fluids*, vol. 32, no. 2, p. 021901, 2020.

[100] F. C. Sales, R. M. Ariati, V. T. Noronha, and J. E. Ribeiro, "Mechanical characterization of PDMS with different mixing ratios," *Procedia Structural Integrity*, vol. 37, pp. 383–388, 2022.

[101] C. Avigo, N. Di Lascio, P. Armanetti, C. Kusmic, L. Cavigli, F. Ratto, S. Meucci, C. Masciullo, M. Cecchini, R. Pini, *et al.*, "Organosilicon phantom for photoacoustic imaging," *Journal of biomedical optics*, vol. 20, no. 4, pp. 046008–046008, 2015.

[102] L. Hacker, J. Joseph, A. M. Ivory, M. O. Saed, B. Zeqiri, S. Rajagopal, and S. E. Bohndiek, "A copolymer-in-oil tissue-mimicking material with tuneable acoustic and optical characteristics for photoacoustic imaging phantoms," *IEEE Transactions on Medical Imaging*, vol. 40, no. 12, pp. 3593–3603, 2021.

[103] N. Hungr, J.-A. Long, V. Beix, and J. Troccaz, "A realistic deformable prostate phantom for multimodal imaging and needle-insertion procedures," *Medical physics*, vol. 39, no. 4, pp. 2031–2041, 2012.

[104] S. E. Bohndiek, S. Bodapati, D. Van De Sompel, S.-R. Kothapalli, and S. S. Gambhir, "Development and application of stable phantoms for the evaluation of photoacoustic imaging instruments," *PloS one*, vol. 8, no. 9, p. e75533, 2013.

[105] U. C. Gautam, Y. S. Pydi, S. Selladurai, C. J. Das, A. K. Thittai, S. Roy, and N. V. Datla, "A poly-vinyl alcohol (PVA)-based phantom and training tool for use in simulated transrectal ultrasound (TRUS) guided prostate needle biopsy procedures," *Medical Engineering & Physics*, vol. 96, pp. 46–52, 2021.

[106] K. Surry, H. Austin, A. Fenster, and T. Peters, "Poly (vinyl alcohol) cryogel phantoms for use in ultrasound and mr imaging," *Physics in Medicine & Biology*, vol. 49, no. 24, p. 5529, 2004.

[107] S. H. Hyon, W. I. Cha, and Y. Ikada, "Preparation of transparent poly (vinyl alcohol) hydrogel," *Polymer bulletin*, vol. 22, pp. 119–122, 1989.

[108] K. Zell, J. I. Sperl, M. W. Vogel, R. Niessner, and C. Haisch, "Acoustical properties of selected tissue phantom materials for ultrasound imaging," *Physics in Medicine & Biology*, vol. 52, no. 20, p. N475, 2007.

[109] A. Kharine, S. Manohar, R. Seeton, R. G. Kolkman, R. A. Bolt, W. Steenbergen, and F. F. de Mul, "Poly (vinyl alcohol) gels for use as tissue phantoms in photoacoustic mammography," *Physics in Medicine & Biology*, vol. 48, no. 3, p. 357, 2003.

[110] M. S. S. Hashuro, S. Tupin, N. K. Putra, K. Daibo, K. Inoue, T. Ishii, H. Kosukegawa, K. Funamoto, T. Hayase, and M. Ohta, "Development of ultrasound phantom made of transparent material: Feasibility of optical particle image velocimetry," *Ultrasound in Medicine & Biology*, vol. 49, no. 6, pp. 1385–1394, 2023.

[111] K. Funamoto, O. Yamashita, and T. Hayase, "Poly (vinyl alcohol) gel ultrasound phantom with durability and visibility of internal flow," *Journal of Medical Ultrasonics*, vol. 42, pp. 17–23, 2015.

[112] N. Ackroyd, R. Gill, K. Griffiths, G. Kossoff, and M. Appleberg, "Quantitative common carotid artery blood flow: prediction of internal carotid artery stenosis," *Journal of vascular surgery*, vol. 3, no. 6, pp. 846–853, 1986.

[113] T. L. Poepping, R. N. Rankin, and D. W. Holdsworth, "Flow patterns in carotid bifurcation models using pulsed Doppler ultrasound: effect of concentric vs. eccentric stenosis on turbulence and recirculation," *Ultrasound in medicine & biology*, vol. 36, no. 7, pp. 1125–1134, 2010.

[114] P. Likittanasombut, P. Reynolds, D. Meads, and C. Tegeler, "Volume Flow Rate of Common Carotid Artery Measured by Doppler Method and Color Velocity Imaging Quantification (CVI-Q)," *Journal of Neuroimaging*, vol. 16, no. 1, pp. 34–38, 2006.

[115] A. de Vecchi, R. E. Clough, N. R. Gaddum, M. C. Rutten, P. Lamata, T. Schaeffter, D. A. Nordsletten, and N. P. Smith, "Catheter-induced errors in pressure measurements in vessels: an in-vitro and numerical study," *IEEE Transactions on Biomedical Engineering*, vol. 61, no. 6, pp. 1844–1850, 2014.

[116] J. J. Cavendish, L. I. Carter, and S. Tsimikas, "Recent advances in hemodynamics: noncoronary applications of a pressure sensor angioplasty guidewire," *Catheterization and Cardiovascular Interventions*, vol. 71, no. 6, pp. 748–758, 2008.

[117] W. Thielicke and E. Stamhuis, "PIVlab–towards user-friendly, affordable and accurate digital particle image velocimetry in MATLAB," *Journal of open research software*, vol. 2, no. 1, 2014.

[118] A. J. Chee, C. K. Ho, B. Y. Yiu, and C. Alfred, "Walled carotid bifurcation phantoms for imaging investigations of vessel wall motion and blood flow dynamics," *IEEE transactions on ultrasonics, ferroelectrics, and frequency control*, vol. 63, no. 11, pp. 1852–1864, 2016.

[119] T. L. Poepping, N. Nikolov, N. Rankin, M. Lee, and D. W. Holdsworth, "An in vitro system for Doppler ultrasound flow studies in the stenosed carotid artery bifurcation," *Ultrasound in medicine & biology*, vol. 28, no. 4, pp. 495–506, 2002.

List of Figures

List of Tables

FOLIO ADMINISTRATIF

THESE DE L'INSA LYON, MEMBRE DE L'UNIVERSITE DE LYON

NOM : CHOUPANI DATE de SOUTENANCE : 10/11/2023
(avec précision du nom de jeune fille, le cas échéant)

Prénoms : Samaneh

TITRE : Intravascular manometry by clinical color Doppler

NATURE : Doctorat Numéro d'ordre : 2023ISAL0085

Ecole doctorale : Mécanique, Énergétique, Génie civil, Acoustique

Spécialité : Biomécanique

RESUME : La sténose artérielle désigne le rétrécissement des artères du système circulatoire, obstruant le flux sanguin normal. Un tel rétrécissement conduit généralement à une diminution de l'approvisionnement en oxygène, et à des complications potentielles pouvant aller jusqu'à l'ischémie dans les cas les plus graves. Un diagnostic précoce et un traitement approprié sont essentiels pour prendre en charge la sténose artérielle, prévenir d'autres complications potentielles et maintenir un flux sanguin optimal. Les approches traditionnelles pour évaluer la sévérité d'une sténose consistent à imager la région en question par échographie, afin d'évaluer sa gravité par des critères géométriques spécifiques issus de l'imagerie. Cependant, ces critères fournissent une information partielle et ignorent les aspects hémodynamiques du flux qui pourraient offrir des informations complémentaires sur la sténose. Une solution consiste à mesurer la chute de pression sanguine intravasculaire entre l'entrée et la sortie d'une sténose. Cette chute de pression est causée par la turbulence post-sténotique et la dissipation d'énergie due aux forces de friction au sein du fluide. Traditionnellement, cette mesure est effectuée par cathéter intravasculaire, une procédure invasive. Cependant, des méthodes non invasives utilisant l'imagerie du flux sanguin sont souvent préférées pour réduire les coûts et les effets secondaires potentiels. L'imagerie par échographie Doppler couleur est une modalité d'imagerie non invasive facilitant l'étude du flux intravasculaire. Sa portabilité combinée à sa capacité à fournir des informations en temps réel sur le flux sanguin, en fait un choix idéal pour l'étude du flux intravasculaire. Cependant, il est essentiel de rappeler que le mode Doppler couleur fournit uniquement une projection de la vitesse sanguine selon l'axe du faisceau ultrasonore. En obtenant le champ vectoriel de la vitesse et en utilisant les équations de la dynamique des fluides, la chute de pression trans-sténotique pourrait être mesurée. L'objectif de cette thèse est de développer et d'examiner la faisabilité d'une technique non invasive utilisant l'imagerie Doppler couleur clinique pour estimer la perte de pression trans-sténotique dans les cas de sténose de l'artère carotide de légère à modérée, en vue d'un diagnostic plus précoce de la gravité de la sténose. La contribution à cette étude est double. Premièrement, une technique de cartographie du flux vectoriel vasculaire (*v*VFM) a été développée afin d'estimer le champ vectoriel des vitesses à partir du champ scalaire Doppler couleur. Ceci est réalisé en minimisant un problème au sens des moindres carrés, tout en utilisant la méthode des multiplicateurs de Lagrange. Deux contraintes liées aux principes de base de la dynamique des fluides sont utilisées : la conservation de la masse et les conditions aux limites de non-glissement. La deuxième contribution est une méthode d'estimation des pertes de pression basées sur les équations de la dynamique des fluides, où nous suggérons une combinaison de l'utilisation de l'équation de Bernoulli et de l'équation de Navier-Stokes. Cette méthode a été validée *in silico* via la dynamique des fluides computationnelle et des simulations d'ultrasons, et *in vitro* à travers la vélocimétrie par images de particules et des expériences d'échographie Doppler couleur sur des modèles de sténose carotide et des fantômes à débits constants. Ce travail de thèse démontre la fiabilité et la faisabilité d'une méthode complète non invasive pour l'estimation de la perte de pression trans-sténotique en utilisant le Doppler couleur clinique.

MOTS-CLÉS : Sténose artérielle, perte de pression, Doppler couleur, imagerie de flux vectoriel, optimisation contrainte.

Laboratoire (s) de recherche : CREATIS
Directeur de thèse : Damien Garcia

Président de jury :

Composition du jury : Valérie Deplano (Rapporteure), Lasse Løvstakken (Rapporteur), Olivier Bernard (Examinateur), Laurence Rouet (Examinatrice), Jean-Christophe Béra (Co-encadrant), Bruno Gilles (Co-encadrant), François Varray (Co-directeur), Damien Garcia (Directeur de thèse)